technische universität
dortmund

Arbeit zur Erlangung des akademischen Grades
Master of Science

Stationary states after interaction quenches in the Fermi-Hubbard model

Philip Bleicker
geboren in Dortmund

2017

Lehrstuhl für Theoretische Physik I
Fakultät Physik
Technische Universität Dortmund

Erstgutachter:	Prof. Dr. Götz S. Uhrig, Technische Universität Dortmund
Zweitgutachter:	Prof. Dr. Ralf Schützhold, Universität Duisburg-Essen
Abgabedatum:	5. Oktober 2017

Abstract

The one-dimensional Fermi-Hubbard model exposed to a sudden global quantum quench is studied where global quenching describes the phenomenon of abruptly altering properties of a physical model. Respective systems being exposed to a quench are to be characterized by processes spread over all energy scales and can only be described using non-equilibrium physics. However, since no general comprehensive techniques for doing so exist up to now assessing the dynamics becomes highly non-trivial.

In this context, the iterated equations of motion approach serves as a means to gain insight into both the dynamics on all time scales and – using long-term averages – into possibly occurring stationary states. Unlike as in former studies a suitable scalar product is chosen which allows for preservation of operator unitarity. Thus, no non-unitary effects like exponentially increasing parts of solutions spoil the results and the dynamics following a quench can be assessed on noticeably longer time scales.

Kurzfassung

Im Rahmen der vorliegenden Arbeit wird der Einfluss globaler Wechselwirkungsquenches auf das eindimensionale Fermi-Hubbard Modell untersucht, wobei es sich bei einem globalen Quench anschaulich um das plötzliche Abändern zentraler Systemcharakteristika handelt. Ein einem derartigen Phänomen ausgesetztes System befindet sich in einem hochgradigen Nichtgleichgewichtszustand mit Prozessen auf nahezu allen Energieskalen und verschließt sich in der Folge einer einfachen Beschreibung seiner Dynamik.

Ein Ansatz, um Einblicke sowohl in Systemdynamik auf allen Zeitskalen als auch – vermöge langfristiger Mittelwerte – in ggf. vorliegende Entwicklung hin zu stationären Zuständen zu erhalten, wird mit den iterierten Bewegungsgleichungen vorgestellt. Dabei wird im Gegensatz zu in vorigen Studien gewählten Ansätzen durch die Wahl eines geeigneten Operatorskalarprodukts Unitarität auf Operatorebene gewährleistet sowie das Auftreten exponentiell ansteigender Lösungsanteile verhindert. Die resultierende Dynamik nach dem Quench ist entsprechend für wesentlich längere Zeiträume zugänglich.

Contents

List of Figures

1 Introduction

The research area of non-equilibrium physics has gained high attention within recent years due to considerable progress regarding the experimental feasibility to both prepare systems in non-equilibrium states and to maintain their isolation from the environment for fairly long times. Undoubtedly, two of the most notable experimental achievements are the ability to confine ultra-cold atomic gases in optical lattices [1–3] – rendering it possible to practically analyze former merely theoretical Hamiltonians [4, 5] – and femtosecond spectroscopy which permits to gain insight into ultrafast dynamics as well as the development of correlations in solid state physics [6–8].

With the increasing interest in non-equilibrium physics a new tool kit is needed. Most theoretical approaches are suitable for describing equilibria as they are based on the assumption that the considered system is in a state near to the ground state or a thermally excited state and excitations may be modelled as (dressed) quasi-particles [9]. Evidently, such methods break down in a non-equilibrium system where dynamics is governed by processes spreading over all energy scales and where the system itself is in a highly excited state.

One possible approach used widely to drive a system out of equilibrium is that of modifying a system by a sudden parameter quench. Quenching is a generic technique both on global [10–15] and local level [16, 17] and consists of suddenly modifying a system, e.g. by preparing the system in the ground state of one Hamiltonian and observing the evolution governed by a different one. This concept was already applied to the one-dimensional Bose-Hubbard model to study quenches across quantum phase transitions both theoretically [18] and experimentally [19] or to examine the propagation of thermal correlations by coherently splitting a one-dimensional Bose gas into two distinct parts [20].

Moreover, quenches were studied in one-dimensional fermionic systems using exact diagonalization to probe thermalization [21], non-equilibrium dynamical mean field theory (DMFT) [22] – which becomes an exact treatment for infinite dimensions –, variational Gutzwiller approaches [23, 24] or repeated applications of the Heisenberg equations of motion [25, 26]. Using perturbative expansions in powers of the inverse coordination number and reduced density matrices renders studying higher dimensional lattices [27] or systems with many tunneling partners [28] possible.

Additionally, various further theoretical approaches exist to account for recent advances in experiments such as time-dependent density matrix renormalization group (tDMRG) techniques [29] being suitable for one dimension only, simulations

performed with quantum Monte Carlo methods [30, 31] or forward-backward continuous unitary transformations [32, 33]. It is worth noting that quenching is not limited to a mere modification of mutual particle interaction but can also be realized by abrupt changes of external fields [10–12] or even of the system geometry [34, 35].

Different invasive and non-invasive experimental methods have been proposed lately which facilitate to study quantum states and thus intrinsic properties of quenched systems. With the aid of Bragg spectroscopy and time-of-flight experiments the excitation spectrum of a one-dimensional Bose gas trapped in an optical lattice could be shown to yield a broad continuum in the superfluid, but a nearly discrete spectrum in the Mott insulating phase [36]. Another invasive imaging process is the so called *in situ* technique which can, e.g., be performed by means of fluorescence [37] and allows for dedicated site-resolved measurement results.

Though, non-invasive approaches are of high interest since they are able to preserve information such as phase coherence in a non-destructive manner. Corresponding ideas range from matter-wave scattering [38, 39] or using optical cavities [40] which even allows for measuring the dynamic structure factor of a quantum gas [41] to using Dicke superradiance as a sensitive probe [42].

In spite of all progress no comprehensive explanations exist up to now why and in how far relaxation and equilibration take place. Time-reversal invariant unitary non-equilibrium dynamics on microscopic level may contradict equilibrated systems at first glance. Phenomena like thermalization are partially explained by the eigenstate thermalization hypothesis [43, 44] which, though, suffers from inadequacy in integrable models [45]. Consequently, gaining further insight into proper ways to assess non-equilibrium time evolution is still highly demanded for a thorough understanding of systems far away from equilibrium.

The outline of this work is as follows. In chapter 2 the Fermi-Hubbard model is introduced and the common techniques involved when quenching a system are elaborated. Moreover, decisive observables to study non-equilibrium phenomena are discussed. The theoretical tool kit of iterated equations of motion to study non-equilibrium physics used throughout all chapters to come is described in chapter 3 accompanied by a dedicated analysis of quasi-particle creation driving the dynamics of the Fermi-Hubbard model. In this context, different approaches to determine operator bases are compared to one another. In chapter 4 a possibility to gain insight into the behaviour of the system for infinite times by means of long-term averages is derived. Chapter 5 deals with properties of different operator bases whereas in chapter 6 the most promising operator basis is put to use to study physical properties of the one-dimensional Fermi-Hubbard model following an interaction quench.

2 Fermi-Hubbard model and quenching

The Fermi-Hubbard model consists of tight-binding electrons with Coulomb interaction [46–48] and is – due to its simplicity and depending on the model parameters – often used to describe electronic properties of condensed-matter systems with narrow energy bands, metal-insulator-transitions or even high-temperature superconductors.

2.1 Model description

Since the Fermi-Hubbard model is made up of an effective one-particle problem H_0 depicting electron hopping through a given lattice and Coulomb repulsion resulting in an interacting part of the Hamiltonian H_{int} the generic Hamiltonian

$$H = H_0 + H_{\text{int}} \text{ with } H_0 = \sum_i^{N_e} \frac{\mathbf{p}_i^2}{2m} + V(\mathbf{r}_i),\ H_{\text{int}} = \frac{1}{2}\sum_{i\neq j}^{N_e} U(\mathbf{r}_i - \mathbf{r}_j) \tag{2.1}$$

arises in first quantization. Considering the derivations of appendix A regarding second quantization and the occupation number representation a basis of one-particle states has to be chosen. Two possible basis choices are discussed below.

2.1.1 Real space representation

For a representation in real space it is advisable to represent the tightly bound electrons by highly localized Wannier functions [49, 50] which form a complete set of orthogonal functions. Let the corresponding creation and annihilation operators be $f_{\mathbf{l}\sigma}^\dagger$ and $f_{\mathbf{l}\sigma}$ for creating or annihilating a particle at lattice vector $\mathbf{l}$ with spin direction $\sigma \in \{\uparrow, \downarrow\}$. Resorting to simplifying approximations such as using only nearest-neighbour hopping and a completely local Coulomb repulsion due to screening leads to the Hamiltonian for the Fermi-Hubbard model with one band in real space

$$H_0 = -J \sum_{\substack{\langle \mathbf{l}', \mathbf{l}\rangle \\ \sigma}} f_{\mathbf{l}'\sigma}^\dagger f_{\mathbf{l}\sigma}, \tag{2.2a}$$

$$H_{\text{int}} = U \sum_{\mathbf{l}\sigma} \widehat{n}_{\mathbf{l}\uparrow}\widehat{n}_{\mathbf{l}\downarrow} \tag{2.2b}$$

for a hopping element J and an energetic penalty U for double occupation of a given site.

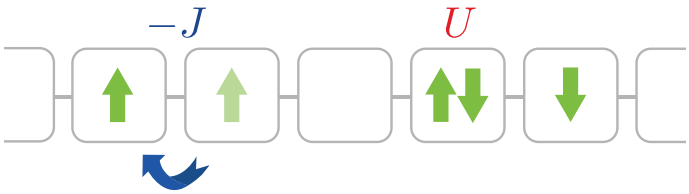

Figure 2.1: Depiction of the one-dimensional Fermi-Hubbard model in real space. Electron hopping sets free an energy of amount J, double occupancy of a site costs an energy of amount U.

The one-dimensional Fermi-Hubbard model depicted in figure 2.1 can be analytically solved via Bethe ansatz [51, 52], but in spite of its seemingly easy form no comprehensive analytical solution for the Fermi-Hubbard model in higher dimensions is known so far.

2.1.2 Momentum space representation

A transformation of (2.2) with the aid of the Fourier transformed creation and annihilation operators for a crystal of N unit cells

$$f^\dagger_{\mathbf{k}\sigma} = \frac{1}{\sqrt{N}} \sum_{\mathbf{l}} f^\dagger_{\mathbf{l}\sigma} e^{i\mathbf{k}\mathbf{l}} \tag{2.3a}$$

$$f_{\mathbf{k}\sigma} = \frac{1}{\sqrt{N}} \sum_{\mathbf{l}} f_{\mathbf{l}\sigma} e^{-i\mathbf{k}\mathbf{l}} \tag{2.3b}$$

leads to the Fermi-Hubbard model in momentum space. The used basis is the H_0 eigenbasis and the Hamiltonian becomes

$$H_0 = \sum_{\mathbf{k}\sigma} \varepsilon_{\mathbf{k}} f^\dagger_{\mathbf{k}\sigma} f_{\mathbf{k}\sigma}, \tag{2.4a}$$

$$H_{\text{int}} = \frac{U}{N} \sum_{\mathbf{k}\mathbf{k}'\mathbf{q}} f^\dagger_{\mathbf{k}+\mathbf{q}\uparrow} f^\dagger_{\mathbf{k}'-\mathbf{q}\downarrow} f_{\mathbf{k}'\downarrow} f_{\mathbf{k}\uparrow}. \tag{2.4b}$$

In order to obtain equation (2.4) it was made use of the orthogonality relation

$$\sum_{\mathbf{l}} f^\dagger_{\mathbf{l}\sigma} e^{i(\mathbf{k}-\mathbf{k}')\mathbf{l}} = N\delta_{\mathbf{k}\mathbf{k}'}. \tag{2.5}$$

Notice that the eigenbasis of H_0 can be motivated from a physical perspective. Since H_0 is an effective one-particle problem of an electron in a lattice-periodic potential with discrete translational symmetry the Bloch theorem [53] states that an energy eigenbasis exists which consists of Bloch functions, i.e. modulated plain waves.

The dispersion relation in the case of hypercubic d-dimensional lattices reads

$$\varepsilon_{\mathbf{k}} := -2J \sum_{i=1}^{d} \cos\left(\mathbf{k}\mathbf{a}_i\right) \tag{2.6}$$

with $\mathbf{a}_i$ denoting primitive translation vectors spanning the underlying lattice. The one-dimensional case is illustrated in figure 2.2 for half-filling.

In consistency with expectations the interaction-free bilinear part H_0 becomes diagonal in its eigenbasis. Hence, for vanishing U the Fermi-Hubbard model is analytically solved by Bloch electrons with its ground state being the Fermi sea $|\mathrm{FS}\rangle$. A natural energy scale is constituted by the bandwidth $W = 2zJ$ where z denotes the coordination number of the used lattice. The bandwidth of a one-dimensional lattice, i.e. $z = 2$, is shown on the ordinate axis in figure 2.2 as the energetic range the particle states are located in. Moreover, the bandwidth defines an appropriate time scale for the system by $1/W$.

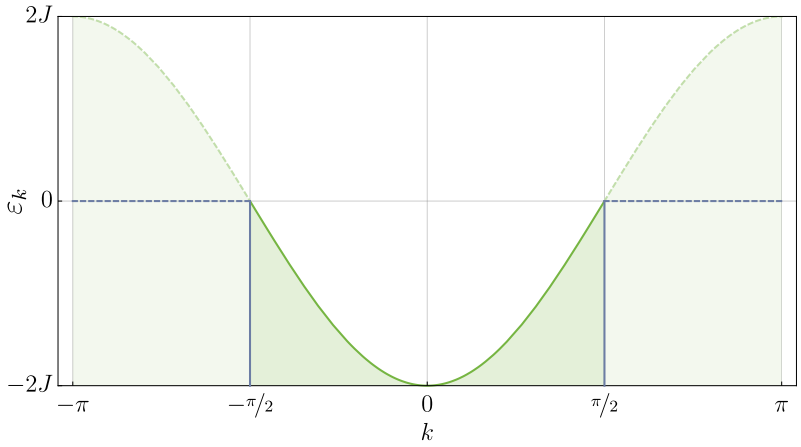

Figure 2.2: Dispersion relation ε_k for the one-dimensional Fermi-Hubbard model according to (2.6) over the first Brillouin zone, i.e. $k \in \,]-\pi, \pi]$, with a lattice constant set to unity. Half-filling is shown, i.e. starting from the energetically lowest case of $k = 0$ the possible k-states are gradually filled in order of increasing energy such that finally states within $\left[-\frac{\pi}{2}, \frac{\pi}{2}\right]$ are occupied. The Fermi wave vector with absolute value $k_\mathrm{F} = \frac{\pi}{2}$ is denoted by solid blue lines, the Fermi energy $E_\mathrm{F} = 0$ as the highest occupied energy by dashed blue lines.

In the case of nonvanishing interaction the electrons are scattered by (2.4b). The process maintains the total momentum as the involved particles leave their former one-particle states $|\mathbf{k}\uparrow\rangle$ and $|\mathbf{k}'\downarrow\rangle$ in order to afterwards occupy $|\mathbf{k}+\mathbf{q}\uparrow\rangle$ and $|\mathbf{k}'-\mathbf{q}\downarrow\rangle$.

2.2 Quenching

To study non-equilibrium physics a sudden quantum quench is used where the system of temperature $T = 0$ is initially prepared in an eigenstate of a given Hamiltonian H_1, e.g. (2.2a) or (2.4a) with the eigenstate in question being the Fermi sea $|\mathrm{FS}\rangle$, having its time evolution governed by a different Hamiltonian $H_1 + H_2$, e.g. the full Fermi-Hubbard Hamiltonian (2.2) or (2.4). This explicit time dependence can be described by the quenched Hamiltonian

$$H_{\mathrm{Q}}(t) = H_1 + \theta(t)H_2. \tag{2.7}$$

The state drastically deviates from $|\mathrm{FS}\rangle$ for $t > 0$. Since the quench described in equation (2.7) changes overall system parameters it is called a global quench. The technique of global quenching is widely used [10–15] and the method considered here and in the chapters to come.

Besides globally altering system parameters it is also possible to drive the system out of equilibrium locally [16, 17] or even to study the influences of abruptly modifying the system geometry altogether by geometric quenches, e.g. by changing the size of the system in one-dimensional models [34] or by glueing together spin chains of different length and magnetization [35].

A crucial aspect is if the many-body system being taken out of equilibrium relaxes towards equilibrium again in the limit of long times. Thermalization and consequently the question if the system or a subpart of it – for example with respect to certain observables $A(t)$ – behaves as if it was describable by equilibrium thermodynamics and thus statistical ensemble theory is of high interest [54]. The term thermalization denotes a development of the system towards a state that is practically indistinguishable from thermal equilibrium, i.e. all microstates of the system can occur with a probability proportional to $e^{-\beta H}$ with the inverse temperature $\beta = 1/k_{\mathrm{B}}T$. On time scales that are noticeably shorter than the thermal equilibration time the phenomenon of prethermalization can emerge. This means a subset of quantities already possesses their final equilibrated values even though the momentum distribution heavily differs from the one in thermal equilibrium [55].

For integrable Hamiltonians with their huge numbers of conserved quantities a full thermalization of a system being in a non-equilibrium state to the canonical ensemble is impossible but maximum entropy states can still be reached [54]. The reason for this lies in the constraints formed by the quantities making the system integrable. These quantities prohibit an ergodical sampling of phase space points with equal energy and thus violate a general assumption of thermodynamics. The generalized Gibbs ensemble introduced in Ref. [56] offers a possibility to predict equilibrated values. Explanations for its success in doing so were tried to be given [57]. Surprisingly, even systems being only close to integrability do not obligatorily reach thermal equilibrium as was experimentally proven by Kinoshita et al. [58].

The one-dimensional Fermi-Hubbard model fulfills the Yang-Baxter conditions [59, 60], is integrable and can be solved, e.g. by means of the Lieb-Wu equations [51].

2.3 Observables and influence of quenching

Hereafter, important observables used to gain insight into non-equilibrium dynamics and to answer the above mentioned questions are characterized. The exact time dependence of observables is later computed by methods introduced in chapter 3.

2.3.1 One-particle correlation function and local particle number average

The one-particle correlation function for equal times is defined by the relation

$$G_\sigma(\mathbf{l_1}, \mathbf{l_2}, t) = G_\sigma(\mathbf{l_2} - \mathbf{l_1}, t) := \langle \mathrm{FS}| f_{\mathbf{l_2}\sigma}(t) f^\dagger_{\mathbf{l_1}\sigma}(t)|\mathrm{FS}\rangle \tag{2.8}$$

and depends only on the relative difference $\mathbf{l_2} - \mathbf{l_1}$ due to discrete translational invariance. Through (2.8) and (A.6) an observable suited to crosscheck numerical results can be derived as the expectation value of the local particle number operator

$$n_{\mathbf{l}\sigma}(t) := \langle \widehat{n}_{\mathbf{l}\sigma}(t)\rangle = \langle \mathrm{FS}| f^\dagger_{\mathbf{l}\sigma}(t) f_{\mathbf{l}\sigma}(t)|\mathrm{FS}\rangle = 1 - G_\sigma(\mathbf{0}, t) \tag{2.9}$$

that measures the average particle number of particles with spin σ at a given lattice site for time t. According to the right-hand side of equation (2.9) it does not matter what lattice site $\mathbf{l}$ is chosen.

The reason why the observable (2.9) is meaningful lies in the $U(1)$ symmetry present in (2.2) causing the invariance of the Fermi-Hubbard Hamiltonian under the continuous transformation

$$f^\dagger_{\mathbf{l}\sigma} \to f^\dagger_{\mathbf{l}\sigma} \exp(i\alpha) \tag{2.10a}$$

$$f_{\mathbf{l}\sigma} \to f_{\mathbf{l}\sigma} \exp(-i\alpha)\,. \tag{2.10b}$$

As the arbitrary phase α and the total particle number operator

$$\widehat{N} = \sum_{\mathbf{l}\sigma} \widehat{n}_{\mathbf{l}\sigma} \tag{2.11}$$

are conjugate variables [61] the continuous $U(1)$ symmetry implies an indeterminate phase and according to Noether's theorem a conserved total particle number/electric charge. Another possibility to verify the particle conserving properties of (2.2) is to check that the relation $\left[H, \widehat{N}\right] = 0$ holds. Considering the fact that particles are neither added nor removed it can be concluded that

$$n_{\mathbf{l}\sigma}(t) =: n \tag{2.12}$$

is valid for all times with $n = \text{const}$ denoting the filling factor. Any deviations of $n_{\mathbf{l}\sigma}(t)$ from n can thus be ascribed to approximations or numerical inadequacy and serve as a means to estimate the time range numerical results can be relied on.

2.3.2 Momentum distribution and jump at the Fermi surface

The momentum distribution indicates the average number of particles with wave vector $\mathbf{k}$ and spin direction σ at a time t as shown in figure 2.3 and is defined by

$$n_{\mathbf{k}\sigma}(t) := \langle \widehat{n}_{\mathbf{k}\sigma}(t) \rangle = \langle \mathrm{FS} | f^\dagger_{\mathbf{k}\sigma}(t) f_{\mathbf{k}\sigma}(t) | \mathrm{FS} \rangle \,. \tag{2.13}$$

Employing equation (2.3) and (2.8) it can be shown that the momentum distribution is closely related to the one-particle correlation function

$$n_{\mathbf{k}\sigma}(t) = \frac{1}{N} \sum_{\mathbf{l_1 l_2}} e^{-i\mathbf{k}(\mathbf{l_2}-\mathbf{l_1})} \langle \mathrm{FS} | f^\dagger_{\mathbf{l_1}\sigma}(t) f_{\mathbf{l_2}\sigma}(t) | \mathrm{FS} \rangle \tag{2.14a}$$

$$= \sum_{\mathbf{l}} e^{-i\mathbf{k}\mathbf{l}} \left(\delta_{\mathbf{l},\mathbf{0}} - G_\sigma(\mathbf{l}, t) \right) . \tag{2.14b}$$

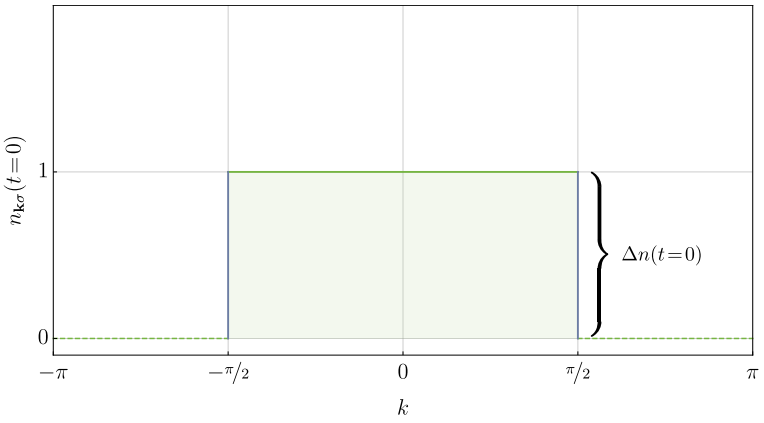

Figure 2.3: The momentum distribution $n_{\mathbf{k}\sigma}(t)$ is closely related to the jump at the Fermi surface $\Delta n(t)$ via equation (2.15). Half-filling is depicted for $t = 0$ with the initial state being the Fermi sea, k_F is denoted by solid blue lines.

The Fermi sea shows a sharp jump at the Fermi surface due to the fact that all states with the property $|\mathbf{k}| \leq k_\mathrm{F}$ ($|\mathbf{k}| > k_\mathrm{F}$) are occupied (unoccupied) where k_F denotes the absolute value of the Fermi wave vector. The jump can be written in terms of limits as

$$\Delta n(t) := \lim_{\mathbf{k} \to \mathbf{k}^-_\mathrm{FS}} n_{\mathbf{k}\sigma}(t) - \lim_{\mathbf{k} \to \mathbf{k}^+_\mathrm{FS}} n_{\mathbf{k}\sigma}(t) \tag{2.15}$$

with $|\mathbf{k}_\mathrm{FS}| = k_\mathrm{F}$ meaning that $\mathbf{k}_\mathrm{FS}$ is a representative of the set of wave vectors located at the Fermi surface. The limit is executed for a fixed vector orientation

given by $\mathbf{k}_{\mathrm{FS}}$ such that $|\mathbf{k}|$ approaches k_{F} from negative or positive values. For hypercubic lattices strong evidences exist that the value of (2.15) is independent of the specific representative $\mathbf{k}_{\mathrm{FS}}$ chosen [62]. The dependence between momentum distribution and jump at the Fermi surface is illustrated in figure 2.3 for a Fermi sea as initial state at $t = 0$ and in figure 2.4 for the result after a quantum quench at a larger time $t > 0$.

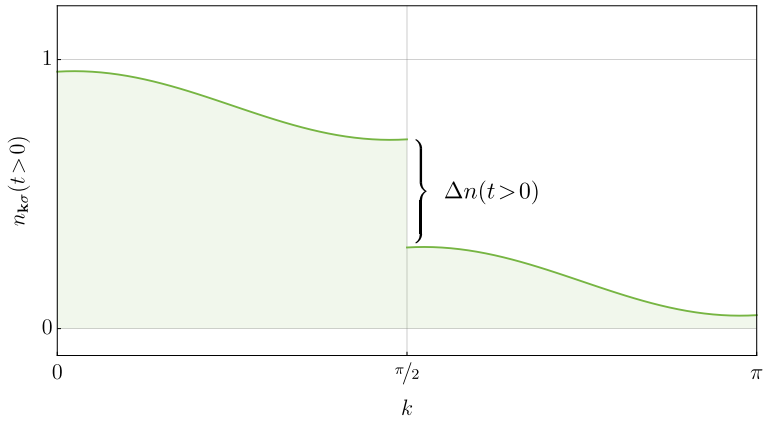

Figure 2.4: Momentum distribution $n_{\mathbf{k}\sigma}(t)$ and jump $\Delta n(t)$ for a time $t > 0$ after a quench of the form (2.7) at $t = 0$ for $U \neq 0$ in (2.4). The jump is weakened due to overall momentum conserving scattering processes.

In contrast to $n_{\mathbf{l}\sigma}(t)$ which is not affected by a quench whatsoever due to (2.12) a quench was shown [25, 26, 63–65] to have a huge impact on $n_{\mathbf{k}\sigma}(t)$ and consequently also on $\Delta n(t)$. Because of the scattering behaviour of (2.4b) electrons located near the Fermi surface are pairwise driven to leave their former states within the Fermi sea and occupy energetically higher states. The sharp jump at the Fermi surface decreases, the momentum distribution differs from the Fermi sea as shown in figure 2.4.

The jump serves as a probe to decide whether the system is thermalized or not. A discontinuity in the momentum distribution, i.e. a nonvanishing jump $\Delta n(t) \neq 0$, can only occur for the $T = 0$ ground state provided that the system is in thermal equilibrium. As a quenched system is undoubtedly in a highly excited state an occurrence of a discontinuity indicates that the system is not (yet) thermalized [63]. In a fully isolated system the excitation energy of the system after the quench has to be conserved. This total energy defines an effective system temperature which describes the final thermal equilibrium state if existing. A comparison of a numerically simulated momentum distribution via DMFT after a quench and subsequent relaxation [63] and the (equally shaped) thermal equilibrium prediction for finite temperature was done by Aoki et al. [65].

2.4 Special case: One-dimensional systems

Subsequent calculations are carried out for one-dimensional lattices. Thus, a dedicated consideration of one-dimensional correlations for $t=0$ is given here.

As both the local particle number average (2.9) and the momentum distribution, cf. equation (2.14a), directly rely on the time-dependent expectation value

$$g_{l\sigma}(t) := \langle \mathrm{FS}| f_{0\sigma}^\dagger(t) f_{l\sigma}(t) |\mathrm{FS}\rangle \tag{2.16}$$

evaluating it with respect to the Fermi sea for arbitrary times t is of importance. Being able to do so for $t > 0$ after the system was exposed to a quench is subject of the chapters to come. This involves knowledge of $g_{l\sigma}(t=0)$ which will be calculated here. A Fourier transform of the real space creation and annihilation operators in (2.16) with the aid of (2.3) yields

$$g_{l\sigma}(t=0) \;=\; \frac{1}{N}\sum_{k_1 k_2} \langle \mathrm{FS}| f_{k_1\sigma}^\dagger f_{k_2\sigma} |\mathrm{FS}\rangle \, e^{ik_2 l} \;=\; \frac{1}{N}\sum_{|k|\leq k_\mathrm{F}} e^{ikl} \tag{2.17}$$

in the case of a system of finite lattice size with a sum over all occupied momenta. The thermodynamic limit allows for a calculation of $g_{l\sigma}(t=0)$ in the case of infinite lattice sizes $N \to \infty$ as shown in figure 2.5 with

$$g_{l\sigma}(t=0) \;=\; \frac{1}{2\pi}\int_{-k_\mathrm{F}}^{k_\mathrm{F}} \mathrm{d}k \, e^{ikl} = \frac{\sin(k_\mathrm{F} l)}{\pi l}. \tag{2.18}$$

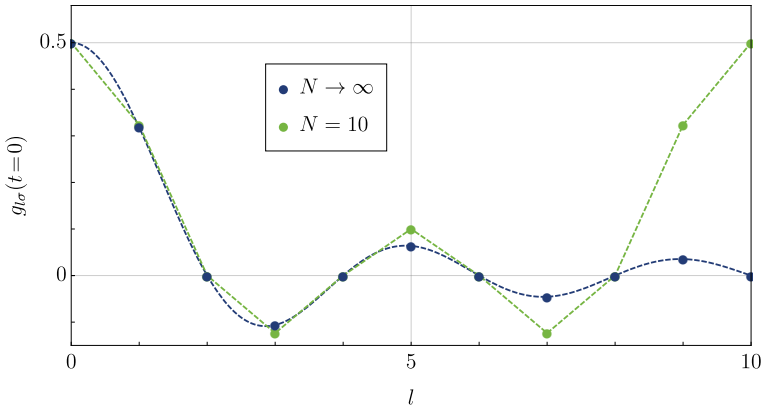

Figure 2.5: Behaviour of the time-dependent expectation value (2.16) before being exposed to a quench, $g_{l\sigma}(t=0)$ is shown for an infinite lattice and for a lattice of size $N = 10$ at half-filling. The time-dependent expectation values exist for integer distances l only. Note the periodicity in the finite size case that is implied by using a Fourier transform in (2.17).

3 Approaches to the time evolution of operators

In order to describe systems far from equilibrium whose dynamics is led by processes spread over wide energy ranges a systematic approach is needed for calculating the time dependence of operators. In the following chapter the conceptual methods being based on the Heisenberg equation of motion will be described and subsequently explained with the aid of easily accessible examples. The sections to come are of particular importance as throughout the whole thesis it will be made heavy use of techniques explained therein. The concepts presented will serve as a means to gain insight into physically relevant system properties.

Henceforth, natural units are used in which $\hbar$ is set to unity.

3.1 Heisenberg picture and equations of motion

In the Schrödinger picture of quantum mechanics the information on the evolution of the system is completely contained in bras $\langle\psi(t)|$ and kets $|\psi(t)\rangle$, respectively, and operators may have at most explicit time dependence. In contrast, in the Heisenberg picture operators $A(t)$ contain the needed information to fully describe the system and thus necessarily depend on time [66, 67]. Switching between the two pictures requires the transformation

$$A_{\mathrm{H}}(t) = U_{\mathrm{S}}^{\dagger}(t, t_0) A_{\mathrm{S}}(t) U_{\mathrm{S}}(t, t_0) \tag{3.1}$$

with the time evolution operator in its most general form

$$U_{\mathrm{S}}(t, t_0) = T_{\mathrm{D}} \exp\left(-i \int_{t_0}^{t} \mathrm{d}t'\, H_{\mathrm{S}}(t')\right). \tag{3.2}$$

In equation (3.1) and equation (3.2) the indices denote the respective picture the operator is formulated in and the argument t of Schrödinger picture operators stands for a possible explicit dependence on time as mentioned above. Since an explicit form of $U_{\mathrm{S}}(t, t_0)$ is not needed in the following and will not be used further equation (3.2) is provided for the sake of completeness only. The occurring Dyson time ordering operator

$$T_{\mathrm{D}}\left(A(t_1)B(t_2)\right) = \begin{cases} A(t_1)B(t_2) & \text{if } t_1 > t_2 \\ B(t_2)A(t_1) & \text{otherwise} \end{cases} \tag{3.3}$$

allows for a concise notation of the underlying von Neumann series.

Important characteristics of the time evolution operator are

$$U_{\mathrm{S}}(t_0, t_0) = 1 \tag{3.4a}$$

$$U_{\mathrm{S}}(t, t_0) = U_{\mathrm{S}}(t, t_1) U_{\mathrm{S}}(t_1, t_0) \tag{3.4b}$$

$$U_{\mathrm{S}}^{\dagger}(t, t_0) = U_{\mathrm{S}}^{-1}(t, t_0) = U_{\mathrm{S}}(t_0, t). \tag{3.4c}$$

As equation (3.4c) implies unitarity of the time evolution operator the transformation (3.1) is a unitary transformation which preserves expectation values and scalar products. Thus, it can be used without altering physically relevant measurable quantities.

The time dependence of operators in the Heisenberg picture can be directly derived assuming the most general case of operators in the Schrödinger picture with explicit time dependence

$$\begin{aligned} \frac{\mathrm{d}}{\mathrm{d}t} A_{\mathrm{H}}(t) = {} & \frac{\mathrm{d}}{\mathrm{d}t} \left(U_{\mathrm{S}}^{\dagger}(t, t_0) \right) A_{\mathrm{S}}(t) U_{\mathrm{S}}(t, t_0) + U_{\mathrm{S}}^{\dagger}(t, t_0) \frac{\partial A_{\mathrm{S}}(t)}{\partial t} U_{\mathrm{S}}(t, t_0) \\ & + U_{\mathrm{S}}^{\dagger}(t, t_0) A_{\mathrm{S}}(t) \frac{\mathrm{d}}{\mathrm{d}t} \left(U_{\mathrm{S}}(t, t_0) \right) \qquad (3.5a) \\ = {} & i[H_{\mathrm{H}}(t), A_{\mathrm{H}}(t)] + U_{\mathrm{S}}^{\dagger}(t, t_0) \frac{\partial A_{\mathrm{S}}(t)}{\partial t} U_{\mathrm{S}}(t, t_0). \qquad (3.5b) \end{aligned}$$

The Heisenberg equation of motion (3.5b) for operators that are completely independent of time in the Schrödinger picture, i.e. $A_{\mathrm{S}}(t) = A_{\mathrm{S}}$, becomes

$$\frac{\mathrm{d}}{\mathrm{d}t} A_{\mathrm{H}}(t) = i[H_{\mathrm{H}}(t), A_{\mathrm{H}}(t)] = i\mathcal{L}(A_{\mathrm{H}}(t)) \tag{3.6}$$

with the Liouville superoperator[1] $\mathcal{L}(.) := [H_{\mathrm{H}}(t), .]$ as a shorthand for a commutation with the Hamiltonian defining the system dynamics.

Due to the fact that all operators of interest in this thesis are constant in the Schrödinger picture the equation (3.6) will be the starting point for further calculations. It will be refrained from using indices denoting the respective picture for better readability. From now on operators depending on time are formulated in the Heisenberg picture, operators without time dependence are operators in the Schrödinger picture.

[1] The term *superoperator* for $\mathcal{L}(.)$ is chosen due to the fact that this operator uses other operators as its argument. These other operators themselves act on the used Hilbert space. Note that future calculations will consider the dynamics of $A(t)$ for $t > 0$ where the Hamiltonian (2.7) is independent of time leading to a conservative system. Thus, in particular the equivalence $H_{\mathrm{H}} = H_{\mathrm{S}} = H$ holds.

3.2 Iterated equations of motion

The iterated equations of motion (iEoM) approach [68] is a technique used to assess the time evolution of operators [25, 62, 64, 69]. Starting from the Heisenberg equation of motion (3.6) and an operator expansion usually infinite-dimensional differential equation systems arise due to the proliferating number of operators created in each further iteration step. Thus, a key aspect is choosing a sensible truncation scheme to make finding a solution numerically feasible. After a description of the fundamentals of the iEoM different possible basis choices will be outlined. Each choice implies a truncation scheme.

3.2.1 iEoM and operator expansion

Each operator of interest $A(t)$ can be written in a form in which its time dependence is completely contained in the prefactors of an operator expansion [70], i.e. a linear combination consisting of operators taken from a specific operator basis $\{A_1, \ldots, A_f\}$

$$A(t) = \sum_i h_i(t) A_i. \tag{3.7}$$

Here the operator $A(t)$ is formulated in the Heisenberg picture and the operators A_i are operators in the Schrödinger picture. Inserting (3.7) into (3.6) leads to

$$\frac{\mathrm{d}}{\mathrm{d}t} A(t) = i\mathcal{L}(A(t)) = i \sum_i h_i(t) \mathcal{L}(A_i)\,. \tag{3.8}$$

An expansion of $\mathcal{L}(A_i)$ in the chosen basis results in the linear combination

$$\mathcal{L}(A_i) = \sum_j M_{ji} A_j. \tag{3.9}$$

As only the prefactors $h_i(t)$ are time-dependent a combination of equation (3.7), (3.8) and (3.9) yields

$$\sum_i \frac{\mathrm{d}}{\mathrm{d}t} \Big(h_i(t) \Big) A_i = i \sum_{ij} M_{ji} h_i(t) A_j. \tag{3.10}$$

A coefficient comparison with respect to the basis operators on both sides of equation (3.10) results in

$$\frac{\mathrm{d}}{\mathrm{d}t} h_j(t) = i \sum_i M_{ji} h_i(t) \tag{3.11a}$$

$$\Leftrightarrow \boxed{\frac{\mathrm{d}}{\mathrm{d}t} \mathbf{h}(t) = i\mathbf{M}\mathbf{h}(t).} \tag{3.11b}$$

3.2.2 iEoM interpretation and solution

Equation (3.11) describes the influence of the matrix $\mathbf{M}$ on the time dependence of the prefactors occuring in the operator expansion (3.7). It is worth to reconsider equation (3.9) and to note that column i of $\mathbf{M}$ contains the image of A_i under application of the Liouville superoperator. Therefore, the matrix $\mathbf{M}$ will be subsequently called the Liouville matrix.

Solving the iEoM system, in other words finding a numerical function or a closed expression for $\mathbf{h}(t)$, can be done numerically as well as analytically. In both cases initial conditions must be considered. For the starting time $t=0$ it can not be of significance what operator picture is used which is why the relation

$$A(t=0) = A_1 \tag{3.12}$$

has to hold. Here it is assumed that A_1 denotes the Schrödinger picture version of the operator in question, i.e. $A_1 = A$. Thus, the final initial conditions of the first-order differential equation system with constant coefficients (3.11) read

$$h_i(0) = \begin{cases} 1 & \text{if } i = 1 \\ 0 & \text{otherwise.} \end{cases} \tag{3.13}$$

Numerical solution

As resorting to differential equation solvers is a well-known and common approach whose requirements are implemented in most modern numerical libraries only a brief formation of concepts should be given here without further ado. In explicit Runge-Kutta methods with or without adaptive error and step size control a general first-order differential equation with t being an independent variable and $\mathbf{y} = \mathbf{y}(t)$ is assumed as in

$$\frac{\mathrm{d}}{\mathrm{d}t}\mathbf{y} = \mathbf{f}(\mathbf{y}, t). \tag{3.14}$$

The time t is discretized so that $t_n = nh$, $n \in \mathbb{N}_0$, and the value of $\mathbf{y}_{n+1} = \mathbf{y}(t_{n+1})$ can be derived with the aid of information from previous steps. An approach is of order p if the cumulated error over all steps is in $\mathcal{O}(h^p)$. Adaptive methods use explicit Runge-Kutta processes of order p and error estimations of order p_e that allow for a permanent adjustment of h in order to account for the special behaviour of the function $\mathbf{f}$ describing the change in $\mathbf{y}$ with respect to former $\mathbf{y}$ and t. These concepts are often symbolized by the notation scheme $p(p_\mathrm{e})$.[2]

A numerical solution approach is used predominantly in chapters 5 and 6 for obtaining the time dependence governed by (3.11).

[2] The most notable examples for adaptive Runge-Kutta methods are the 4(5) Runge-Kutta-Fehlberg method [71], the 5(4) Dormand-Prince [72] and the 5(4) Bogacki-Shampine [73] solvers.

Analytical solution

Apart from using numerical differential equation system solvers it is always possible to analytically reduce the time dependence of $\mathbf{h}(t)$ in (3.11b) to that of the matrix eigensystem. The term eigensystem here and in the following is used synonymously for the full set of eigenvalues and corresponding eigenvectors.

Let $\mathbf{E}$ be the identity matrix with the same dimension $f \times f$ as the matrix $\mathbf{M}$. Then a vector $\mathbf{v} \in \mathbb{C}^f$ with $\mathbf{v} \neq \mathbf{0}$ is an eigenvector for the eigenvalue λ of the matrix $\mathbf{M}$ if and only if

$$\mathbf{M}\mathbf{v} = \lambda\mathbf{v} \tag{3.15a}$$

$$\Leftrightarrow \underbrace{(\mathbf{M} - \lambda\mathbf{E})}_{=:\,\mathbf{M}_\lambda}\mathbf{v} = \mathbf{0} \tag{3.15b}$$

holds. Be $p(\lambda) = \det(\mathbf{M}_\lambda)$ the characteristic polynomial of the matrix $\mathbf{M}$. If λ_i is a zero of p with algebraic multiplicity $k_i \geq 1$ exactly k_i linearly independent eigenvectors span the corresponding λ_i-eigenspace. In the case of a defective matrix, i.e. a matrix with the property of the geometric multiplicity K_i being smaller than the algebraic one

$$K_i = \ker(\mathbf{M}_{\lambda_i}) < k_i \tag{3.16}$$

for the eigenvalue λ_i, further generalized eigenvectors have to be constructed via

$$\mathbf{M}_{\lambda_i}^m\mathbf{v} = \mathbf{0} \text{ with } m \geq 2 \tag{3.17}$$

until k_i linearly independent eigenvectors are found. Applying these considerations to the differential equation system (3.11) the fundamental set of solutions $\{\mathbf{h}_1(t), \ldots, \mathbf{h}_f(t)\}$ may be derived from eigenvalues and eigenvectors [74] using

$$\mathbf{h}_i(t) = e^{\lambda_i t}\mathbf{v}_i \qquad (K_i = k_i) \tag{3.18a}$$

$$\mathbf{h}_i(t) = e^{\lambda_i t}\left(\mathbf{v}_i + t\ \mathbf{M}_{\lambda_i}\mathbf{v}_i + \ldots + \frac{t^{m-1}}{(m-1)!}\ \mathbf{M}_{\lambda_i}^{m-1}\mathbf{v}_i\right) \qquad (K_i < k_i). \tag{3.18b}$$

Analytical solution for Hermitian and symmetric matrices

A special case that is of particular interest is that of Hermitian or symmetric matrices $\mathbf{M}$ with $\mathbf{M}^\dagger = \mathbf{M}$ or $\mathbf{M}^T = \mathbf{M}$ as those matrices always possess real-valued eigenvalues with equal algebraic and geometric multiplicity. Hence, they are diagonalizable and accordingly never defective. Assuming that $\mathbf{M}^\dagger = \mathbf{M}$ in equation (3.11b) a general solution can always be built using the fundamental set from (3.18a). The solution reads

$$\mathbf{h}(t) = \sum_{j=1}^{f} \alpha_j e^{i\lambda_j t}\mathbf{v}_j \tag{3.19}$$

with the coefficient set $\{\alpha_j\}$ chosen in such a way that (3.13) is fulfilled. It might be worthwhile and instructive to look at (3.19) even from a numeric point of view: Once the time evolution of $\mathbf{h}(t)$ has been mapped onto the matrix eigensystem a calculation of each time step simply involves recomputing complex phase factors in the linear combination above.

3.3 iEoM and their application to quenches in the Fermi-Hubbard model

A crucial question to ask in the context of the concrete case of section 2.2 is which operators need to be examined further with the iEoM approach. In accordance with appendix A.3 every one-particle observable can be described in terms of the time evolution of the elementary fermionic creation and annihilation operators presented in appendix A.2. Hence, in the real space case (2.2) the time evolution of $f_{i\uparrow}^\dagger(t)$ and its Hermitian conjugate is searched for. Calculations are performed for a one-dimensional lattice, the notation scheme is chosen accordingly.

3.3.1 Monomials and clusters

The dynamics of $f_{i\uparrow}^\dagger(t)$ is governed by the kinetic hopping term H_0 and – provided that $U \neq 0$ – the interaction term H_{int} as defined in equation (2.2) which induce the operator monomial expansion. Henceforth, the terms *monomial* and *cluster of size m* are used interchangeably for a product of m elementary fermionic creation and annihilation operators of the form

$$A_i = \prod_j^m F_{\alpha_j} \tag{3.20}$$

constituting a basis operator A_i in (3.7) where $F_{\alpha_j} \in \{f_{\alpha_j}^\dagger, f_{\alpha_j}\}$ denotes either an elementary creation or an annihilation operator for Fermions with a full set of quantum numbers α_j, e.g. a combination of spin and lattice site. Evidently, a constraint for the monomials (3.20) exists: Once a particle with spin pointing upwards is added to a system with filling factor $n > 0$ for $t = 0$ at site i by $f_{i\uparrow}^\dagger(t)$ each cluster has to maintain the net balance of one additional particle. To phrase it differently, conforming to concepts originally presented in Ref. [68] and with recourse to Ref. [62] the most general ansatz for the creation operator can formally be written as

$$f_{i\uparrow}^\dagger(t) = P_i^\dagger + P_i^\dagger \left(P^\dagger H^\dagger\right)_i + \dots \tag{3.21}$$

where $P_i^\dagger \left(H_i^\dagger\right)$ is a superposition of all particle (hole) creation operators that act on all sites $i \pm \delta$ within reach from site i for the elapsed time t and the maximum

velocity $v_{\max}$ quasi-particles may travel with. Figure 3.1 shows which lattice sites participate in (3.21) for a given time t. An explicit form for the superposition of particle creation operators reads

$$P_i^\dagger := \sum_{\delta \leq v_{\max} t} \sum_{\sigma} h^*_{i\pm\delta,\sigma}(t) f^\dagger_{i\pm\delta,\sigma} \tag{3.22}$$

with δ being an integer multiple of the lattice constant. An upper bound $v_{\max}$ for the group velocity in quantum systems, i.e. the speed information can propagate with, is given by Lieb and Robinson [75].

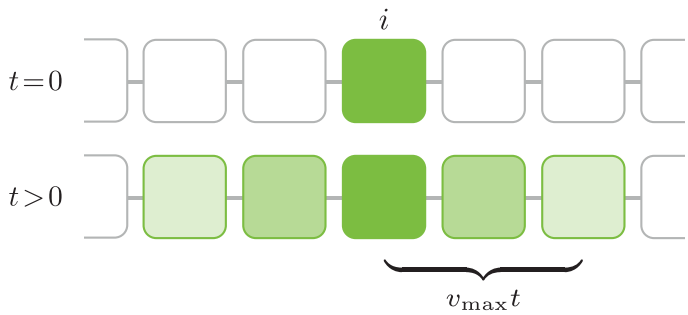

Figure 3.1: Lattice sites that occur in (3.21) for both $t = 0$ and $t > 0$. Colored sites actively participate, white sites are exponentially suppressed, the darker the color, the smaller the minimum time t the site contributes operators. Equal colors mean equal activation times for the site. For $t = 0$ only the site i, where the additional particle is injected, delivers operators. For $t > 0$ neighbouring sites within the lattice range $[i - v_{\max}t,\, i + v_{\max}t]$ also contribute.

3.3.2 Fermi-Hubbard model revisited

The main purpose of this section is to graphically illustrate the inherent connection between monomial creation and physical processes such as quasi-particle movement through the lattice as well as creation of quasi-particles. To understand the individual contributions regarding operator clusters from a mathematical viewpoint each part of the Hamiltonian is applied individually as described in (3.6). Time-dependent prefactors are omitted for brevity and $\mathcal{L}_p(.)$ means a commutation with H_p. Green (red) colored arrows stand for particles (holes), the spin direction is described by the arrow orientation.

Kinetic part

To study the influence of the kinetic part H_0 on cluster creation for $f^\dagger_{i\uparrow}(t)$

$$\mathcal{L}_0\left(f^\dagger_{i\uparrow}\right) = -J f^\dagger_{i-1\uparrow} - J f^\dagger_{i+1\uparrow} \tag{3.23}$$

is evaluated. This leads to one-particle contributions located at adjacent sites as can be seen in figure 3.2. A generalization is allowed: In an already existing cluster

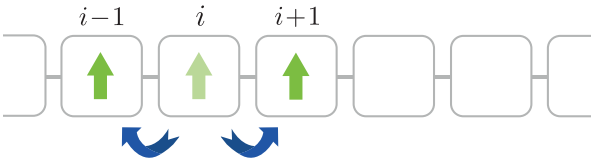

(hopping)

Figure 3.2: Possible effects of H_0 on an electron located at site i. A hop can take place to both the site $i-1$ and the site $i+1$.

of arbitrary number of particles and holes H_0 creates all clusters in which exactly one particle or hole moves to a neighbouring site. For this reason, the kinetic part of the Hamiltonian, H_0, is often referred to as hopping part.

Interaction part

Likewise, the cluster contribution of H_{int} can be studied by means of evaluating

$$\mathcal{L}_{\text{int}}\left(f_{i\uparrow}^\dagger\right) = U f_{i\uparrow}^\dagger f_{i\downarrow}^\dagger f_{i\downarrow}. \tag{3.24}$$

This process is depicted in figure 3.3. A cluster consisting of one electron located at site i is enlarged and becomes a cluster with three quasi-particles. A generalization of commutation with H_{int} to larger clusters is easily possible: One single application of the interaction part to a given monomial creates all possible clusters[3] in which exactly one of the fermionic creation or annihilation operators constituting the cluster is extended in analogy to (3.24).

Combination of hopping and interaction

Combining the effects of both elementary parts of the Fermi-Hubbard Hamiltonian leads to contributions as in

$$\mathcal{L}_0\left(\mathcal{L}_{\text{int}}\left(f_{i\uparrow}^\dagger\right)\right) = -JU f_{i-1\uparrow}^\dagger f_{i\downarrow}^\dagger f_{i\downarrow} + \dots \tag{3.25}$$

with the first created monomial being shown in figure 3.4. Due to the fact that the hopping part H_0 gradually moves already existing fermionic operators of a given monomial through the lattice and the interaction part incessantly generates

[3] Note that depending on the quantum numbers in a specific cluster, i.e. site and spin, not all operators of the cluster can always be expanded as (3.24) predicts. As an instructive example consider $\mathcal{L}_{\text{int}}\left(f_{m\uparrow}^\dagger f_{n\downarrow}^\dagger f_{o\downarrow}\right) = U f_{m\uparrow}^\dagger f_{m\downarrow}^\dagger f_{m\downarrow} f_{n\downarrow}^\dagger f_{o\downarrow} + \dots = U f_{m\uparrow}^\dagger f_{m\downarrow}^\dagger (\delta_{nm} - f_{n\downarrow}^\dagger f_{m\downarrow}) f_{o\downarrow} + \dots$ that does not lead to a nonvanishing expansion of $f_{m\uparrow}^\dagger$ in the case of $m = n$ due to equation (A.9).

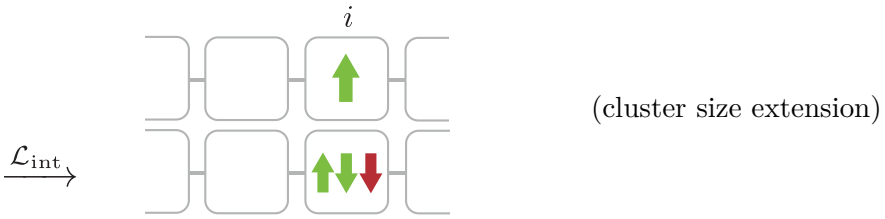

Figure 3.3: Exemplary effect of H_{int} on an electron located at site i. A cluster of three quasi-particles with two electrons and one hole is created. The cluster position in the lattice does not change.

monomials with increasing numbers of related operators it becomes impossible to provide a complete set of operators $\{A_i\}$. Note especially that it is possible to construct operator bases that are either closed under application of $\mathcal{L}_0(.)$ or of $\mathcal{L}_{\text{int}}(.)$ but none that is closed under application of both.

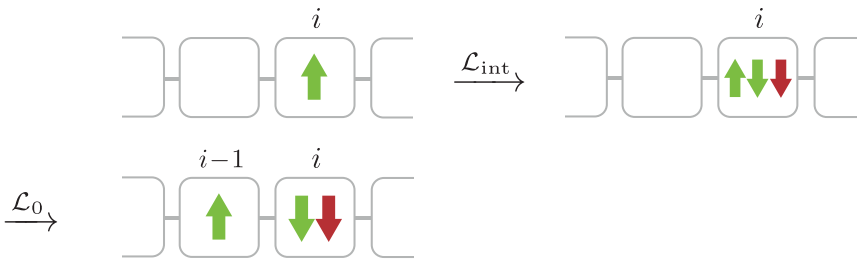

Figure 3.4: Combined effect of H_{int} and H_0 on an electron located at site i. At first, a cluster of three quasi-particles with two electrons and one hole is created whereupon one electron is moved from site i to site $i-1$. Further in the second step created monomials are not shown here.

In a finite system without interaction, i.e. $U = 0$, a complete set of operator monomials would consist of

$$f_{i\uparrow}^{\dagger} \text{ for } i \in \{1, \ldots, N\} \tag{3.26}$$

with N signifying the lattice size. This choice does not remain valid for $U \neq 0$ which is why reasonable truncation schemes have to be chosen. Possibilities for doing so will be outlined now.

3.4 Approaches for determining operator bases

Finding a reasonable operator basis $\{A_i\}$ to be used within equation (3.7) can be done in different ways all of which have specific properties, advantages and

shortcomings. While former studies [25, 26, 62] used what is generally called an m-loop approach it shows that in the context of this strategy non-unitary effects on operator level emerge (cf. especially Ref. [62]). In the following, an alternative is presented that does not suffer from these constraints and establishes operator unitarity. Note that this operator unitarity does not imply unitarity with respect to states as analyzed in Ref. [62]. Before the alternative approach is discussed in detail the m-loop is recapitulated briefly at first.

3.4.1 m-loop approach

The main idea of the m-loop approach is to gradually add operators during the calculation as they arise. Assume again the time dependence of $A(t) = A_1(t)$ is searched for. Obviously, the corresponding operator A_1 has to be part of the basis before the first loop, i.e. the first application of $\mathcal{L}(.)$, starts. The dynamics of

$$A(t) = h_1(t)A_1 \qquad \text{(Initial condition)} \tag{3.27}$$

is driven by the Hamiltonian via (3.6). Employing the general form (3.9) of the application of the Liouville superoperator new operators may appear. Let O_m denote the set of basis operators created in the $m-1$st loop, i.e. $O_1 = \{A_1\}$ due to initialization, and let there be $k_m \geq 0$ newly created operators in the mth step. Hence, for the first loop the result reads

$$\xRightarrow{\mathcal{L}(O_1)} A(t) = \sum_{i=1}^{k_1+1} h_i(t)A_i \qquad \text{(Expansion after 1st loop)} \tag{3.28}$$

as the new linear combination for the operator in question. In an m-loop approach the looping takes place $m-1$ times as described above step by step increasing the basis size to $f = 1 + \sum_{i=1}^{m-1} k_i$ operators in total. The resulting final operator expansion can be written in direct analogy to equation (3.28) as

$$\xRightarrow{\mathcal{L}(O_{m-1})} A(t) = \sum_{i=1}^{f} h_i(t)A_i \qquad \text{(Final operator expansion)} \tag{3.29}$$

in the second last step. Operators appearing in the final mth loop for the first time are neglected and only the projection of each of the $\mathcal{L}(A_i)$ onto the subspace spanned by already considered operators is kept. Consequently, the final differential equation system consists of all operators $\{A_1, \ldots, A_f\}$ having appeared in the first $m-1$ loops such that

$$\mathbf{h}(t) = \Big(h_1(t), h_2(t), \ldots, h_f(t)\Big)^T \tag{3.30}$$

and $M \in \mathbb{C}^{f\times f}$ for the Liouville matrix in equation (3.11b).

Ambiguity issues

A subtle difficulty shows up when this approach is applied to operators in second quantization as discussed in appendix A. Operators resulting from the application of $\mathcal{L}(.)$ can be written in different forms with varying numbers of quasi-particles (QP), e.g.

$$\underbrace{f_{0\uparrow}^{\dagger} f_{0\downarrow}^{\dagger} f_{0\downarrow}}_{3\text{ QP}} = \underbrace{f_{0\uparrow}^{\dagger}}_{1\text{ QP}} - \underbrace{f_{0\uparrow}^{\dagger} f_{0\downarrow} f_{0\downarrow}^{\dagger}}_{3\text{ QP}}, \tag{3.31}$$

leaving it unclear how to match the created coefficients with the individual basis operators and to form the Liouville matrix. A possibility to overcome this obstacle is to use an operator form without hidden contributions from terms with different numbers of quasi-particles. This is achieved by normal-ordering.

Normal-ordering

A usual representation is Wick's normal-ordering [76, 77] in which an operator A is described in terms of fluctuations around its mean value with

$$:A: = A - \langle A \rangle \,. \tag{3.32}$$

Transferring an operator product to its fully normal-ordered form involves

$$\begin{aligned} A_1 A_2 A_3 \ldots A_n = {} & :A_1 A_2 A_3 \ldots A_n: \\ & + \langle A_1 A_2 \rangle :A_3 \ldots A_n: + \text{all summands with one contraction} \\ & + \langle A_1 A_2 \rangle \langle A_3 A_4 \rangle :A_5 \ldots A_n: + \text{all summands with two contractions} \\ & + \ldots \\ & + \text{all summands with maximum number of contractions.} \end{aligned} \tag{3.33}$$

Note that for (3.31) an unambiguous matching is now possible as a normal-ordered operator product of k creation and l annihilation operators solely describes the contribution of a $k + l$ quasi-particle term. In practice, a further convention is needed to handle the arbitrary order of creation and annihilation operators.

3.4.2 Orthonormality with respect to a scalar product

Another possibility to choose an operator basis is to construct it beforehand with respect to a given scalar product. For this purpose the Frobenius scalar product $(A|B)$ according to equation (B.1) will be used. Proofs of properties of the Frobenius scalar product and further details are discussed extensively in appendix B. For now it is sufficient to reconsider the choice of a scalar product from a physical perspective.

The Frobenius scalar product $(A|B)$ can be seen as the high-temperature limit $T \to \infty$ of the thermal expectation value

$$(A|B) = \lim_{T\to\infty} \left\langle A^\dagger B \right\rangle = \lim_{T\to\infty} \operatorname{Tr}\left(\rho A^\dagger B\right) \tag{3.34}$$

in the canonical ensemble with the density matrix operator ρ following for a Hamiltonian H and the inverse temperature $\beta > 0$ from

$$\rho = \frac{e^{-\beta H}}{\operatorname{Tr}\left(e^{-\beta H}\right)} \tag{3.35}$$

such that the considered system is maximally disordered and each state is equally likely with

$$\lim_{T\to\infty} \rho \propto \mathbb{1}. \tag{3.36}$$

Note that equation (3.34) requires a finite local Hilbert space. This prerequisite is fulfilled in the Fermi-Hubbard model. Furthermore, only local pairings can produce finite contributions to the expectation value because all other correlations vanish.

Let $\{A_i\}$ be an orthonormal operator basis which thus fulfills the requirement

$$(A_i|A_j) = \delta_{ij}, \tag{3.37}$$

i.e. an operator basis that does not possess a finite overlap between pairwise different basis monomials with respect to the Frobenius scalar product. Accordingly, the Liouville matrix $\mathbf{M}$ in (3.11b) can be constructed by determining the overlap of a basis monomial A_j and the result of the application of the Liouville superoperator to a basis monomial A_i as in

$$M_{ji} = (A_j|\mathcal{L}(A_i))\,. \tag{3.38}$$

The resulting Liouville matrix $\mathbf{M}$ is Hermitian, i.e. $\mathbf{M} = \mathbf{M}^\dagger$, due to the relation

$$\begin{aligned}
M_{ji} &= (A_j|\mathcal{L}(A_i)) = \mathcal{N}\operatorname{Tr}\left(A_j^\dagger [H, A_i]\right) && \text{(3.39a)}\\
&= \mathcal{N}\operatorname{Tr}\left(A_j^\dagger \left(HA_i - A_i H\right)\right) = \mathcal{N}\operatorname{Tr}\left(A_i \left(A_j^\dagger H - H A_j^\dagger\right)\right) && \text{(3.39b)}\\
&= \mathcal{N}\operatorname{Tr}\left(A_i \left(HA_j - A_j H\right)^\dagger\right) = \mathcal{N}\operatorname{Tr}\left(A_i \mathcal{L}^\dagger\left(A_j\right)\right) && \text{(3.39c)}\\
&= (\mathcal{L}(A_j)|A_i) = (A_i|\mathcal{L}(A_j))^* = M_{ij}^*. && \text{(3.39d)}
\end{aligned}$$

Here it was made use of the invariance of the trace under cyclic permutation, the equation (B.2) and the general notation of appendix B. A proof of the self-adjointness of the Liouville superoperator is inherently contained in (3.39) as well. By definition

$$\left(A_j \,\middle|\, \mathcal{L}(A_i)\right) = \left(\mathcal{L}^\dagger\left(A_j\right) \,\middle|\, A_i\right) \tag{3.40}$$

holds which is why the green colored parts of equation (3.39) directly imply

$$\mathcal{L} = \mathcal{L}^\dagger. \tag{3.41}$$

The hermiticity of the Liouville matrix is the central difference between this method and the m-loop approach described in section 3.4.1. In general, the Liouville matrix resulting from an m-loop approach is *not* Hermitian.

Due to a Hermitian Liouville matrix the method presented in this section ensures that solutions always assume the form of equation (3.19) with real-valued eigenvalues λ_i. The time evolution is unitary with respect to operators and the solution thus only has oscillatory parts. Since the Liouville matrix of an m-loop approach in general possesses complex-valued eigenvalues the fundamental system shows exponentially increasing or decreasing components.

Another slightly less obvious difference is the possibility to create highly problem-specific operator bases with the scalar product approach. Considering the Fermi-Hubbard model again, this means that while an m-loop approach is restricted to including all occurring operator monomials without exception the scalar product method renders it possible to only include monomials known to be important for special cases, e.g. for the insulator or metal regime with $U/J \gg 1$ or $U/J \ll 1$, respectively.

These two aspects are huge advantages of the scalar product approach even from a computational point of view given the findings of section 3.2.2 for the calculation of eigenvalues and eigenvectors. First, a Hermitian matrix allows for the application of highly specialized algorithms.[4] Second, a smaller basis size will result in noticeably faster computation.[5]

3.5 Examples

Here, the contents of the former sections 3.2 to 3.4 are illustrated. Both a 2-loop approach with Wick's normal-ordering and the scalar product approach with an appropriate operator basis are discussed and compared on the basis of the Hamiltonian (2.2). Further different basis choices and their respective properties will be discussed more extensively in chapter 5.

[4] Provided that only a subset of eigenvalues and eigenvectors is needed, algorithms like the Arnoldi iteration [78] can be used. In the case of Hermitian matrices the iteration considerably simplifies and becomes the faster Lanczos algorithm [79], see section 4.1.2 for further details.

[5] Both in the case that only a subset of eigenvalues and eigenvectors is needed and in the case that a full eigensystem decomposition is searched for the basis size has an impact on the performance. In the first case, a smaller basis size leads to a smaller Liouville matrix and matrix vector multiplications within the Arnoldi iteration are faster. In the second case, the overall computation time rises due to a time complexity like $\mathcal{O}\left(f^3\right)$ for an exact diagonalization of a Liouville matrix in a f-dimensional basis.

The following calculations intentionally take place in momentum space to emphasize the universality of the concepts described above and to clarify that those approaches are by far not limited to real space. What is more, the number of loops and the size of the operator basis in the scalar product approach are deliberately reduced to bare minimum to keep the examples instructive and transparent. All commutations in the rest of this chapter take place in real space while the finally calculated operators are momentum space operators as desired.

3.5.1 Exact solution for vanishing interaction

Even though implicitly already done in section 2.1.2 by diagonalization of the real space Hamiltonian (2.2) the case of vanishing on-site repulsion with $U = 0$ shall be explicitly treated here by means of the aforementioned techniques. By doing so, a reference for the time dependence of the fermionic creation operator $f^\dagger_{k\uparrow}(t)$ will be gained that has to be reproduced by the approximate truncation results of the next section in the limit $U \to 0$.

Starting from the operator of interest by using its definition (2.3a), assuming the general time dependence (3.27) and inserting it into (3.6) results in a commutation with the hopping part H_0 which leads to

$$\frac{\mathrm{d}}{\mathrm{d}t} f^\dagger_{k\uparrow}(t) = \frac{1}{\sqrt{N}} \sum_m i\mathcal{L}_0\left(f^\dagger_{m\uparrow}(t)\right) e^{ikm} \tag{3.42a}$$

$$= \frac{1}{\sqrt{N}} \sum_m -Ji\left(f^\dagger_{m-1\uparrow}(t) + f^\dagger_{m+1\uparrow}(t)\right) e^{ikm} \tag{3.42b}$$

$$= \frac{1}{\sqrt{N}} \sum_m -Ji\left(f^\dagger_{m-1\uparrow}(t)\, e^{ik(m-1)} e^{ik} + f^\dagger_{m+1\uparrow}(t)\, e^{ik(m+1)} e^{-ik}\right) \tag{3.42c}$$

$$= -2Ji\cos(k) f^\dagger_{k\uparrow}(t) \tag{3.42d}$$

for a lattice constant set to unity. No further operators are created and the Fourier transform of the set of one-particle operators (3.26) suffices to describe the system which means $f = 1$ in (3.29) in momentum space. Solving the differential equation (3.42) requires the initial condition (3.12), i.e.

$$f^\dagger_{k\uparrow}(t{=}0) \stackrel{!}{=} f^\dagger_{k\uparrow}, \tag{3.43}$$

which leads to the analytic expression for the time dependence of the fermionic creation operator in momentum space of

$$f^\dagger_{k\uparrow}(t) = e^{-2Ji\cos(k)t} f^\dagger_{k\uparrow}. \tag{3.44}$$

Obviously, the momentum distribution (2.13) does not change over time due to

$$n_{k\uparrow}(t) = \langle \mathrm{FS}| e^{-2Ji\cos(k)t} f^\dagger_{k\uparrow} e^{2Ji\cos(k)t} f_{k\uparrow} |\mathrm{FS}\rangle = n_{k\uparrow}(t{=}0) \tag{3.45}$$

with a jump at the Fermi surface of $\Delta n(t) = 1$ leading to an overall qualitative behaviour as shown in figure 2.3.

3.5.2 Truncation schemes for nonvanishing interaction

2-loop approach

In the case of a nonvanishing interaction further commutations with H_{int} lead to never-ending creations of new operators. The 2-loop approach ensures that only operators created in the first loop are taken into consideration to achieve a finite basis, cf. equation (3.29). While the first commutation in order to generate the operator basis can be done explicitly a graphical approach according to section 3.3.2 is easier here. The hopping due to $\mathcal{L}_0(.)$ is completely contained in $f^\dagger_{k\uparrow}$ as shown in section 3.5.1, the on-site repulsion in $\mathcal{L}_{\mathrm{int}}(.)$ gives rise to a fully local cluster extension. To account for this extension, the definition of a Fourier transform of three-particle operators located at the very same lattice site is used with

$$f^\dagger_\uparrow f^\dagger_\downarrow f_\downarrow\big|_k := \frac{1}{\sqrt{N}} \sum_m f^\dagger_{m\uparrow} f^\dagger_{m\downarrow} f_{m\downarrow} e^{ikm}. \tag{3.46}$$

To avoid ambiguity regarding operator matching normal-ordering as given by (3.33) is imposed and the final operator basis takes the form

$$A_1 = a_1 f^\dagger_{k\uparrow} \tag{3.47a}$$

$$A_2 = a_2 :f^\dagger_\uparrow f^\dagger_\downarrow f_\downarrow\big|_k: = a_2 f^\dagger_\uparrow f^\dagger_\downarrow f_\downarrow\big|_k - a_2 n f^\dagger_{k\uparrow} \tag{3.47b}$$

with the arbitrary basis prefactors $a_i \in \mathbb{R}^+$ and the filling factor n. Using $a_i = 1$ reproduces the original and unmodified 2-loop approach of section 3.4.1. The reason for the usage of basis prefactors $a_i \neq 1$ will become clear in subsequent sections.

To determine the matrix elements of the Liouville matrix $\mathbf{M}_{\mathrm{EoM}}$ used in the differential equation system (3.11) equation (3.9) will be used which requires commuting each individual basis operator and normal-ordering the resulting operators. The application of the Liouville superoperator to A_1 results in

$$\mathcal{L}(A_1) = -2J\cos(k) a_1 f^\dagger_{k\uparrow} + U a_1 f^\dagger_\uparrow f^\dagger_\downarrow f_\downarrow\big|_k \tag{3.48a}$$

$$= -2J\cos(k) A_1 + UnA_1 + U\frac{a_1}{a_2} A_2. \tag{3.48b}$$

The occurrence of $\mathcal{L}_0\left(f^\dagger_{m\uparrow} f^\dagger_{m\downarrow} f_{m\downarrow}\right)$ in the case of the second basis operator (3.47b) allows for hopping of exactly one quasi-particle leading to six (not normal-ordered) three-particle clusters in total. After application of normal-ordering two of them contain contributions that can not be neglected in the chosen basis, the remaining

four clusters are indicated by dots and do not have an influence on the dynamics with respect to the current truncation scheme

$$\mathcal{L}(A_2) = a_2\mathcal{L}\left(f_\uparrow^\dagger f_\downarrow^\dagger f_\downarrow\big|_k\right) - a_2 n\mathcal{L}\left(f_{k\uparrow}^\dagger\right) \tag{3.49a}$$

$$= \frac{1}{\sqrt{N}}\sum_m -Ja_2\left(nf_{m-1\uparrow}^\dagger + nf_{m+1\uparrow}^\dagger + \ldots\right)e^{ikm} \tag{3.49b}$$

$$+ Ua_2 f_\uparrow^\dagger f_\downarrow^\dagger f_\downarrow\big|_k - n\frac{a_2}{a_1}\mathcal{L}(A_1) \tag{3.49c}$$

$$= Un(1-n)\frac{a_2}{a_1}A_1 + \ldots + U(1-n)A_2. \tag{3.49d}$$

A coefficient comparison in both (3.48) and (3.49) allows for a direct identification of the M_{ji} and the matrix reads

$$\mathbf{M}_{\mathrm{EoM}} = \begin{pmatrix} -2J\cos(k) + Un & Un(1-n)\frac{a_2}{a_1} \\ U\frac{a_1}{a_2} & U(1-n) \end{pmatrix}. \tag{3.50}$$

A first conclusion can already be drawn at this early point: The matrix (3.50) is Hermitian only for the special choice

$$\frac{a_1}{a_2} = \sqrt{n(n-1)}. \tag{3.51}$$

In the case of the unmodified 2-loop approach, i.e. $a_1 = a_2 = 1$, this can not be satisfied for physically meaningful fillings.

Scalar product approach

In analogy to the basis of the 2-loop approach consisting of two operators the following basis in momentum space is chosen to be used in the scalar product approach

$$A_1 = \sqrt{2}f_{k\uparrow}^\dagger \tag{3.52a}$$

$$A_2 = \sqrt{8}f_\uparrow^\dagger f_\downarrow^\dagger f_\downarrow\big|_k - \sqrt{2}f_{k\uparrow}^\dagger. \tag{3.52b}$$

Note especially that the basis (3.52) fulfills orthonormality (3.37) as required and again captures the kinetic part as a whole due to the first basis operator A_1 in (3.52a). Calculating the Liouville matrix $\mathbf{M}_{\mathrm{SP}}$ involves determining the following three black colored generically different matrix elements

$$\mathbf{M}_{\mathrm{SP}} = \begin{pmatrix} (A_1|\mathcal{L}(A_1)) & (A_1|\mathcal{L}(A_2)) \\ (A_2|\mathcal{L}(A_1)) & (A_2|\mathcal{L}(A_2)) \end{pmatrix} \tag{3.53}$$

in momentum space whereas the green colored element follows from hermiticity (3.39). Momentum space scalar products are known if the underlying real space scalar products are available. Exemplarily, for the upper left matrix element the calculation using the scalar product (B.22a) of appendix B.3 runs as follows

$$(A_1|\mathcal{L}(A_1)) = \frac{2}{N}\sum_{m,n}\left(f_{n\uparrow}^\dagger\middle|\mathcal{L}\left(f_{m\uparrow}^\dagger\right)\right)e^{ik(m-n)} \tag{3.54a}$$

$$= \frac{1}{N}\sum_{m,n}\left(-J\delta_{n,m+1} - J\delta_{n,m-1} + \frac{U}{2}\delta_{mn}\right)e^{ik(m-n)} \tag{3.54b}$$

$$= -2J\cos(k) + \frac{U}{2}. \tag{3.54c}$$

Having determined the two remaining scalar products likewise the complete Liouville matrix for the basis choice (3.52) finally reads

$$\mathbf{M}_{\mathrm{SP}} = \begin{pmatrix} -2J\cos(k) + {}^{U}\!/_{2} & {}^{U}\!/_{2} \\ {}^{U}\!/_{2} & {}^{U}\!/_{2} \end{pmatrix}. \tag{3.55}$$

Analysis of matrices

First, the special case $U = 0$ for the derived results (3.50) and (3.55) is considered. The matrices considerably simplify possessing one nonvanishing entry only and the solution (3.44) is reproduced.

To understand the reason for the introduction of the arbitrary prefactors a_i in (3.47) the second basis operator used in the scalar product approach (3.52b) is rewritten to become

$$A_2 = \sqrt{8}\left(f_\uparrow^\dagger f_\downarrow^\dagger f_\downarrow\big|_k - \frac{1}{2}f_{k\uparrow}^\dagger\right). \tag{3.56}$$

A comparison of (3.47b) and (3.56) hints at an equality of the bases (3.47) and (3.52) for the parameter set

$$a_1 = \sqrt{2} \qquad a_2 = \sqrt{8} \qquad n = \frac{1}{2}. \tag{3.57}$$

The occurrence of equality for a special filling factor only is caused by the fact that the normalization in the case of normal-ordering is achieved by referring to a reference state, e.g. the Fermi sea, in the case of the scalar product approach by tracing over the whole Hilbert space. For this reason the filling factor n appears in (3.50) but not in (3.55). Moreover, the choice (3.57) obeys (3.51) and results in the Hermitian Liouville matrix (3.50) identical to (3.55) which indicates the complete equality of the m-loop and the scalar product approach for equal input bases conforming to (3.37).

Solution in case of the scalar product approach

After the Liouville matrix $\mathbf{M}$ has been obtained the time dependence is fully set by the differential equation system (3.11) and the concrete form

$$f^{\dagger}_{k\uparrow}(t) = h_1(t)A_1 + h_2(t)A_2 \tag{3.58}$$

of the operator expansion (3.7). The two time-dependent prefactors in (3.58) will be gained here by methods of section 3.2.2.

Following exemplary evaluations take into consideration the Frobenius scalar product case, i.e. the basis choice (3.52) and the resulting matrix (3.55) are used. Numerical results of the time-dependent coefficients $h_1(t)$ and $h_2(t)$ for varying sets of parameters J and U are depicted in figures 3.5 and 3.7 in the frequency and time domain, respectively, starting from the trivial case of completely vanishing hopping and mutual interaction strengths in the upper left corner and gradually increasing $J(U)$ along the ordinate (abscissa) in steps of one. All coefficients are superpositions (3.19) of the two eigenvectors $\mathbf{v}_{1,2}$ of the given matrix $\mathbf{M}_{\mathrm{SP}}$ that rotate in the complex plane unperturbed by each other. The rotation speed of each eigenvector is determined by the corresponding eigenvalue

$$\lambda_{1,2} = \frac{1}{2}\left(U - 2J\cos(k) \pm \sqrt{2J^2\cos(2k) + 2J^2 + U^2}\right) = 2\pi f \tag{3.59}$$

and the resulting frequency f. As none of the eigenmodes shows exponentially increasing or decreasing behaviour the coefficients can not show unphysical behaviour either. Thus, the coefficient increase is bounded as shown in the time domain representation. A decomposition of the numerically gained time-dependent coefficients into the analytically determined superposition of rotating eigenvectors is shown in figure 3.6 for different times.

For the frequency domain depiction the numerical solutions of the differential equation system are discretized where the sampling rate used for discretization is ensured to be higher than twice the maximum signal frequency to match the Nyquist-Shannon theorem for avoiding aliasing effects [80]. The frequency domain data set itself is then gained by means of fast Fourier transform.

Finally, the exact result for vanishing interaction $U = 0$ explicitly calculated in section 3.5.1 is visualized here as well in the left grid column of figures 3.5 and 3.7. According to (3.44) only one coefficient should be present that rotates in the complex plane. This prediction is verified by the two green colored circles in the time and only one single mode in the frequency domain whose only difference lies in the velocity with whom the individual trajectories are traversed as can be seen by the different arrow positions in figure 3.7 indicating the individual coefficient states at final time as well as two different frequency maxima in figure 3.5.

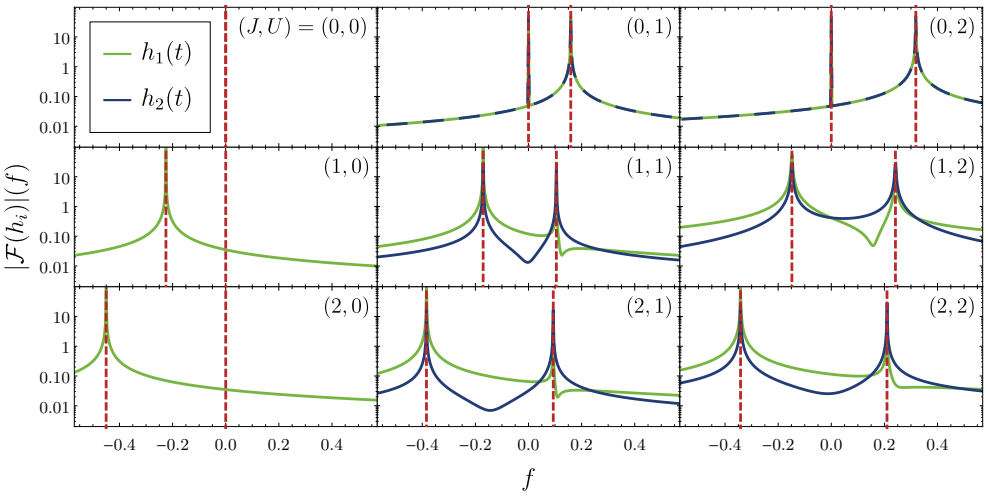

Figure 3.5: Absolute values of coefficients in the frequency domain. The frequencies of the two eigenmodes predicted by (3.59) are inserted with dashed red colored lines. For the treated momentum an arbitrary value is chosen with $k = \frac{\pi}{4}$ to gain insight into generic dynamics where k is no cosine zero, hopping (interaction) strength $J(U)$ increases from top to bottom (left to right) from zero to two in steps of one. Dashed lines in the topmost row underline the equal frequency spectra of both coefficients.

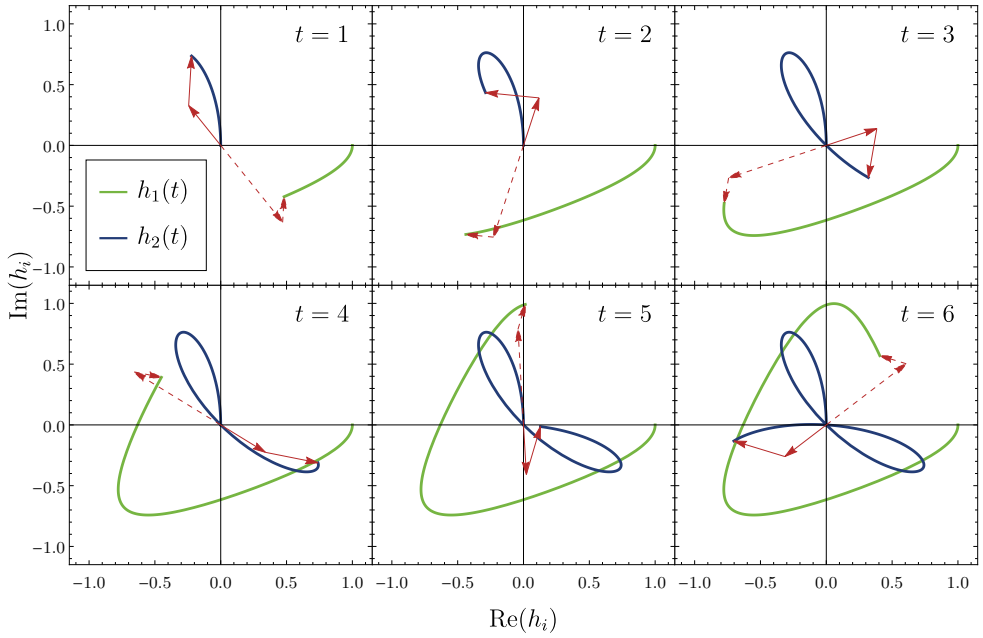

Figure 3.6: Time-dependent coefficients $h_1(t)$ and $h_2(t)$ decomposed into the matrix eigensystem. The chosen parameters are $k = \frac{\pi}{4}$, $J = 1$ and $U = 2$. Dashed (solid) red colored arrows denote the first (second) vector component in the superposition (3.19).

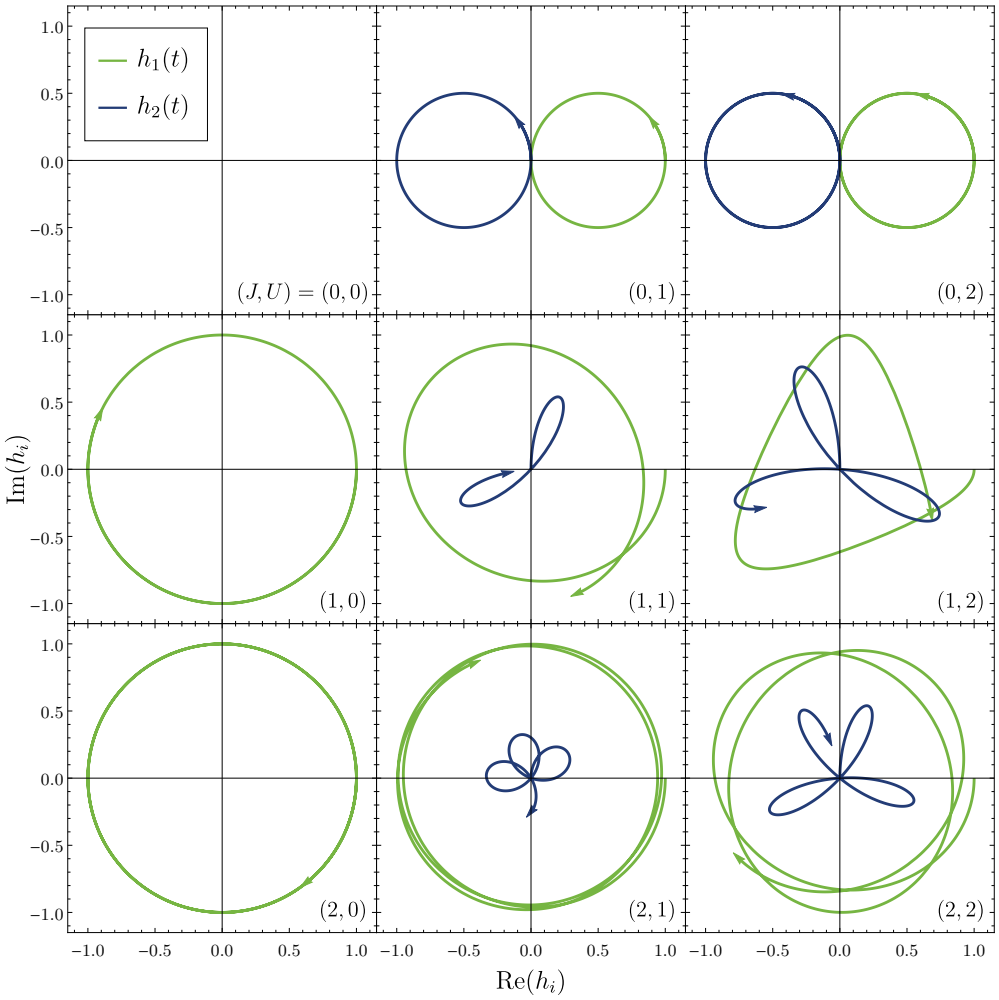

Figure 3.7: Time-dependent coefficients $h_1(t)$ and $h_2(t)$ occurring in the operator expansion (3.58) shown in the time domain. The time t increases in direction of the arrows and all plots show the same time frame $t \in [0, 7]$. An initial condition of $\mathbf{h}(t{=}0) = (1, 0)^T$ is used in accordance with (3.13) meaning the starting point for the green trajectory is always the positive valued abscissa, the blue curve starts in the origin. Explanations given below figure 3.5 regarding parameter choices apply.

Solution in case of the m-loop approach

The main motivation of this section is to emphasize the general difference between the scalar product approach analyzed in the former section and the m-loop approach. For this purpose, results of the m-loop approach for different filling factors n and interaction strengths U are shown in figure 3.8. Due to the structure of the matrix $\mathbf{M}_{\mathrm{EoM}}$ given in equation (3.50) the individual values of a_i have no impact on the solution. The ratio $\frac{a_1}{a_2}$ and its reciprocal only appear in the off-diagonal entries and cancel out when calculating the eigenvalues of the matrix. This is a special case and has to be ascribed to the small number of two basis operators and the simplicity of the example at hand.

Consequently and since the ratio $\frac{a_1}{a_2}$ does not matter, the scalar product solution is equal to the solution of the m-loop approach for half-filling and fully arbitrary factors a_i, cf. equation (3.57). This parameter choice is used to compute the green colored line in figure 3.8. For all fillings of $n \neq \frac{1}{2}$ the results of the scalar product and the m-loop approach noticeably differ from each other underlining the impact of the Fermi sea as reference state for normal-ordering in the latter approach.

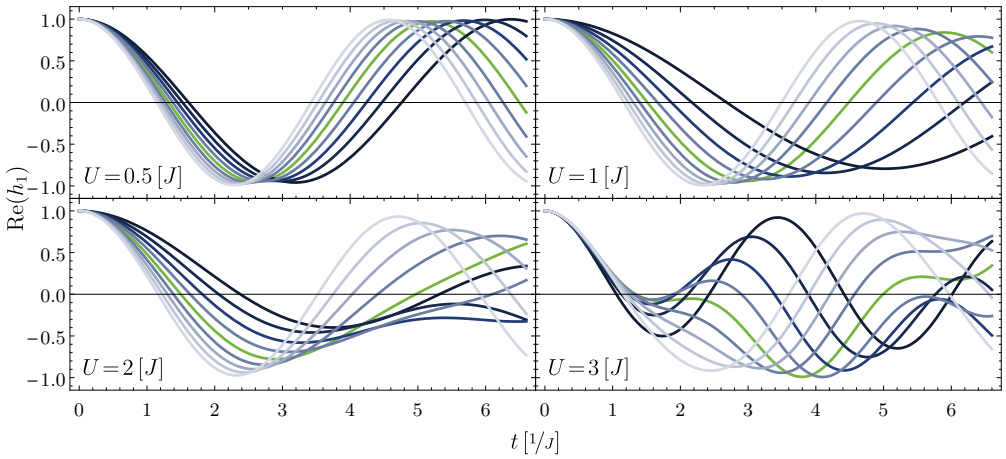

Figure 3.8: Real part of the coefficient $h_1(t)$ shown in the time domain in dependence on different filling factors n. The filling factor is increased in steps of 0.1 starting from $n = 0.1$ (light blue line) to $n = 0.9$ (dark blue line). The interaction strength U is variable, the remaining parameters are fixed to $J = 1$ and $k = \frac{\pi}{4}$. Arbitrary values of $a_i = 1$ are used. The green line denotes the case of $n = 0.5$ in the m-loop approach or the scalar product result, respectively.

The fact that the physically relevant property of filling does not have an impact on the time-dependent coefficients of a scalar product solution may seem counter-intuitive at first. To solve this apparent issue it has to be realized that the time-dependent coefficients are no physically measurable observables. Real observables like the local

particle number average $n_{l\sigma}(t)$ or the jump at the Fermi surface $\Delta n(t)$ are calculated by resorting to expectation values of the form $g_{l\sigma}(t=0)$ as defined in (2.16). These correlations are heavily influenced by the filling which is why n has an influence on the observables in the scalar product case as well.

Due to the simplicity of this example no non-unitary effects emerge in the m-loop approach and unitarity on operator level is preserved. The reason for this lies in the fact that the eigenvalues of the 2×2-Liouville matrix $\mathbf{M}_{\mathrm{EoM}}$ are always real-valued in spite of the chosen parameters. Real-valued eigenvalues ensure that the time dependence of the eigenvectors is purely oscillatory as discussed in section 3.2.2 and can not show exponentially increasing or decreasing behaviour. The absence of non-unitary effects is a mere coincidence and not the usual case that can be observed in the m-loop approach. More extensive calculations using so called full m-loop approaches which are a slightly different technique as the self-consistent approach used in the former example and as performed in, e.g., Ref. [62] prove that operator unitarity is generally broken. An example taken from this reference is depicted in figure 3.9. As can be seen, the local particle number average computed in approaches of $m \in \{2, 3, 4\}$ full loops agrees with the analytical result $n_{0\uparrow}(t) = 0.5$ only for short times until a drastic deviation can be noticed.

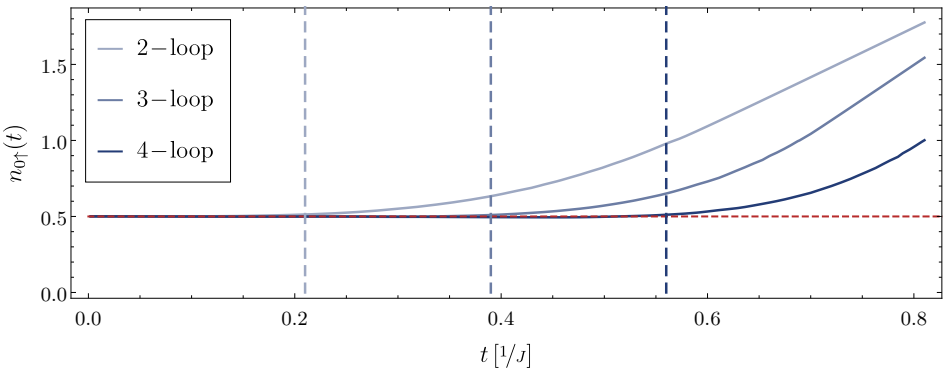

Figure 3.9: Results of a full m-loop calculation taken from Ref. [62]. The horizontal dashed red line denotes the reference value of the local particle number average for half-filling, the vertical dashed lines mark the times t where the difference of the m-loop approach and the reference value becomes more than 2 %. A higher number of loops means a longer time range the results can be trusted in. Note how small the considered time ranges are.

Though, for fairly short times, i.e. before exponentially increasing time-dependent coefficients spoil the solution altogether, and a sufficiently high number of loops the results gained by an m-loop approach may serve as a reference to compare results from the scalar product approach with. This allows for a very first benchmark of results gained by the scalar product approach.

4 Long-term behaviour of observables

To answer the initially asked questions whether a quenched system over time retains information about its initial state and adopts (quasi-)stationary states it is desirable to have access to the expectation value of macroscopic observables O in the limit of infinite times. To phrase it differently, it is asked for the infinite time average of an observable

$$O_\infty := \lim_{t\to\infty} \frac{1}{t} \int_0^t \mathrm{d}t' \left\langle O(t') \right\rangle . \tag{4.1}$$

This definition is chosen as it is the most generic one and particularly useful in cases which do not have a well-defined long-term limit

$$\langle O(t\to\infty) \rangle := \lim_{t\to\infty} \langle O(t) \rangle \tag{4.2}$$

due to nonvanishing oscillatory contributions, see figure 4.1b. If the expression $\langle O(t\to\infty) \rangle$ exists the following relation holds

$$O_\infty = \langle O(t\to\infty) \rangle . \tag{4.3}$$

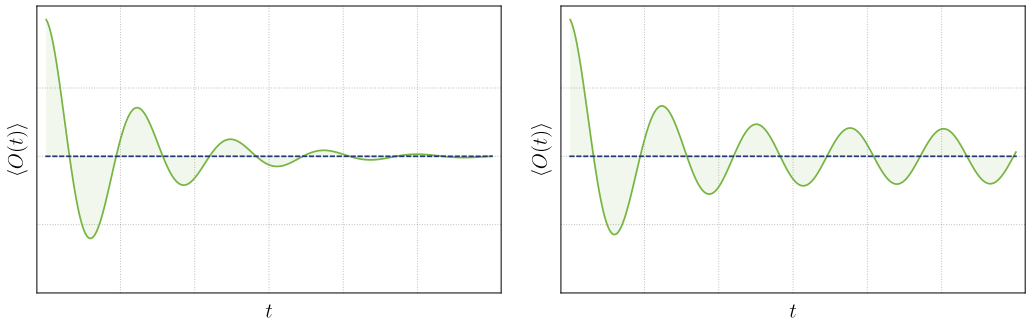

(a) Vanishing oscillatory contributions **(b)** Nonvanishing oscillatory contributions

Figure 4.1: Qualitative behaviour of arbitrary observables $O(t)$ over time. (a) oscillatory parts die out and (4.2) is well-defined, (b) oscillatory parts do not vanish and the limit (4.2) does not exist. Though, in both cases O_∞ defined in (4.1) exists (shown by the blue dashed line).

In the following, two important observables are analyzed with respect to their long-term behaviour (4.1), the expectation value of the occupation or local particle

number operator $\widehat{n}_{\mathrm{l}\sigma}$ defined in (2.9) and the jump at the Fermi surface Δn as defined in (2.15).

Regardless which observable is chosen a full decomposition of the underlying Liouville matrix into eigenvalues and eigenvectors according to section 3.2.2 is needed. This becomes problematic with an increasing number of basis operators due to the time complexity of diagonalization being cubic in the overall basis size. As a result numerically computable long-term averages for one-dimensional Fermi-Hubbard systems are limited to systems of very few sites due to the number of monomials in the expansion (3.7). Reducing the size of the matrix to diagonalize is a central aspect to achieve calculations on larger lattices. A possible approach to do so is outlined in section 4.1.2.

All calculations take place in real space and the notation assumes one-dimensional systems for brevity. A generalization of the equations is easily possible if needed. Furthermore, here and in the following operator bases are chosen which are orthonormal (3.37) and the scalar product approach from section 3.4.2 is used. This implies a Hermitian Liouville matrix governing the time evolution of prefactors in the operator expansion.

4.1 General method

4.1.1 Time-dependent prefactor products in the infinite time limit

Taking former results of section 3.3 into consideration both the expectation value of the local particle number operator and the jump at the Fermi surface can be derived from the time evolution of the fermionic creation and annihilation operators. Here an operator expansion of the form (3.7) is assumed for the fermionic annihilation operator $f_{0\uparrow}$ which directly specifies the corresponding creation operator, too, as its Hermitian conjugate

$$f_{0\uparrow} = \sum_n h_n(t) A_n \tag{4.4a}$$

$$f_{0\uparrow}^\dagger = \sum_m h_m^*(t) A_m^\dagger. \tag{4.4b}$$

Both $n_{0\uparrow}(t)$ and $\Delta n(t)$ are compound expressions. The local particle number average $n_{0\uparrow}(t)$ is a sum of products of the form $h_m^*(t)h_n(t)$ multiplied by expectation values of operators from the operator expansion $\langle A_m^\dagger A_n \rangle$, the jump at the Fermi surface $\Delta n(t)$ is basically a Fourier transform of expressions proportional to the time-dependent prefactor product $h_m^*(t)h_n(t)$.

The individual general time evolution of these prefactor products can be derived by means of (3.19) from the eigenvalues and eigenvectors of the Liouville matrix

$\mathbf{M} \in \mathbb{C}^{f\times f}$ which is at the heart of the underlying iEoM via equation (3.11b). The coefficient set $\{\alpha_i\}$ can be deduced by considering the initial condition (3.12), i.e.

$$f_{0\uparrow}(t=0) \stackrel{!}{=} f_{0\uparrow}, \tag{4.5}$$

that leads to a requirement regarding the value of the prefactors for the starting time, that is $\mathbf{h}(0)$. Let $\mathbf{V}$ be the matrix whose j-th column is the eigenvector $\mathbf{v}_j$ of $\mathbf{M}$ and let $\boldsymbol{\alpha} = (\alpha_1, \alpha_2, \ldots, \alpha_f)^T$ be the coefficient set vector. Then $\boldsymbol{\alpha}$ directly follows from solving the linear equation system

$$\mathbf{V}\boldsymbol{\alpha} = \mathbf{h}(0). \tag{4.6}$$

As coefficients and eigenvectors always appear in combination the abbreviation $\overline{\mathbf{v}}_j := \alpha_j \mathbf{v}_j$ is defined. Once the time dependence is reduced to that of the matrix eigensystem the product of time-dependent prefactors becomes

$$h_m^*(t)h_n(t) = \sum_{i,j} \overline{v}_{i,m}^* \overline{v}_{j,n} e^{i(\lambda_j - \lambda_i)t} \tag{4.7}$$

with $\overline{v}_{p,q}$ denoting the q-th component of the scaled eigenvector $\overline{\mathbf{v}}_p$. The infinite time average (4.1) can be individually applied to each product (4.7) such that

$$\lim_{t\to\infty} \frac{1}{t} \int_0^t \mathrm{d}t' h_m^*(t')h_n(t') = \sum_{i,j} \overline{v}_{i,m}^* \overline{v}_{j,n} \underbrace{\lim_{t\to\infty} \frac{1}{t} \int_0^t \mathrm{d}t' e^{i(\lambda_j - \lambda_i)t'}}_{=\delta_{\lambda_i,\lambda_j}} \tag{4.8a}$$

$$= \sum_{\substack{i,j \\ \lambda_i = \lambda_j}} \overline{v}_{i,m}^* \overline{v}_{j,n} \tag{4.8b}$$

holds. This means especially that in both $n_{0\uparrow}(t)$ and $\Delta n(t)$ only those contributions do not vanish with regard to the long-term average that are located within the same subspace spanned by eigenvectors of the same eigenvalue. The calculation (4.8) includes the possibility of degenerate eigenvalues.

4.1.2 Diagonalization techniques - a faster take

An inherent requirement of the method described in section 4.1.1 is the full diagonalization of the Liouville matrix $\mathbf{M}$. This again raises the question of numerical feasibility for large systems with a vast amount of basis operators. Consequently, a reduction of the matrix dimension becomes crucial. Each technique to do so obviously must eliminate less needed directions. The result is a new matrix

$$\widetilde{\mathbf{M}} \in \mathbb{C}^{F\times F} \text{ with } F < f \tag{4.9}$$

with new eigenvectors that span a smaller space $\widetilde{S}$ than $S = \mathrm{span}\,(\{\mathbf{v}_j\})$. As a direct result not all former vectors $\mathbf{r} \in S$ are still part of $\widetilde{S}$. Above all, a suitable algorithm has to fulfill

$$\mathbf{h}(0) \in \widetilde{S} \tag{4.10}$$

to guarantee that the initial condition (4.5) can be realized.

As a special case of the Arnoldi iteration [78] for Hermitian matrices the Lanczos algorithm [79] is well suited especially for sparse matrices due to occurring repeated matrix-vector multiplications. If the matrix is sparse noticeably less floating point operations have to be performed explicitly. While the Lanczos algorithm fulfills all the above mentioned requirements it does not fully diagonalize the newly created matrix.

Given a starting vector

$$\mathbf{s} := \mathbf{h}(0) \tag{4.11}$$

that automatically ensures (4.10) the Lanczos algorithm gradually constructs the F-dimensional Krylov space

$$\mathcal{K}^F(\mathbf{s}) = \mathrm{span}\left(\mathbf{s},\, \mathbf{M}\mathbf{s},\, \mathbf{M}^2\mathbf{s}, \ldots,\, \mathbf{M}^{F-1}\mathbf{s}\right) \tag{4.12}$$

as a subspace of $\mathbb{C}^f$. The general iteration process [81] starts by using the normalized initial vector taken from equation (4.11) as the first basis vector

$$\mathbf{b}_1 = \frac{\mathbf{s}}{\|\mathbf{s}\|} \tag{4.13a}$$

of $\mathcal{K}^F$. Further vectors $\mathbf{r}_j$ spanning the Krylov space are constructed to be mutually orthogonal and orthogonal to $\mathbf{b}_1$ by use of

$$\gamma_j = \mathbf{b}_j^\dagger \mathbf{M} \mathbf{b}_j \tag{4.13b}$$

$$\mathbf{r}_j = \mathbf{M}\mathbf{b}_j - \gamma_j \mathbf{b}_j - \beta_{j-1}\mathbf{b}_{j-1} \tag{4.13c}$$

$$\beta_j = \begin{cases} \|\mathbf{r}_j\| & \text{if } j \geq 1 \\ 0 & \text{otherwise.} \end{cases} \tag{4.13d}$$

To ensure a set of orthonormal basis vectors a normalization of $\mathbf{r}_j$ takes place

$$\mathbf{b}_{j+1} = \frac{\mathbf{r}_j}{\|\mathbf{r}_j\|}. \tag{4.13e}$$

During the Lanczos algorithm (4.13) and henceforth, the orthonormal basis vectors created in the course of the iterative process are referred to as $\mathbf{b}_j, j \in \{1, \ldots, F\}$, with

$$\mathbf{b}_i^\dagger \mathbf{b}_j = \delta_{ij} \tag{4.14}$$

where $\mathbf{b}_i^\dagger$ denotes the conjugate transpose of the vector $\mathbf{b}_i$. Expressing the former Liouville matrix $\mathbf{M}$ with respect to the basis $\{\mathbf{b}_i\}$ leads to the real-valued symmetric tridiagonal matrix

$$\widetilde{\mathbf{M}} = \begin{pmatrix} \gamma_1 & \beta_1 & 0 & \cdots & 0 & 0 \\ \beta_1 & \gamma_2 & \beta_2 & \cdots & 0 & 0 \\ 0 & \beta_2 & \gamma_3 & & 0 & 0 \\ \vdots & \vdots & & \ddots & & \vdots \\ 0 & 0 & 0 & & \gamma_{F-1} & \beta_{F-1} \\ 0 & 0 & 0 & \cdots & \beta_{F-1} & \gamma_F \end{pmatrix}. \tag{4.15}$$

Depending on the chosen Krylov space dimension F the diagonalization time to find the eigensystem of eigenvalues $\widetilde{\lambda}_j$ and eigenvectors $\mathbf{u}_j, j \in \{1, \ldots, F\}$, of the reduced Liouville matrix $\widetilde{\mathbf{M}}$ decreases significantly compared to fully diagonalizing $\mathbf{M}$.

To use the Lanczos algorithm as a mere drop-in replacement for a full diagonalization in (4.8) the resulting F-dimensional eigenvectors $\mathbf{u}_i$ have to be transformed to f-dimensional ones $\{\widetilde{\mathbf{v}}_1, \ldots, \widetilde{\mathbf{v}}_F\}$ by means of

$$\widetilde{\mathbf{v}}_i = \sum_{j=1}^{F} u_{i,j} \mathbf{b}_j \tag{4.16}$$

where $u_{i,j}$ means the j-th vector component of the eigenvector $\mathbf{u}_i$.

4.2 Observables in detail

Whilst section 4.1 mostly deals with general concepts and ideas behind eigensystem representations as well as possibilities to speed up computations in numerical matrix diagonalizations through dimension reduction this section puts the formerly explained techniques to use and provides fully analytical expressions for the infinite time averages n_∞ as well as Δn_∞.

4.2.1 Local particle number operator

Considering translational invariance the desired infinite time average of the occupation number operator is

$$n_\infty := \lim_{t\to\infty} \frac{1}{t} \int_0^t \mathrm{d}t' n_{0\uparrow}(t') \tag{4.17}$$

using the general naming scheme introduced in equation (2.9). Due to the easily accessible structure of the local particle number operator the results from section 4.1.1 can be used nearly without changes. Utilizing (4.4) and reinserting it into

equation (4.17) yields

$$n_\infty = \lim_{t\to\infty} \frac{1}{t} \int_0^t \mathrm{d}t' \sum_{m,n} h_m^*(t') h_n(t') \left\langle A_m^\dagger A_n \right\rangle . \tag{4.18}$$

The time dependence in equation (4.18) can be eliminated with the aid of (4.8) such that the infinite time average finally reads

$$n_\infty = \sum_{\substack{m,n,i,j \\ \lambda_i=\lambda_j}} \overline{v}_{i,m}^* \overline{v}_{j,n} \left\langle A_m^\dagger A_n \right\rangle \tag{4.19}$$

where the sum only applies to eigenvector components sharing the same eigenvalue $\lambda_i = \lambda_j$. Notice that (4.19) can be rewritten defining the matrix $\mathbf{A}$ with corresponding matrix elements

$$A_{mn} := \left\langle A_m^\dagger A_n \right\rangle \tag{4.20}$$

to become a repeated matrix-vector multiplication[1] for scaled eigenvectors again belonging to the same eigenvalue

$$n_\infty = \sum_{\substack{i,j \\ \lambda_i=\lambda_j}} \overline{\mathbf{v}}_i^\dagger \mathbf{A} \overline{\mathbf{v}}_j . \tag{4.21}$$

The notation in terms of matrix-vector multiplications has practical implications. The dynamics of the system and with this the strengths of the hopping J and interaction U are completely contained in the Liouville matrix. Thus, for the same basis choice the matrix $\mathbf{A}$ can be calculated only once and kept thereafter such that a fast execution of equation (4.21) for different parameter choices becomes possible. Only the diagonalization of the Liouville matrix has to be performed again for varying J and U to deliver new eigenvalues and eigenvectors.

4.2.2 Jump at the Fermi surface

In comparison with n_∞ the infinite time average of the jump at the Fermi surface Δn_∞ is slightly more complicated. Initially, a straightforward method is outlined to calculate the time-dependent jump $\Delta n(t)$ by resorting to a specific basis choice. Then, this modified approach is used to determine Δn_∞ itself.

[1] Even if calculations in this chapter are purely analytical ones and the correspondence between (4.19) and (4.21) may seem trivial at first it is, though, worth mentioning with respect to later numerical implementations. A notation in terms of matrix-vector multiplications, i.e. BLAS Level 2 routines, allows for fully vectorized simulation code. Numerical frameworks like the Intel Math Kernel Library automatically use threaded operations for these routines [82] to achieve performance gains proportional to the number of processing units.

An alternative expression for normal-ordered monomials

In order to determine the infinite time average of the jump at the Fermi surface an alternative expression to (2.15) taken from Ref. [68] can be used. A brief motivation should be given here.

Consider as an appropriate starting point an operator expansion similar to equation (3.21) of – according to (3.33) – fully normal-ordered basis operators

$$f_{i\uparrow}^{\dagger}(t) = \underbrace{\sum_{m}^{N} H_m^*(t) :f_{m\uparrow}^{\dagger}:}_{\substack{\text{one-particle} \\ \text{contributions}}} + :P_i^{\dagger}\left(P^{\dagger}H^{\dagger}\right)_i: + ... \tag{4.22}$$

with $H_m^*(t)$ denoting the time-dependent prefactor of the m-th one-particle basis operator of a lattice of N sites. Hence and in contrast to former calculations, constraints apply, i.e. the underlying operator basis is not arbitrary which is why in the following explicitly needed time-dependent prefactors are capitalized in (4.22) for better distinguishability.

Given the figures 2.3 and 2.4 as well as equation (2.15) it is clear that the value of $\Delta n(t)$ as a scaled Heaviside-like jump is a mere Fourier transform of all terms proportional to $1/r$. Any correlations within $G_\sigma(l,t)$ in equation (2.14b) are evaluated with respect to the ground state, namely the Fermi sea $|\mathrm{FS}\rangle$. Occurring correlations are built from the combination of normal-ordered basis monomials from (4.22) with the first possible combination being the one of two one-particle terms. Since

$$f_{i\sigma}^{(\dagger)} = :f_{i\sigma}^{(\dagger)}: \tag{4.23}$$

holds which implies that a single creation or annihilation operator is always normal-ordered the respective correlation of two one-particle terms reads

$$\left\langle :f_{0\sigma}^{\dagger}::f_{r\sigma}:\right\rangle = \left\langle f_{0\sigma}^{\dagger} f_{r\sigma}\right\rangle . \tag{4.24}$$

Here and in the following, the scaling behaviour of correlations in the case of an infinite lattice is considered. Finite size calculations as presented in chapter 6 are an approximation to the results of infinite lattices. According to equation (2.18) the elementary expectation value (4.24) has an asymptotic behaviour proportional to $1/r$ in the case of an infinite lattice.

The next higher correlations in $G_\sigma(l,t)$ consist of the combination of basis operators with one and three quasi-particles. According to normal-ordering rules [76] the respective contractions

$$\langle :F_{\alpha_1}::F_{\alpha_2}F_{\alpha_3}F_{\alpha_4}:\rangle = 0 \tag{4.25}$$

have to vanish. Here, $F_{\alpha_i} \in \{f_{\alpha_i}^{\dagger}, f_{\alpha_i}\}$ denotes a creation or annihilation operator of fully arbitrary quantum numbers α_i.

Correlations with an even higher number of quasi-particles decrease faster than $1/r$, e.g. the combination of two three-particle operators

$$\left\langle :f^\dagger_{\alpha_i} f_{\alpha_j} f_{\alpha_k} : : f^\dagger_{\alpha_k} f^\dagger_{\alpha_j} f_{\alpha_i} : \right\rangle \propto \frac{1}{r^3}. \tag{4.26}$$

Hence, correlations of basis monomials involving more than two one-particle basis operators do not have an impact on the jump at the Fermi surface. Pairing all possible time-dependent prefactors of one-particle contributions of the creation operator (4.22) and the related annihilation operator and Fourier transforming the result leads to

$$\Delta n(t) = \frac{1}{N^2} \sum_{m,n}^{N} H^*_m(t) H_n(t) e^{ik_\mathrm{F}(m-n)} \tag{4.27}$$

as a direct way to determine the value of the jump at the Fermi surface in a normal-ordered operator basis.

Infinite time average

Having started with (4.22) it is not fully evident if calculations need to be executed in normal-ordered form. Indeed, doing so is not needed. Instead an operator basis of choice can be used and the $H^*_m(t)$ be extracted in a subsequent step.[2]

As this case is the most general one it will be tackled hereafter. The searched for time-dependent prefactors $H_n(t)$ of normal-ordered one-particle contributions of the annihilation operator are linear combinations of the available time-dependent prefactors $h_j(t)$ of an arbitrary operator basis. In the following all t_{nj} shall be the transformation coefficients that describe the one-particle contribution of the j-th basis operator regarding lattice site n. The linear combination reads

$$H_n(t) = \sum_j t_{nj} h_j(t). \tag{4.29}$$

Thus, combining equation (4.1) and (4.29) for the prefactor product in (4.27) and further simplifying it with the aid of (4.8) by utilizing the underlying eigensystem

[2] As an example for this approach that maintains the possibility of free basis choices consider the l-th monomial that might arise in (3.21) with

$$h^*_l(t) f^\dagger_{m\uparrow} f^\dagger_{n\downarrow} f_{o\downarrow} = h^*_l(t) : f^\dagger_{m\uparrow} f^\dagger_{n\downarrow} f_{o\downarrow} : + h^*_l(t) \underbrace{\left\langle f^\dagger_{n\downarrow} f_{o\downarrow} \right\rangle}_{t^*_{ml}} : f^\dagger_{m\uparrow} : \tag{4.28}$$

which unproblematically allows for an extraction of a part of $H^*_m(t)$ even though the actual calculation might already have happened. In general, many different prefactors $h^*_i(t)$ contribute to a specific prefactor $H^*_m(t)$ such that $H^*_m(t) = f(h^*_1(t), \ldots, h^*_f(t))$ holds. Thus, knowledge of all prefactors of the former basis is needed.

of the Liouville matrix $\mathbf{M}$ leads to

$$\lim_{t\to\infty}\int_0^t \mathrm{d}t' H_m^*(t')H_n(t') = \sum_{p,q} t_{mp}^* t_{nq} \lim_{t\to\infty}\int_0^t \mathrm{d}t' h_p^*(t')h_q(t') \tag{4.30a}$$

$$= \sum_{\substack{p,q,i,j \\ \lambda_i=\lambda_j}} t_{mp}^* t_{nq} \overline{v}_{i,p}^* \overline{v}_{j,q}. \tag{4.30b}$$

Defining the site-dependent matrix $\mathbf{T^{mn}}$ as the transformation coefficient matrix[3] with matrix elements for the extraction of one-particle parts

$$T_{pq}^{mn} := t_{mp}^* t_{nq} \tag{4.31}$$

allows for an even shorter notation in which equation (4.30b) in matrix-vector notation finally becomes

$$\lim_{t\to\infty}\int_0^t \mathrm{d}t' H_m^*(t')H_n(t') = \sum_{\substack{i,j \\ \lambda_i=\lambda_j}} \overline{\mathbf{v}}_i^\dagger \mathbf{T^{mn}}\, \overline{\mathbf{v}}_j. \tag{4.32}$$

Consequently, the infinite time average of (4.27) as a summation over the pairs of one-particle contributions (4.32) takes the form

$$\Delta n_\infty = \frac{1}{N^2}\sum_{m,n}^{N}\sum_{\substack{i,j \\ \lambda_i=\lambda_j}} \overline{\mathbf{v}}_i^\dagger \mathbf{T^{mn}}\, \overline{\mathbf{v}}_j\, e^{ik_\mathrm{F}(m-n)}. \tag{4.33}$$

As with the infinite time average of the local particle number operator an extensive usage of caching is possible here as well. The matrices $\mathbf{T^{mn}}$ have to be calculated only once per chosen operator basis and can be reused thereafter. Furthermore, the computations of Δn_∞ and n_∞ can be executed in parallel since they both require a diagonalization of the same matrix $\mathbf{M}$. Avoiding to perform it twice leads to a performance gain.

[3] To understand how dense or sparse the matrix $\mathbf{T^{mn}}$ usually is consider a basis without normal-ordering on a finite lattice with N sites which has one one-particle operator per site and N^3 three-particle operators acting on up to three different lattice sites with an inherent one-particle contribution for one site each. An example for such a basis will later be called the 3-basis, cf. section 5.2.1. Thus, N^2+1 out of N^3+N operators possess a one-particle contribution for a chosen site which leads to a highly sparse filling rate for $\mathbf{T^{mn}}$ of $\left(\frac{N^2+1}{N^3+N}\right)^2$.

5 Assessing the quality of different basis choices

In the following chapter concrete realizations of operator bases will be motivated and chosen in order to calculate the time dependence of the local particle number operator (2.9) after a sudden quantum quench as explained in chapter 2 by means of methods from chapter 3. Moreover, the corresponding infinite time average using methods from chapter 4 is determined. The results will serve as a litmus test due to (2.12) to evaluate the quality of basis choices in different parameter regimes.

5.1 Periodic boundary conditions

All calculations employing finite size lattices with N sites rely on periodic boundary conditions where a given lattice site i is only determined modulo the lattice size, i.e.

$$i \equiv i + kN, \ k \in \mathbb{Z}. \tag{5.1}$$

This way a fully closed system is ensured where leakage effects can not occur and the behaviour of an infinite lattice is simulated. As a consequence, unphysical results such as a change in the expectation value of the local particle number operator (2.12) are avoided which means the lattice filling is kept constant over time.

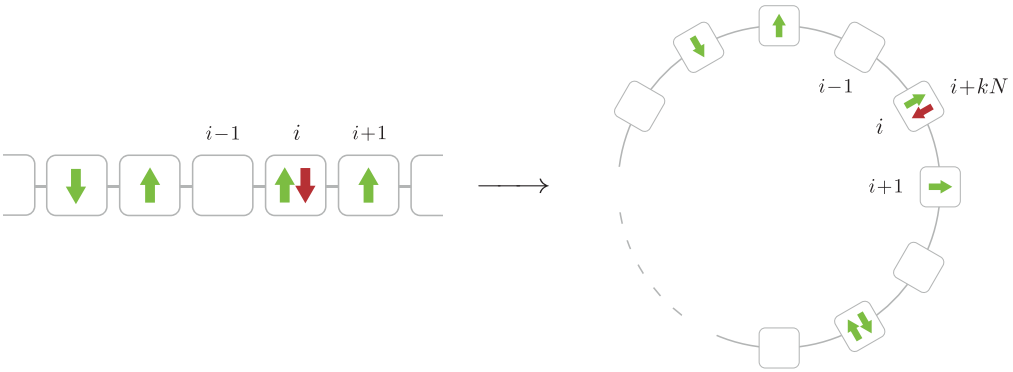

Figure 5.1: Periodic boundary conditions for a one-dimensional finite lattice of N sites can be illustrated by bending the linear lattice such that both ends meet. The lattice becomes a circle and no quasi-particles may leave the lattice via hopping. The equivalence of sites as given by (5.1) can be understood by imagining a quasi-particle having moved around the complete circle to arrive at the starting point again.

5.2 Operator bases and motivation

For explicit numerical evaluations utilizing the Frobenius scalar product approach concrete operator bases have to be chosen before a benchmarking and comparison of individual strengths and shortcomings can take place. In the following, two possible operator bases are presented that are used throughout the following chapters.

Common to the construction of both bases is a first loop according to section 3.4.1 as suitable starting point. An initial application of $\mathcal{L}(.)$ to the general operator of interest $f_{i\uparrow}^\dagger$ leads to the operator set

$$\mathcal{L}_0\left(f_{i\uparrow}^\dagger\right) \to f_{i\pm1\uparrow}^\dagger \tag{5.2a}$$

$$\mathcal{L}_{\text{int}}\left(f_{i\uparrow}^\dagger\right) \to f_{i\uparrow}^\dagger f_{i\downarrow}^\dagger f_{i\downarrow} \tag{5.2b}$$

as illustrated in section 3.3.2. To account for translational invariance inherent in the system, i.e. the fact that the choice of i has to be completely arbitrary, each operator set starting from this first loop always has to include all N one-particle monomials (5.2a) as well as all N fully local three-particle operators (5.2b). Merely the treatment of operators arising from subsequent loops remains to be specified.

5.2.1 Invariance under repeated hopping

From a mathematical viewpoint two borderline cases are present with $U/J \ll 1$ and $U/J \gg 1$. Initially, the first case of a solid of mostly metallic character is considered. Due to the overwhelming importance of the dynamics governed by the kinetic hopping part of the Hamiltonian (2.2a) in this parameter range a truncation is imposed by only allowing further applications of $\mathcal{L}_0(.)$ to the set of $2N$ operators emerged in the first loop (5.2). After orthonormalization, e.g. by means of a Gram-Schmidt process, the resulting operators fulfill (3.37) and read

$$w_1^\dagger(i) = \sqrt{2} f_{i\uparrow}^\dagger \tag{5.3a}$$

$$w_2^\dagger(i,j,k) = \left(\sqrt{2}\right)^3 f_{i\uparrow}^\dagger \left(f_{j\downarrow}^\dagger f_{k\downarrow} - \frac{1}{2}\delta_{jk}\right) \tag{5.3b}$$

for $i,j,k \in \{1,\ldots,N\}$ leading to N^3+N operators in total. Consequently, further cluster extensions are strictly omitted and the basis is invariant under hopping meaning no basis operators can be created by repeated application of $\mathcal{L}_0(.)$ to (5.3) that are not already included in this basis. The first monomials not covered by the chosen basis provided in equation (5.3) are of order $\mathcal{O}(J \cdot U^2)$. This can be intuitively understood by considering an alternating application of cluster extension

and hopping on the fermionic creation operator as in

$$f_{i\uparrow}^\dagger \xrightarrow{\mathcal{L}_{\text{int}}(.)} U f_{i\uparrow}^\dagger f_{i\downarrow}^\dagger f_{i\downarrow} \tag{5.4a}$$

$$\xrightarrow{\mathcal{L}_0(.)} JU f_{i\uparrow}^\dagger f_{i+1\downarrow}^\dagger f_{i\downarrow} + \dots \tag{5.4b}$$

$$\xrightarrow{\mathcal{L}_{\text{int}}(.)} JU^2 f_{i\uparrow}^\dagger f_{i+1\downarrow}^\dagger f_{i+1\uparrow}^\dagger f_{i+1\uparrow} f_{i\downarrow} + \dots \tag{5.4c}$$

that leads to a five operator monomial which is ignored in the current operator set.

Subsequently, this basis is referred to as 3-basis and is used to gain access to the the time dependence of observables after weak quenches, that is, a weak enforcement of on-site repulsion for $t > 0$.

5.2.2 Invariance under repeated cluster extension

The remaining parameter range $U/J \gg 1$ of an insulating solid is mostly influenced by $\mathcal{L}_{\text{int}}(.)$. Notice that already the operator set (5.2) is invariant under repeated application of this superoperator. To go a step further and to create a more promising basis the operator choice (5.3) is used as a starting point and modified to be invariant under $\mathcal{L}_{\text{int}}(.)$. As seen in (5.4c) doing so involves extending the three-particle operator (5.3b) on up to three lattice sites leading to seven new operator families extending the 3-basis by

$$\bullet\bullet\ w_3^\dagger(i,j,k) = \left(\sqrt{2}\right)^5 f_{i\uparrow}^\dagger \left(\widehat{n}_{i\downarrow} - \frac{1}{2}\right)\left(f_{j\downarrow}^\dagger f_{k\downarrow} - \frac{1}{2}\delta_{jk}\right) \tag{5.5a}$$

$$\bullet\bullet\ w_4^\dagger(i,j,k) = \left(\sqrt{2}\right)^5 f_{i\uparrow}^\dagger f_{j\downarrow}^\dagger \left(\widehat{n}_{j\uparrow} - \frac{1}{2}\right) f_{k\downarrow} \tag{5.5b}$$

$$\bullet\bullet\ w_5^\dagger(i,j,k) = \left(\sqrt{2}\right)^5 f_{i\uparrow}^\dagger f_{j\downarrow}^\dagger f_{k\downarrow} \left(\widehat{n}_{k\uparrow} - \frac{1}{2}\right) \tag{5.5c}$$

$$\bullet\ w_6^\dagger(i,j,k) = \left(\sqrt{2}\right)^7 f_{i\uparrow}^\dagger \left(\widehat{n}_{i\downarrow} - \frac{1}{2}\right) f_{j\downarrow}^\dagger \left(\widehat{n}_{j\uparrow} - \frac{1}{2}\right) f_{k\downarrow} \tag{5.5d}$$

$$\bullet\ w_7^\dagger(i,j,k) = \left(\sqrt{2}\right)^7 f_{i\uparrow}^\dagger \left(\widehat{n}_{i\downarrow} - \frac{1}{2}\right) f_{j\downarrow}^\dagger f_{k\downarrow} \left(\widehat{n}_{k\uparrow} - \frac{1}{2}\right) \tag{5.5e}$$

$$\bullet\ w_8^\dagger(i,j,k) = \left(\sqrt{2}\right)^7 f_{i\uparrow}^\dagger f_{j\downarrow}^\dagger \left(\widehat{n}_{j\uparrow} - \frac{1}{2}\right) f_{k\downarrow} \left(\widehat{n}_{k\uparrow} - \frac{1}{2}\right) \tag{5.5f}$$

$$\bullet\ w_9^\dagger(i,j,k) = \left(\sqrt{2}\right)^9 f_{i\uparrow}^\dagger \left(\widehat{n}_{i\downarrow} - \frac{1}{2}\right) f_{j\downarrow}^\dagger \left(\widehat{n}_{j\uparrow} - \frac{1}{2}\right) f_{k\downarrow} \left(\widehat{n}_{k\uparrow} - \frac{1}{2}\right). \tag{5.5g}$$

All operators of equations (5.3) and (5.5) are constructed to fulfill (3.37). Due to the explanations in footnote 3 on page 18 restrictions regarding index choices apply. A green colored dot indicates that the specific operator only exists in the case of

three distinct indices $i \neq j \neq k$, $i \neq k$ and a blue colored dot means the operator is present in addition to that if the two indices without extension are equal, e.g. $i \neq j = k$ for the basis operator (5.5a).

The basis consisting of the operators $w_1^\dagger(i)$ to $w_9^\dagger(i,j,k)$ is called 3^+-basis, well suited for strong quenches and exact up to and including monomials of order J^2. Higher orders of J account for basis operators of four and more realized lattice sites. These operators obviously can not be represented by the 3^+-basis with at most three distinct sites.

Estimating the influence of hopping - an expansion in powers of J/U

Given the fact that the 3^+-basis is constructed with the fully local physical effect of on-site interaction in mind the question arises if and to what extent results are altered by restricting the overall number of hopping processes in this basis. A motivation to do so is the expectation of being able to obtain equal results with smaller basis sizes and consequently less numerical efforts for $U \to \infty$ and fixed J.

Since we consider U/J to be considerably large its reciprocal

$$\widetilde{J} := \frac{J}{U} \tag{5.6}$$

may serve as a sufficiently small expansion parameter with $\widetilde{J} \ll 1$. This expansion is exact up to order $\widetilde{J}^2$ as the 3^+-basis is used which itself is exact up to this order.

In order to decide which basis operators are still present for a given hopping limit of L maximally allowed hops each possible index triple (i,j,k) of a three-site cluster located at sites i, j and k is examined individually. Respective clusters possess three to nine quasi-particles. Assume site s to be the starting point in the lattice from where all three quasi-particles start. Then, the minimum number of hops to reach the final positions provided in the index triple is given by

$$\xi_s = \Delta_{si} + \Delta_{sj} + \Delta_{sk} \tag{5.7}$$

where Δ_{mn} describes the shortest lattice distance from site m to site n with respect to the periodic boundary conditions (5.1), i.e. the minimum of the two distances measured clockwise and counterclockwise, respectively, which in one dimension reads

$$\Delta_{mn} = \min\left(|n-m|,\, N - |n-m|\right). \tag{5.8}$$

Since the system is translationally invariant and all three-particle operators $w_2^\dagger(i,i,i)$ are always included – even for $L = 0$ – each lattice site qualifies to be the starting point s for the calculation of (5.7). Let

$$\xi := \min_{\forall s \in S} \xi_s \tag{5.9}$$

be the overall minimum number of hops to realize the index triple assuming that S is the set containing all possible sites to start from. A naïve take to determine (5.9) would be to include all lattice sites in S. This leads to a time complexity of $\mathcal{O}(N)$.

Obviously, solving this task in faster time[1] depending on the maximum number of allowed hops is possible as well. Due to the fact that each index of the triple needs to be simultaneously reachable from the starting point in at most L hops the set S can be significantly reduced to become

$$S = \bigcap_{m=i,j,k} \{m - L, \ldots, m + L\}. \tag{5.10}$$

A three-site operator is included in the reduced basis if $\xi \leq L$ holds. Examples of index triples included in the individual sets for varying L are shown in figure 5.2.

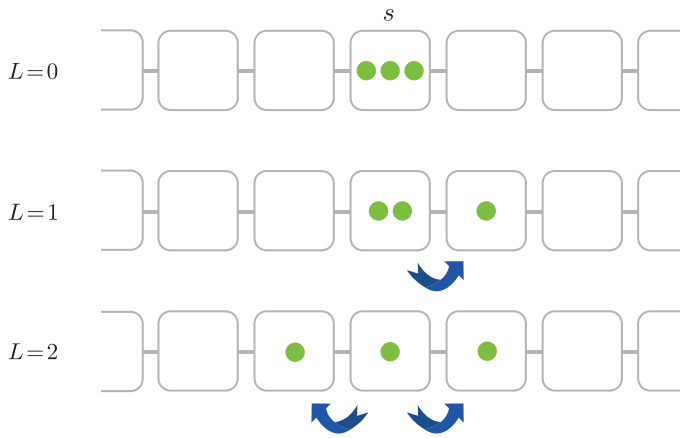

Figure 5.2: Realized sites in a hopping restriction of L maximally allowed hops. Each green colored dot means one quasi-particle monomial located at the respective site. In the given example all sites containing dots are possible starting points for hopping and part of S in (5.10). The minimally possible number of hops is annotated with blue colored arrows and measured from the site s for which $\xi = \xi_s$ holds. An infinite lattice is depicted. Note that the positions shown are exemplary and not necessarily the whole index triple set allowed for the given L.

[1] Estimating the time complexity for this approach is slightly more difficult. A general implementation might use a hash table [83] for each of the three sets of $2L + 1$ elements. Iterating through the first set takes $\mathcal{O}(L)$ time, identifying whether an element of the first set is part of the second and third one takes $\mathcal{O}(1)$ on average and $\mathcal{O}(L)$ in a worst case scenario leading to a cumulated average complexity of $\mathcal{O}(L)$.

A more specific algorithm design recognizes that all sites in the three sets of (5.10) are consecutively labeled which makes it possible to find the common range of all three sets via comparisons of the set minima and maxima. This way it is possible to determine S in constant time. S has at most $2L + 1$ elements.

5.3 Local particle number operator

Before physically relevant observables are discussed in chapter 6 both the 3-basis and the 3^+-basis are compared regarding their ability to describe the time evolution of operators in the quenched fermionic system (2.2). For this purpose the local particle number operator $\widehat{n}_{l\sigma}(t)$ will be used.

Due to translational invariance the lattice site is arbitrary and will be fixed to $l = 0$ henceforth. With the same operator expansion (4.4) as used to derive the long-term average the time-dependent local particle number operator reads

$$\widehat{n}_{0\uparrow}(t) = \sum_{m,n} h_m^*(t) h_n(t) A_m^\dagger A_n. \tag{5.11}$$

Using the notation scheme introduced in equation (2.9) the local particle number average directly follows as

$$n_{0\uparrow}(t) = \langle \widehat{n}_{0\uparrow}(t) \rangle = \sum_{m,n} h_m^*(t) h_n(t) \left\langle A_m^\dagger A_n \right\rangle. \tag{5.12}$$

For the Fermi-Hubbard model all monomials A_i are known to be of the fundamental structure (3.20) meaning each monomial is a product of the gradually created particle-hole pairs driving the dynamics. Due to the net balance of one additional particle in each cluster all monomials are odd-numbered combinations of elementary fermionic creation and annihilation operators. Consequently, the contributions $\langle A_m^\dagger A_n \rangle$ derived with respect to $|\mathrm{FS}\rangle$ in equation (5.12) are even-numbered.

Resorting to Wick's normal-ordering as given in section 3.4.1 and keeping in mind that expectation values of normal-ordered operators vanish according to (3.32) the expectation value reduces to all summands with the maximum number of contractions in (3.33). Thus, each summand is a product of Wick contractions of two elementary fermionic operators $g_{l\sigma}(t=0)$. These contractions can be calculated using (2.17) in the case of finite lattice sizes. By doing so, the local time-dependent correlation (2.16), i.e.

$$n_{0\uparrow}(t) = g_{0\uparrow}(t), \tag{5.13}$$

is completely mapped to and determined by the correlations before the quench. The dynamics and thus non-equilibrium phenomena are contained in the prefactors governed by the Liouville matrix and the differential equation system (3.11b).

Apparently and as discussed in Ref. [26], the invaluable benefit of treating the time dependence on operator level instead of using descriptions based on quantum states is the system size to be kept in memory. This applies to both the scalar product and the m-loop approach. In the first case the choice of the basis decides on the scaling behaviour. Both the 3-basis and the 3^+-basis grow polynomially with the finite lattice size. The m-loop approach even allows for dealing with infinite

lattices in the thermodynamic limit and at the same time preserving a finite number of considered operators thanks to linked-cluster properties. Up to a given order in time only a finite number of operators is created.

A dedicated approach using quantum states always requires dealing with the full exponentially growing Hilbert space. Hence, especially a treatment of the thermodynamic limit becomes infeasible and techniques like exact diagonalization are limited to very few lattice sites [84].

Results of the local particle number average using the scalar product approach are shown in figure 5.3 for both basis choices and different quench regimes at half-filling. While the analytical solution predicts a constant average number of half a particle for all times the results of both bases vary. For all shown interaction strengths U the 3^+-basis is able to keep the initial analytical result for longer times. Both bases show a characteristic first dip while the phenomenon is more pronounced in the 3-basis. Astonishingly, the dip seems to always occur in the 3-basis albeit results for large interaction, e.g. $U = 8\,[J]$, show a general tendency to be located noticeably above the reference value.

Exemplarily, long-term averages n_∞ as defined in (4.21) are calculated and inserted into figure 5.3 as an overlay. Long-term averages permit to study the common mean behaviour of observables on infinite time scales. The long-term averages of the 3^+-basis are considerably nearer to the analytical result indicating a better description of dynamics on longer time scales, too.

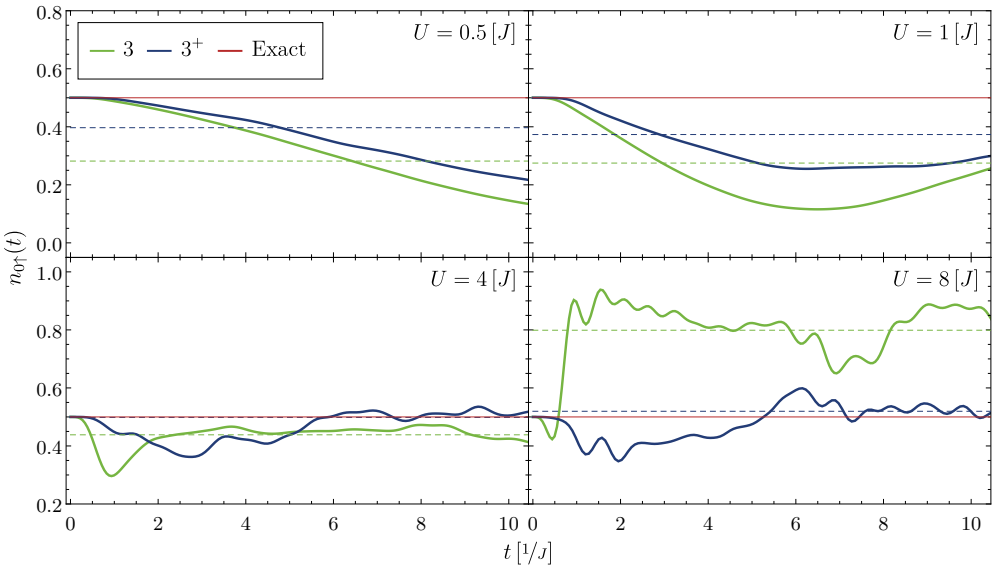

Figure 5.3: Local particle number average derived for the 3-basis and the 3^+-basis, different interaction strengths U and half-filling. The dashed long-term averages n_∞ are inserted as visual orientation. A good agreement between $n_{0\uparrow}(t)$ and n_∞ for the larger two U can be observed for the times shown.

5.4 Comparison of operator bases

Aside from the visual comparison of both operator bases using the results of the local particle number average as done in section 5.3 a more comprehensive quality assessment of the 3-basis and the 3^+-basis is desirable. To assess more detailed information both a qualitative and a quantitative criterion will be used. For the quantitative one we heavily rely on the long-term average n_∞ as motivated in section 5.3. We will call a basis superior to another if its long-term average is closer to the analytical result of the constant filling factor (2.12). Thus, the best case for a basis is $n_\infty = n$. Half-filling is used which implies $n = 1/2$.

5.4.1 Gauging the Lanczos algorithm: The minimally needed dimension of the Krylov space

To compute the long-term average n_∞ a complete diagonalization of the Liouville matrix $\mathbf{M}$ is needed as discussed in section 4.1. This becomes a practical problem because the number of basis operators increases like $\mathcal{O}(N^3)$ for both basis choices. To circumvent this problem the diagonalization is performed in the noticeably smaller Krylov space created by the Lanczos algorithm. Since information inherent in the full f-dimensional space is neglected by the construction of an F-dimensional subspace with $F \ll f$ it is unclear how accurate the calculation of n_∞ actually is.

As a way to estimate the needed dimension of the Krylov space, i.e. the number of Lanczos iterations that should be minimally performed to achieve a given accuracy, a complete diagonalization is executed at first which yields the reference result n_∞. Then, the observable $n_\infty^{(F)}$ is repeatedly calculated with the diagonalization taking place in a Krylov space created by $F \in \{F_{\text{init}}, \ldots, F_{\text{final}}\}$ iterations as shown in figure 5.4. The initial dimension F_{init} is chosen comparably small, the final dimension F_{final} such that a convergence of $n_\infty^{(F)}$ to n_∞ has occured for $F < F_{\text{final}}$.

Starting from F_{final} the data set is iterated backwards until the difference between $n_\infty^{(F)}$ and the reference result n_∞ becomes larger than a predefined accuracy goal ε. The data point with the smallest value of F still conforming to

$$n_\infty^{(F)} \in [n_\infty - \varepsilon,\, n_\infty + \varepsilon] \tag{5.14}$$

is called the minimally needed dimension for convergence. A depiction of the dimensions needed for convergence ("steps") in dependence on the interaction strength U can be found in figure 5.5 using numbers of lattice sites N for which a complete diagonalization is still feasible and an accuracy goal $\varepsilon = 10^{-4}$.

We conclude the convergence dimension to be related to the Hilbert space dimension f but not to U. Thus, we consider a result gained by the Lanczos algorithm reliable if the Krylov space dimension is at least one third of the dimension of the whole Hilbert space. This rule will be followed whenever possible.

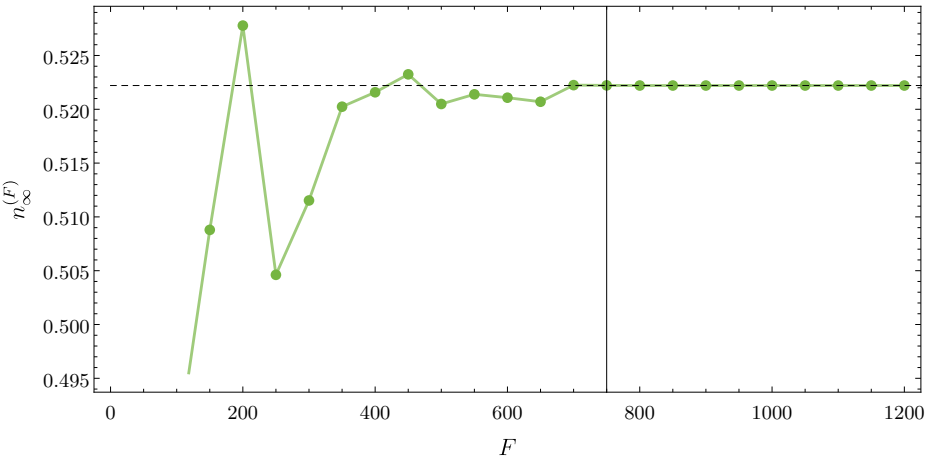

Figure 5.4: Approximation of the local particle number average $n_\infty^{(F)}$ using a Krylov space of dimension F. The dashed line denotes the reference result gained by means of a complete diagonalization in the full f-dimensional space. The solid vertical line shows the minimally needed Krylov space dimension $F = 750$ to converge to the exact result up to an accuracy of $\varepsilon = 10^{-4}$ according to (5.14). The result is obtained in a finite size calculation of $N = 8$ lattice sites for the 3^+-basis and $U = 6\,[J]$. For the calculation of $n_\infty^{(F)}$ the Krylov space was enlarged in steps of 50 with an initial (final) dimension of 50 (1200).

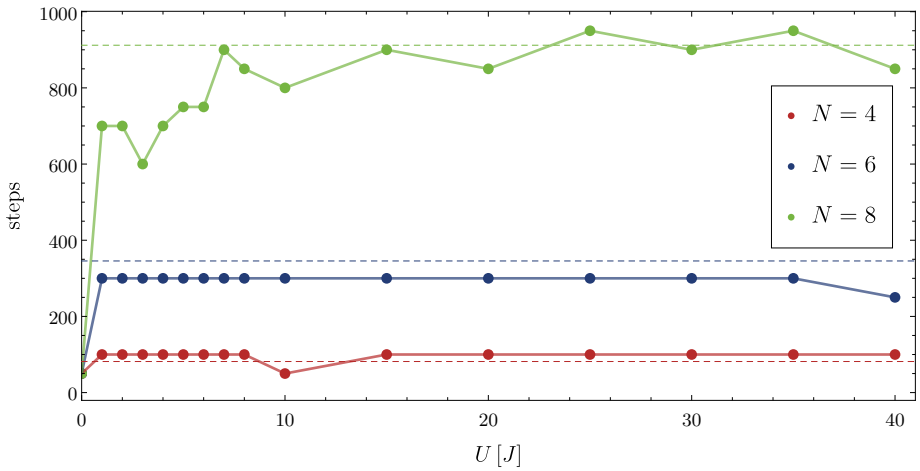

Figure 5.5: Number of Lanczos iterations ("steps") needed for the local particle number average $n_\infty^{(F)}$ to converge to the exact result of complete diagonalization n_∞ up to an accuracy of $\varepsilon = 10^{-4}$. All results are obtained in a finite size calculation of N lattice sites for the 3^+-basis, varying U and fixed $J = 1$. An example of the process to obtain one data point can be found in figure 5.4. The dashed lines denote about one third (30 %) of the Hilbert space belonging to the operator basis for N sites.

5.4.2 Quantitative comparison

As a very first step towards rating the quality of the two different operator bases the long-term averages of the 3-basis and the 3^+-basis are examined. Here and in all numerical simulations to come the hopping strength is kept to $J=1$. Thus, the parameter U explicitly describes the ratio U/J determining the strength of the sudden quantum quench.

All results are computed using the Lanczos algorithm. Due to the high number of basis operators in the 3^+-basis results for the lattice size $N = 20$ are only shown for the 3-basis. Moreover, for the case of $N = 16$ in the 3^+-basis the Lanczos algorithm was performed using 20 % of the convergence dimension proposed in section 5.4.1.

The most comprehensive basis used is the 3^+-basis which is constructed to be invariant under application of $\mathcal{L}_{\text{int}}(.)$. As a consequence, a reasonable starting point for the comparison of both operator bases is the regime of stronger quenches, i.e. quenches of $U/J \in [5, 40]$, as depicted in figure 5.6.

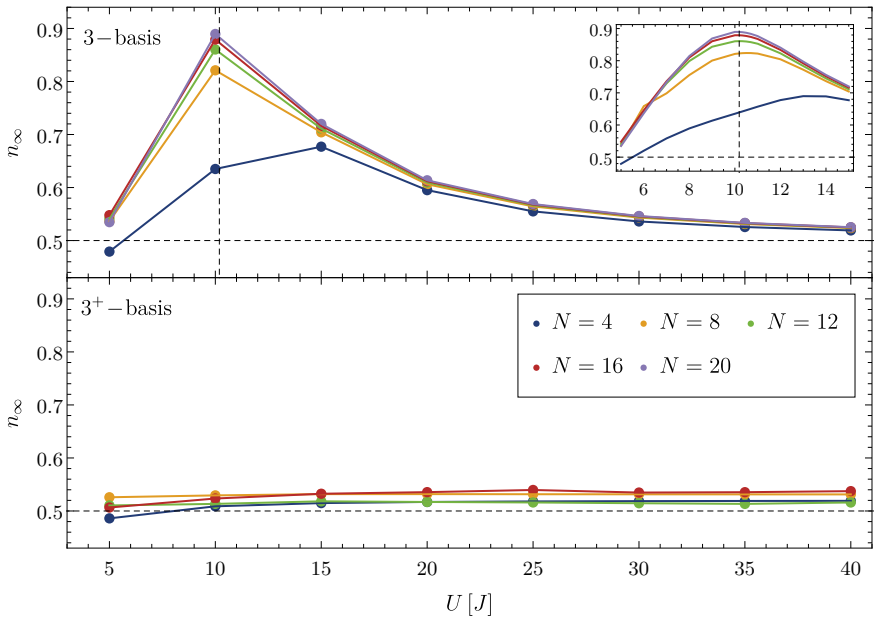

Figure 5.6: Long-term average n_∞ for the 3-basis and 3^+-basis in the regime of strong quenches. The inset shows a detailed view of the region with the highest difference between n_∞ calculated using the 3-basis and the analytical result of half-filling which is shown by the horizontal dashed line.

Three main aspects can be noticed considering the results. First, the differences of the results of the 3^+-basis and the reference value are constantly below 10 % despite the respective interaction strength U. Second, the 3-basis shows a huge deviation of

up to 80 % in the range of $U/J \in [5, 25]$. In this range the 3^+-basis shows qualitative changes, too, but on much smaller scales. Third, above $U = 25\,[J]$ both bases adopt nearly the same long-term average value of about $n_\infty \approx 0.52$.

Results of weak to intermediate quenches are shown in figure 5.7. The first data point is provided for completeness only as $U = 0$ means no occurrence of quenching at all. Without quenching an exact description of the dynamics without any truncation whatsoever can be performed in both bases. This stems from the fact that the N one-particle operators $f^\dagger_{i\uparrow}$ as included in (5.2a) are already sufficient to build a basis according to section 3.5.1. Hence, this data point may serve as a litmus test for the used numerical implementation.

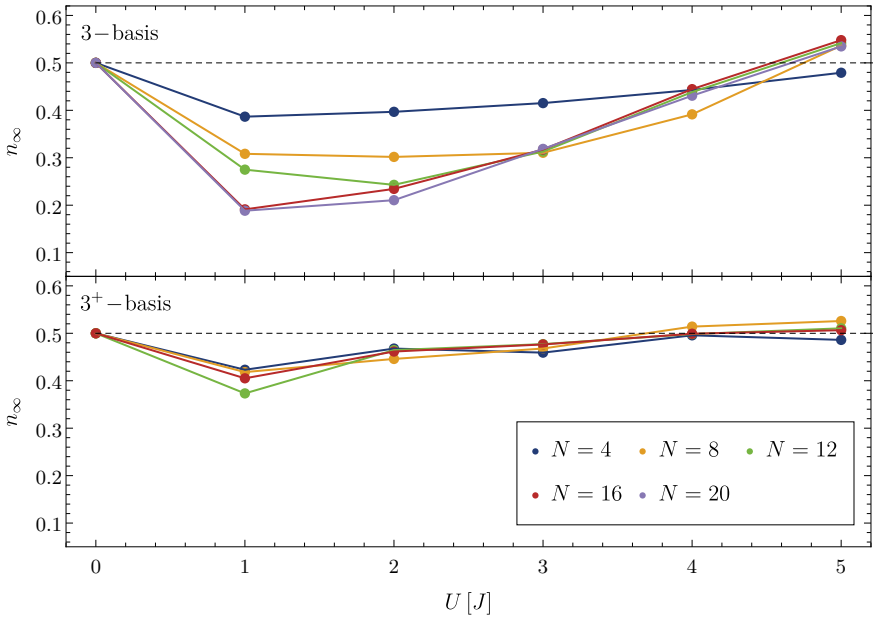

Figure 5.7: Long-term average n_∞ for both bases in the regime of weak and intermediate quenches. The analytical result is inserted using the dashed line.

As can be seen, the 3^+-basis performs better than the 3-basis throughout the whole parameter range of weak to intermediate quenches. Especially for $U = 1\,[J]$ and $U = 2\,[J]$ the former one is about twice as good as the latter one in describing the long-term dynamics. For both basis choices the comparatively worst results in this parameter range are obtained for very weak quenches of up to $U = 2\,[J]$.

5.4.3 Qualitative comparison

Obviously, the quantitative approach of section 5.4.2 can only be one aspect to rate a basis as it only measures the long-term average and therefore does not provide

reasonable information on how much the observable $n_{l\sigma}(t)$ changes in time. A smaller fluctuation of the value of the local particle number operator around its long-term average n_∞ implies a higher significance of the long-term average.

In order to quantify this overall qualitative criterion the long-term average n_∞ is used as a baseline and the oscillations of the curve are measured by summing up the squares of the areas between the time-dependent curve $n_{0\uparrow}(t)$ and the constant long-term average for a system being exposed to a quench of strength U using the variance

$$\sigma_\tau^2 = \frac{1}{\tau} \int_{t_s}^{t_s+\tau} \mathrm{d}t' \left(n_{0\uparrow}(t') - n_\infty \right)^2. \tag{5.15}$$

Since we are interested in the ability of the deduced long-term average to describe the dynamics of the system on longer time scales and to answer the question whether oscillations around the mean value die out over time or not we ignore the initial dynamics after the quench by choosing $t_s = 20 \left[\frac{1}{J}\right]$. This way possibly erratic behaviour after the quench is ignored and the focus is laid on common long-term properties. The following calculations are performed for $N \in \{4, 8, 12\}$. Exemplarily, results of σ_τ^2 derived for a lattice of $N = 12$, various U and both basis choices are shown in figure 5.8a.

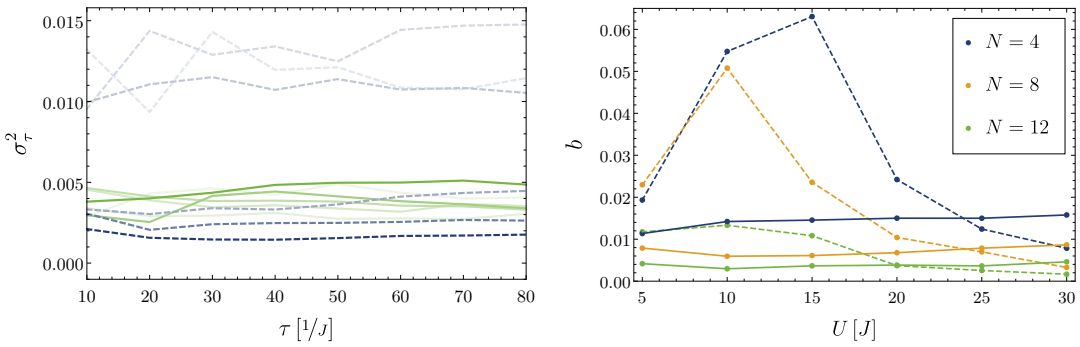

(a) Time dependence of variance

(b) Variance depending on interaction

Figure 5.8: (a) Variance σ_τ^2 measured from a starting time of $t_s = 20 \left[\frac{1}{J}\right]$ for $N = 12$ and $U = 5\,[J]$ to $U = 30\,[J]$ in steps of $5\,[J]$ (colors from light to dark). Blue (dashed) lines denote results of the 3-basis, green (solid) lines denote results of the 3^+-basis. (b) Mean values of the variance for different lattice sizes N, the 3-basis (dashed) and the 3^+-basis (solid) in dependence on U according to (5.16).

All curves in figure 5.8a can be approximately described by constant lines, i.e. the results do not depend on τ. This also applies to the results for the smaller lattice sizes $N = 4$ and $N = 8$ (not shown here). Consequently, each variance result can be characterized by

$$\sigma_\tau^2 \approx b \tag{5.16}$$

where b denotes the mean value of the data points. An essentially constant variance especially implies that oscillations of $n_{0\uparrow}(t)$ around n_∞ do not die out. Instead a qualitative behaviour of nonvanishing oscillatory contributions shown in figure 4.1b can be observed clearly.

Due to the fact that oscillations do not disappear the amount of these deviations from the long-term average becomes of importance to assess the quality of a basis. A suitable parameter for this purpose is b. A depiction of the dependence of this parameter on the interaction U is shown in figure 5.8b. While the 3^+-basis keeps the same amount of oscillations over the whole parameter range, the 3-basis shows a behaviour similar to that of the long-term average n_∞ shown in figure 5.6. For intermediate quenches noticeably worse results arise for the 3-basis compared to the 3^+-basis. For stronger quenches the relation changes and the 3-basis becomes slightly better than the 3^+-basis.

In particular, the results of the 3^+-basis which do not depend on U whatsoever suggest to assume that the amount of oscillations is a quantity decreasing with the lattice size. To verify this hypothesis the average variance $\bar{b}$ is computed by using the mean value of each curve in figure 5.8b and plotted against the inverse lattice size as depicted in figure 5.9. Both the extrapolated results for the 3-basis and the 3^+-basis are nearly zero. We attribute the impossible occurence of a slightly negative variance in the 3^+-basis to the small data set of only three different lattice sizes. In agreement with expectations the prediction for the infinite lattice shows no oscillations which lets us conclude that long-term averages are more meaningful the larger the used lattice is. Thus, especially large lattices are well characterized by the respective long-term averages.

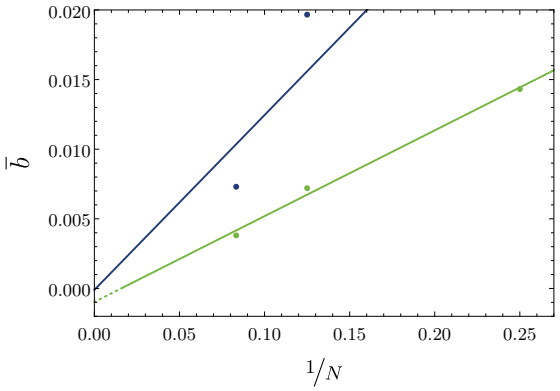

Figure 5.9: Mean variance $\bar{b}$ in dependence on the inverse lattice size $1/N$. The data points for the three lattice sizes are marked by dots, the lines denote fits extrapolating the results to an infinite lattice. The range around $1/N = 0$ is enlarged, values $\bar{b} < 0$ are dotted. Blue (green) colors denote the results of the 3-basis (3^+-basis).

The results of the aforementioned calculations are twofold. Neither the 3^+-basis nor the 3-basis show evidence for vanishing oscillatory contributions in finite lattices. Instead a constant amount of fluctuations around the individual mean values can be observed for long times. What is more, the amount of oscillations is directly related to the lattice size being a strong evidence that fluctuations are a finite size phenomenon. This leads to the expectation that oscillations of $n_{0\uparrow}(t)$ around the individual long-term average vanish altogether for $N \to \infty$.

5.5 Results for imposed hopping restriction

Due to the fact that the 3^+-basis is a superset of the 3-basis it does not come as a surprise that the 3^+-basis is superior to the 3-basis. More reliable results are paid for by a drastically enlarged number of basis operators as shown in figure 5.10. Reducing the number of basis operators becomes crucial for numerical calculations in order to reduce the computational effort needed for results.

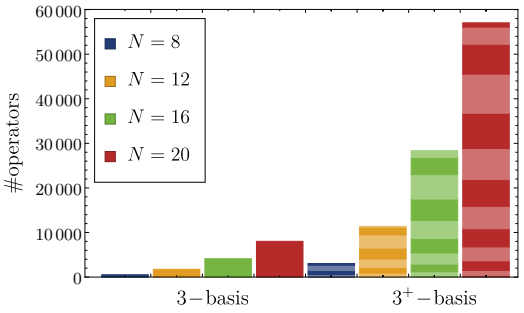

Figure 5.10: Comparison of the number of operators included in each basis for a lattice of N sites. Stacked segments denote operators arising from a further hop in the 3^+-basis. L increases from bottom to top. Alternating colors start with the darker color at the bottom.

One way to achieve a smaller basis size is to reduce the number of allowed hops as discussed in section 5.2.2. A depiction showing the implications of a hopping restriction for a lattice of $N = 12$ sites is shown for two quenches of different strengths in figure 5.11 and renders it possible to recognize a general effect. The agreement between a result derived for at most $L < 8$ hops and the calculation using the full set of operators, i.e. $L = 8$, becomes better for increasing L. Furthermore, a time t_L exists up to which the results of a hopping restriction with L maximally allowed hops are equal to the result of no imposed hopping restriction. Another feature to be observed is the increase of oscillations for stronger interaction.

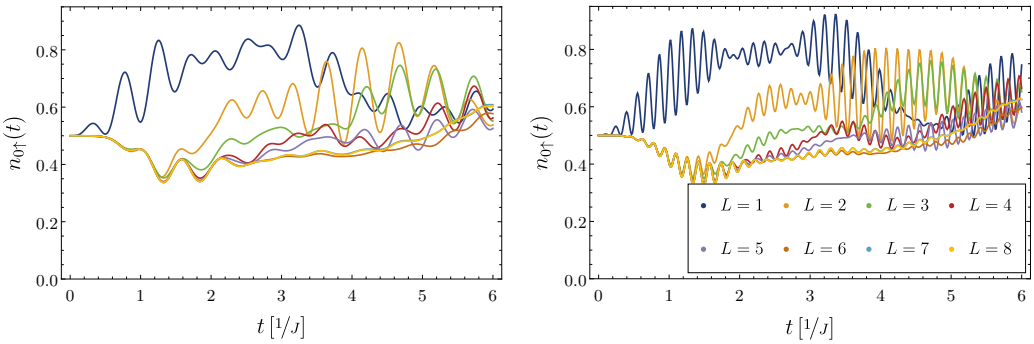

(a) $U = 12\,[J]$ **(b)** $U = 40\,[J]$

Figure 5.11: Dependence of the local particle number average $n_{0\uparrow}(t)$ on the number of maximally allowed hops L for a lattice of $N = 12$ sites. The case $L = 8$ equals the full set of basis operators meaning no hopping restriction is used. The times up to which results agree with the reference result $L = 8$ increases with L.

Analysis of t_L

The deviation time t_L is not influenced by the interaction strength U as depicted in figure 5.12. For this reason the mean value of t_L for all strengths U is used in the following.

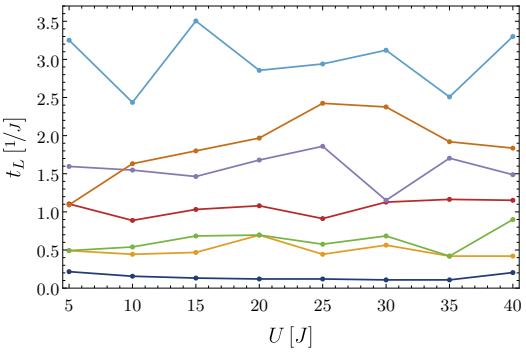

Figure 5.12: Dependence of the deviation time t_L on the interaction strength U for a lattice of $N = 12$ and $U = 5\,[J]$ to $U = 40\,[J]$ in steps of $5\,[J]$. L increases from bottom to top, i.e. the color coding of figure 5.11 is used.

As each hopping restriction L implies a decrease of the overall basis size the question arises in how far t_L depends on the basis fraction used and if all operators contained in the basis contribute to t_L to about the same extent. For each possible restriction L in a lattice of N sites we calculate the ratio between the size of the restricted basis and the full basis as well as the deviation time t_L for which the results of both bases begin to differ by more than 10^{-2}. Since we expect t_L to be directly related to the lattice size a rescaling of the ordinate is used. The resulting dependence shown in figure 5.13 is nearly linear, e.g. implying that a doubling of the used basis fraction enlarges t_L by a factor of two.

Another slightly more subtle fact can be deduced from figure 5.13. Obviously, a time

$$t_{\mathrm{FS}} = \frac{N}{4}\left[\frac{1}{J}\right] \tag{5.17}$$

exists up to which the results for the full basis without hopping restriction can be considered reliable.

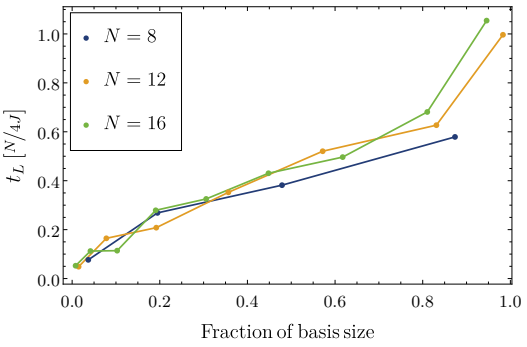

Figure 5.13: Dependence of the mean deviation time t_L on the fraction of the used basis of L maximally allowed hops with respect to the full basis without hopping restriction. The $N = 16$ data set is based on $U = 5$ and $U = 40$.

We ascribe the existence of such time to finite size effects and motivate it using a gedankenexperiment. Consider the periodic boundary conditions shown in figure 5.1 and the tight-binding model, i.e. the Fermi-Hubbard model for $U = 0$, with an additional particle inserted into the lattice at an arbitrary site. The maximum speed information can travel with is given by the group or Fermi velocity

$$v_{\mathrm{F}} = \left.\frac{\mathrm{d}\epsilon_k}{\mathrm{d}k}\right|_{k=k_{\mathrm{F}}} \tag{5.18}$$

which amounts to $v_\mathrm{F} = 2Ja$ for half-filling, the dispersion relation (2.6) for a one-dimensional lattice and a lattice constant a. Consequently, the same information may travel clockwise and counterclockwise and meets at t_FS after having run through half the lattice leading to interference. Results for all times $t > t_\mathrm{FS}$ are strongly influenced by finite size effects while those for $t < t_\mathrm{FS}$ can be considered reliable.

Finally, note a possibility given by the results of figure 5.13. Provided that results of certain observables are only needed for times noticeably below t_FS the computation time can be decreased. The basis may be reduced by a hopping restriction suitable for the intended time range beforehand and results are guaranteed not to differ from calculations using the full basis size for the times in question.[2]

Rabi oscillations

Before the increase of oscillations for strong quenches, cf. figure 5.11, can be understood the limit of infinite on-site interaction has to be examined. For large interaction strengths the Fermi-Hubbard model becomes essentially local and Rabi oscillations occur. The involved system of two states may consist of a single site being occupied by either one or two particles. A general state of a lattice site, e.g. especially the starting state of the quenched system, is a superposition of both with oscillations due to $\mathcal{L}_\mathrm{int}(.)$ in between. Hence, in the $U \to \infty$ limit the system is merely made of N fully independent atoms. In this case only Rabi oscillations occur and the oscillation period is

$$T = \frac{2\pi}{U}\left[\frac{1}{J}\right]. \tag{5.19}$$

The results shown in figure 5.14 confirm the assumption that Rabi oscillations are the reason for the phenomenon to be observed in figure 5.11. For increasing U the periods T fully agree with the prediction given by equation (5.19).

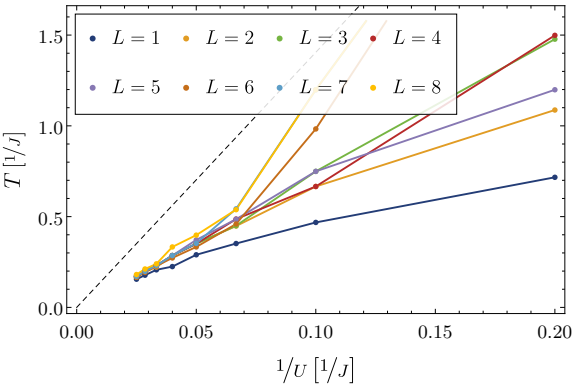

Figure 5.14: Period T of the oscillations of the $N = 12$ lattice with imposed hopping restriction as visible in figure 5.11 and their dependence on the inverse interaction strength $1/U$. The dashed line shows the prediction of Rabi oscillations according to equation (5.19).

[2] To illustrate how useful this approach may be consider the computation of the time dependence of the local particle number average $n_{l\sigma}(t)$ as discussed in section 5.3. Due to the fact that all possible pairings of operators $\langle A_m^\dagger A_n \rangle$ are needed the computation time of $n_{l\sigma}(t)$ is quadratic in the basis size. Halving the basis size using a hopping restriction thus leads to a result being computed four times faster.

Long-term averages

In respect of the promising results for hopping restrictions and the ability to describe the initial dynamics after the quench with a heavily reduced set of operators a natural next step is to study whether reduced operator bases are capable of reproducing the long-term averages as well.

For this we resort to the long-term average of the local particle number operator n_∞ and repeat calculations already performed in section 5.4.2 with the difference of using only the subset of operators arising for at most L allowed hops. The resulting long-term averages and their dependence on U are shown in figure 5.15. Due to translational invariance all fully local operators – especially all one-particle operators $w_1^\dagger(i)$ – are always part of the restricted operator sets despite L. Consequently, the calculations for $U = 0$ are exact which explains the special role of this parameter choice.

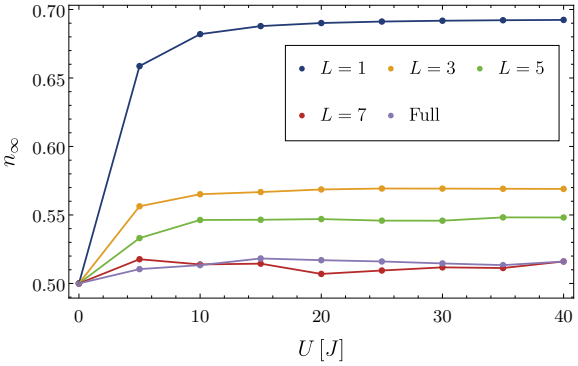

Figure 5.15: Infinite time average of the local particle number operator n_∞ and its dependence on U for $N = 12$. The averages are calculated using the operator subset arising in a hopping restriction L. The full set $L = 8$ is given for reference.

Two aspects can be noticed considering the dependence on L. Apparently, information about the long-term average is not equally distributed among the operators. The mean values $n_\infty^{(L)}$ are calculated for all results $U \neq 0$ of a restricted basis and compared to the reference result n_∞ without hopping restriction yielding

$$\overline{\Delta}_L = \left| 1 - \frac{n_\infty^{(L)}}{n_\infty} \right|. \tag{5.20}$$

Table 5.1: Hopping restriction L, basis fraction δ and relative deviation with respect to the full basis $\overline{\Delta}_L$.

L	$\delta\,[10^{-2}]$	$\overline{\Delta}_L\,[10^{-2}]$
1	1.48	33.19
3	19.20	10.06
5	57.17	5.87
7	98.31	0.43

The relation between this quantity and the ratio of the restricted basis size and the full basis size δ can be found in table 5.1. As an example for the unequally distributed information about the long-term average consider the restricted operator set belonging to $L = 3$. It has about 80 % less operators compared to the full set even though its long-term average only differs by nearly 10 %. Secondly, only the full set of operators is able to generate a reasonable long-term average near to the analytical result of half-filling as used for numerical calculations.

Thus, while a hopping restriction is sufficient and can be used to produce results up to certain time thresholds its usage for long-term averages should be avoided.

6 Observables

In this chapter observables related to the momentum distribution and their evolution after being quenched are studied. Here, both the initial dynamics after the quench and the long-term averages are considered. We start with the jump at the Fermi surface and close the analysis with the quenched momentum distribution.

Due to the fact that the 3^+-basis has proven to be superior to the 3-basis the former one will be used in this chapter. With respect to section 5.4 we expect the 3^+-basis to perform best for strong quenches.

6.1 Time dependence of the jump

The jump $\Delta n(t)$ is calculated using equation (4.27). This means the calculation of all time-dependent prefactors $h_i(t)$ arising in a 3^+-basis is performed as is and the one-particle parts $H_i(t)$ of normal-ordered monomials are separated thereafter. Only these $H_i(t)$ determine the jump at the Fermi surface according to section 4.2.2. The behaviour of the jump describes the dynamics of the system after a quench. Exactly solvable one-dimensional models have been found not to relax [68, 85].

A first approximation of the time dependence of $\Delta n(t)$ in leading order of t can be gained using a 2-loop calculation in real space as motivated in Ref. [62]. The resulting differential equation system can be expanded in t which leads to

$$\Delta n(t) = 1 - U^2 n(1-n)t^2 + \mathcal{O}(t^4). \tag{6.1}$$

The approximation given by (6.1) is a parabola with maximum slope for half-filling and may serve as a means to crosscheck numerical results.

6.1.1 Comparison with reference results for short times

Since the reference data taken from Ref. [62] is computed by resorting to the m-loop approach non-unitary effects render the results useless on intermediate to long time scales. As an example of how missing unitarity on operator level can lead to exponentially increasing solutions consider section 3.5.2 and especially the results on page 32. The local particle number average computed for two to four loops shows a nearly linear increase in the time range in which results can be considered reliable. As the reference results are available for at most 11-loops the following comparison is peformed for fairly short times t. The maximum time range for the

11-loop approach amounts to $t = 2.5\,\left[\frac{1}{J}\right]$ for weak quenches and correspondingly less for large quenches. The jump at the Fermi surface $\Delta n(t)$ is shown in figure 6.1 for weak to intermediate quenches and in figure 6.2 for strong quenches where dashed curves denote results of the 11-loop approach.[1] Exemplarily, the result in leading order of t given in equation (6.1) is inserted into figures 6.1 and 6.2 using a dotted line for $U = 5\,[J]$ and $U = 12\,[J]$, respectively.

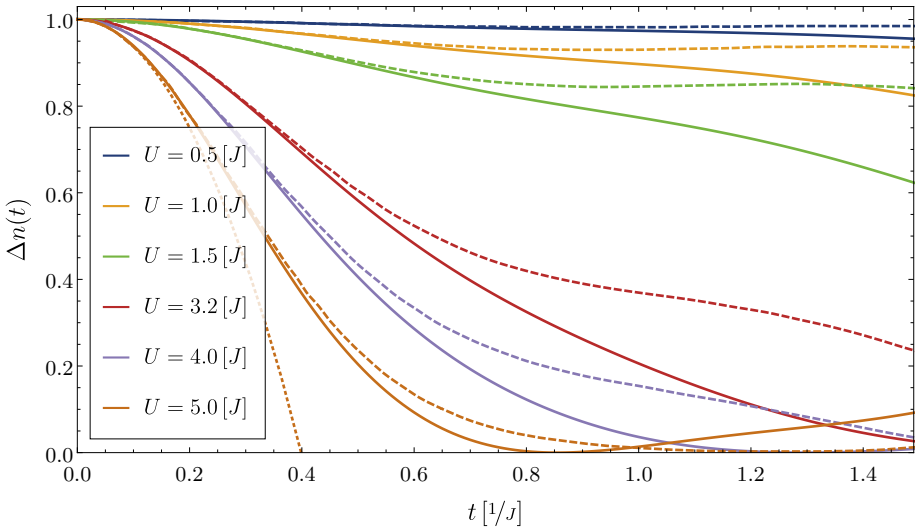

Figure 6.1: Jump at the Fermi surface for weak to intermediate quenches. The solid lines are results derived by the scalar product approach for $N = 36$, half-filling and different U. For comparison the results for equal parameters in a 11-loop approach taken from Ref. [62] are shown in dashed lines. The dotted parabola for $U = 5\,[J]$ is calculated according to (6.1).

For a quench of strength $U = 5\,[J]$ the similarities between the results of the scalar product approach (solid lines) and an 11-loop approach (dashed lines) go far beyond the parabola approximation (6.1). The correspondence in terms of minima becomes better for increasing U. Once the jump has vanished for the first time it slightly increases again. The $U = 5\,[J]$ jump regains about 20 % of its initial value for $t \approx 2\,\left[\frac{1}{J}\right]$ (not shown here). The following maxima are even smaller meaning the oscillation amplitudes decrease notably over time.

The results for strong quenches show a very precise agreement with the 11-loop data regarding oscillation periods and quite a good agreement with respect to

[1] The computational effort needed to calculate scalar product results for $N = 36$ and $N = 40$ amounts to about $3.5 \cdot 10^5$ and $4.8 \cdot 10^5$ basis operators, respectively, as opposed to $5 \cdot 10^5$ operators for the 11-loop approach. While the number of basis operators in the first case increases like $\mathcal{O}(N^3)$, the one for the m-loop approach asymptotically grows like $\mathcal{O}(3^m)$.

amplitudes especially for the $U = 40\,[J]$ quench as the jump highly oscillates while preserving amplitudes of nearly the initial value of the equilibrium momentum distribution at temperature zero. Apparently, this almost complete recovery of amplitudes is phenomenologically different and qualitatively distinct from what could be observed in the weak to intermediate quench regime where amplitudes decrease much faster. We call this behaviour for strong quenches a collapse-and-revival phenomenon. Collapse-and-revival phenomena were observed in similar studies as well [64] where a physical motivation using Rabi oscillations was given, cf. section 5.5 for an in-depth explanation of how Rabi oscillations emerge.

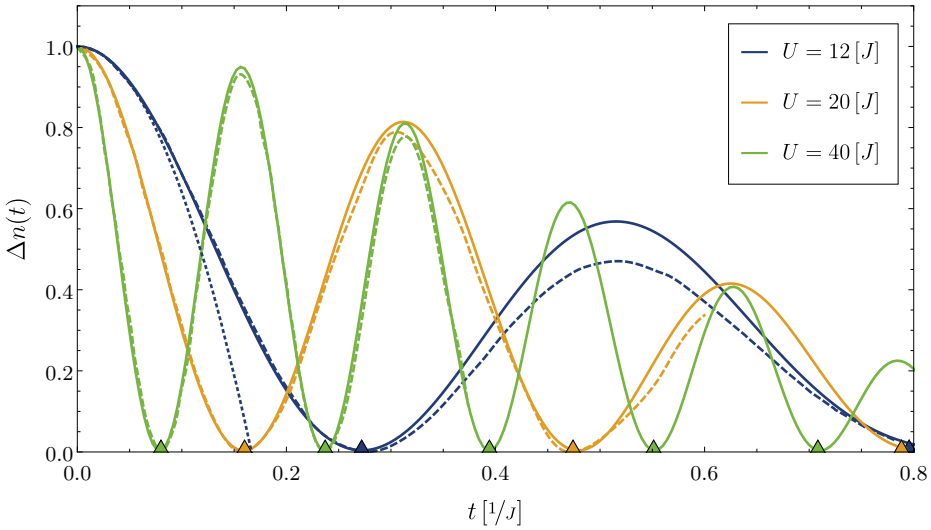

Figure 6.2: Jump at the Fermi surface for strong quenches. The explanations given below figure 6.1 apply, except for $N = 40$ which is used here. Results of the 11-loop approach are only accessible for fairly short times and thus cut off once non-unitary effects spoil the results. Colored triangles at the bottom denote the Rabi oscillation periods according to (5.19) starting at the first zero of each solid curve. For stronger quenches a good agreement regarding both the amplitude and the oscillation period is visible.

Rabi periods predicted using equation (5.19) are inserted into figure 6.2 as colored triangles at the bottom. The predictions start at the first zero of each scalar product result and are then equidistantly positioned with distances T. Especially for the $U = 40\,[J]$ result it can be seen that the physics is mostly governed by these local oscillations as the predictions coincide with the actual minima of the jump.

A general aspect to be noticed is that the scalar product results predict a slower decay of amplitudes for strong quenches than the results obtained using an 11-loop approach. We ascribe this to the lattice and thus the fact that in the 11-loop

approach hopping is considered far more and the surrounding sites may serve as a bath which consistently damps the Rabi oscillations whereas the scalar product result is only exact up to and including processes of two hops as motivated in section 5.2.2. The fact that the 3^+-basis is constructed with completely local processes in mind explains why the oscillation zeros approach the Rabi predictions in the limit of larger interaction strengths.

The qualitatively different behaviour is consistent with a clear distinction between weak and strong quenches and a sharp dynamical transition at

$$U_c = \frac{32}{\pi} \approx 10.2 \tag{6.2}$$

found in previous studies by Eckstein et al. using non-equilibrium DMFT [22], Schiró and Fabrizio using a variational Gutzwiller approach [23, 24] and Hamerla and Uhrig using an m-loop approach [25]. According to these studies two regimes of quenches separated by U_c can be identified. For weak quenches $U < U_c$ the jump decreases fast without significantly regaining its initial amplitude. For strong quenches $U > U_c$ a collapse-and-revival phenomenon is found with a slow decrease in amplitudes.

6.1.2 Finite size effects

While the m-loop approach uses an infinite lattice with a finite number of considered operators due to the exponentially suppressed participations of operators outside the Lieb-Robinson cone, see especially equation (3.22), the scalar product approach uses a finite lattice with periodic boundary conditions. As a result, the influence of finite size effects has to be examined.

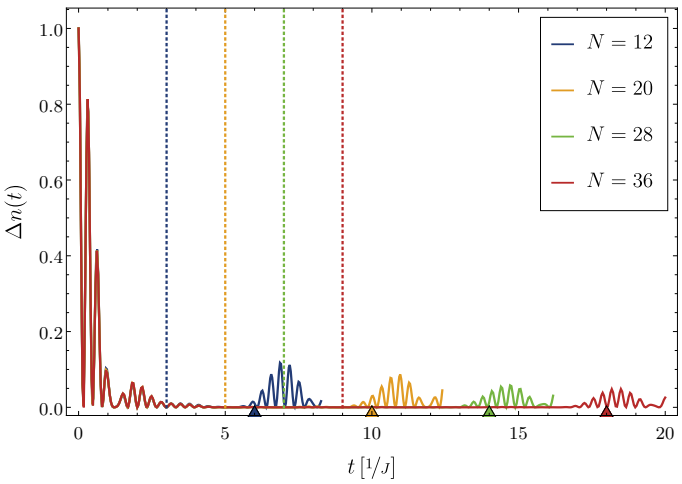

Figure 6.3: Jump at the Fermi surface as derived for different lattice sizes N, half-filling and $U = 20\,[J]$. Dashed lines denote t_{FS}, colored triangles mark $2t_{\mathrm{FS}}$.

Results of the jump $\Delta n(t)$ derived for different lattice sizes and fixed interaction strength are shown in figure 6.3 and display clear evidence for the existence of finite size effects as predicted in section 5.5. Both the times t_{FS} as defined in (5.17), i.e. the time up to which results are expected not to show finite size effects, and $2t_{\mathrm{FS}}$ are inserted as visual orientation. Here, $2t_{\mathrm{FS}}$ equals the time when finite size revivals are predicted to occur.

We emphasize the crucial aspect that the initial behaviour of the jump after the quench is identical regardless of the individual lattice size. This indicates that results are not altered by finite size effects up to the threshold given by t_{FS}.

6.1.3 Dynamical transition

For a further analysis of the dynamical transition between the two distinct parameter ranges separated by U_c identifying the participating energy scales is crucial. In the following we identify two competitive energy scales and the resulting time scales on which oscillations take place. All numerical calculations are performed for $N = 40$ lattice sites.

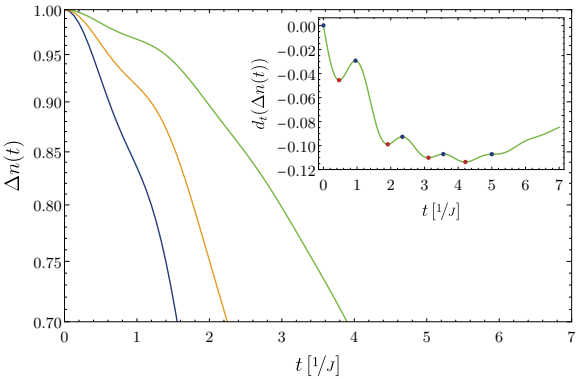

Figure 6.4: Jump at the Fermi surface in semi-logarithmic representation. The compactified interaction strength increases from 0.1 to 0.2 in steps of 0.05 (top to bottom), the inset shows the first derivative of the jump for an interaction of 0.1.

The first time scale can be determined using the energy scale of the bandwidth $W = 4J$ for the one-dimensional lattice as described in section 2.1.2. The finite range of the Brillouin zone implies high-energy cut-offs which consequently neglect physical processes outside the considered ranges. While this is believed to have no effect on low-energy equilibrium physics the situation is different for high-energy processes arising in non-equilibrium systems after quenching [86]. Oscillations due to these cut-offs in momentum space have been observed in different studies [25, 26, 33, 86] and are thus considered a generic feature. Identifying such oscillations due to the finite Brillouin zone with the respective period

$$T = \frac{2\pi}{W} \tag{6.3}$$

is numerically involved. As can be seen in figure 6.4, the wiggling phenomenon [64] is a minor feature superimposed onto the general decrease of the jump and thus closed off to regular techniques like peak detections. Using the first derivative as shown in the inset and measuring the distances between local minima (red dots) a period detection becomes feasible again.

Rabi oscillations govern the second energy and time scale with a corresponding period given in equation (5.19). Especially for $U \gg U_c$ we expect the dynamics to be predominantly determined by the local Rabi processes. Since Rabi oscillations are pronounced effects, cf. for example figure 6.2, a peak detection performed for the original data of the jump is the means of choice to measure periods.

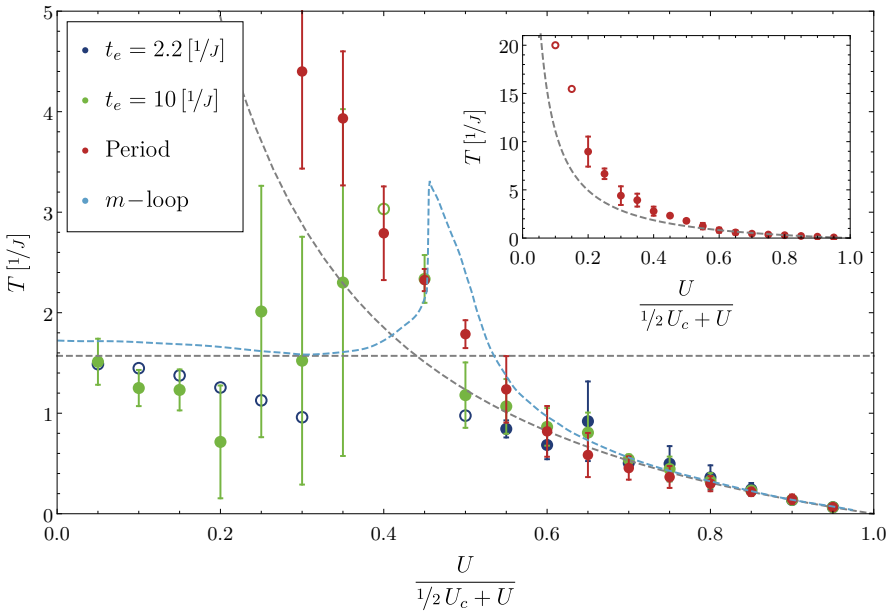

Figure 6.5: Periods of oscillations T in dependence on the compactified interaction parameter as calculated via the first derivative until t_e, via period detect or via fits of m-loop data (as provided in Ref. [25]). Error bars show one standard deviation and are given if data sets contain more than two elements. Otherwise, data points are marked as empty circles. Empty circles in the inset are additionally calculated using data for $t > t_{\mathrm{FS}} = 10$ and thus have to be treated with caution. Dashed lines denote the predicted oscillation periods using the constant period given by equation (6.3) or the Rabi oscillation period (5.19) depending on the interaction.

To account for the two phenomena both peak detection via derivative and regular peak detection is used in parallel in figure 6.5 which shows the dependence of the oscillation period on the compactified interaction strength. The approach via the first derivative considers times $t \in [0, t_e]$. As the scalar product approach can be considered reliable on noticeably longer time scales compared to the most accurate m-loop data currently accessible [25] we are able to extend the regular peak detection to longer times and smaller compactified interactions. As a consequence, it can be noticed that both phenomena coexist for weak quenches whereas the strong quench regime is completely determined by Rabi oscillations due to the increasing number of localized electrons. The inset of figure 6.5 shows the general tendency towards Rabi oscillations in parallel to wiggling even for very weak quenches. We thus especially do not see an abrupt transition between both regimes as in former studies [22–25] but a general crossover instead.

Naturally, the range in between the two regimes of weak and strong quenches is the most difficult one to describe since techniques to differentiate between both effects fail. This explains the increase in uncertainty for mid-range compactified interaction strengths.

6.1.4 Hopping restriction

Given the outcomes of section 5.5 which imply that results may be derived with considerably less numerical effort the jump at the Fermi surface for short times as depicted in figure 6.2 is recomputed using hopping restrictions. In each calculation the number of basis operators is drastically reduced as provided in table 6.1. The respective results are shown in the left-hand side panels of figure 6.6. Using the basic prediction of the deviation time t_L given in section 5.5 the estimated time $t_{L=1}$ for at most one hop is inserted. The actual agreement between $L = 1$ results and the data gathered in a full calculation is far better than expected leading to the conclusion that the influence of hopping is far less for the jump $\Delta n(t)$ in the strong quench regime than it is for the local particle number average. The deviation time seems to behave like $t_L \propto L$ for $\Delta n(t)$.

Table 6.1: Basis sizes for hopping restriction L and $N = 40$ sites

L	Basis size
1	560
5	$2.2 \cdot 10^4$
10	$9.1 \cdot 10^4$
Full	$4.8 \cdot 10^5$

Moreover, the full time range up to t_{FS} is considered in the right-hand side panels. Here, serious shortcomings of the imposed hopping restriction become apparent. For times of about $t > 1\left[\frac{1}{J}\right]$ results derived using a maximum of one hop become unphysical and can not be used anymore. The same applies to $L = 5$ for about $t > 6\left[\frac{1}{J}\right]$ yielding the result that hopping restrictions have constraints in the limit of long times. However, these limitations were to be expected due to an increasing importance of quasi-particle hopping within clusters for $t \to \infty$ and the time-dependency of the Lieb-Robinson cone, cf. section 3.3.1.

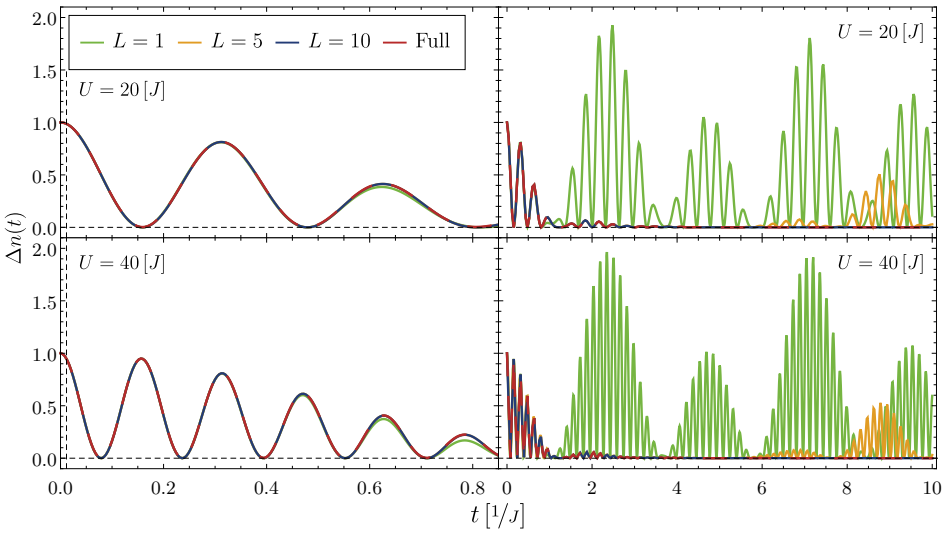

Figure 6.6: Behaviour of the jump at the Fermi surface for short and long times as derived for at most L hops. The respective number of basis operators may be found in table 6.1. Exemplarily, the prediction of section 5.5 up to which $L = 1$ shall be considered reliable is inserted by means of a vertical dashed line in the left-hand side panels at $t_1 = 1.2 \cdot 10^{-2}\left[\frac{1}{J}\right]$.

6.2 Long-term average of the jump

Here, long-term averages of the jump Δn_∞ as given in (4.33) are derived in finite size calculations. Gradually increasing the lattice sizes N and extrapolating the results to the case of the infinite lattice allows us to gain insight into the behaviour of the system in the thermodynamic limit. The results are depicted in figure 6.7.

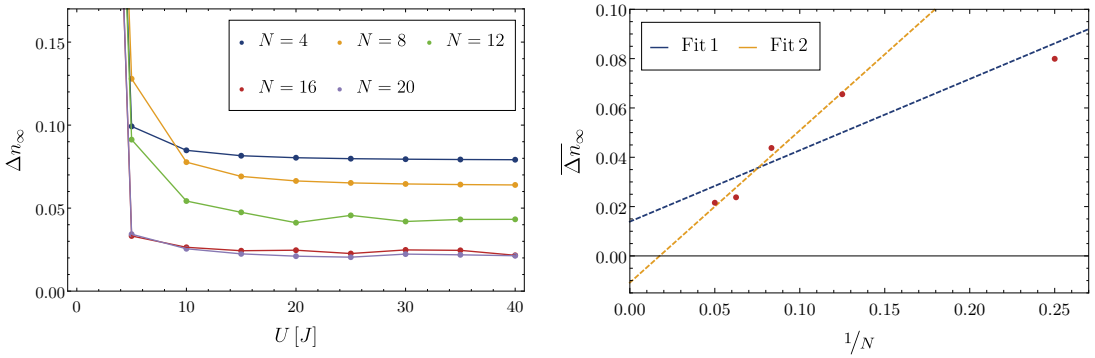

(a) Jump for finite sizes

(b) Extrapolation for $U \geq 15\,[J]$

Figure 6.7: (a) Long-term averages Δn_∞ calculated for a lattice of N sites and varying $U = 0\,[J]$ to $U = 40\,[J]$ in steps of $5\,[J]$. (b) Mean values of the jump for $U = 15\,[J]$ to $U = 40\,[J]$ in dependence on the inverse lattice size. Linear fits for all (Fit 1) and the first four data points (Fit 2) are given as an extrapolation to the infinite lattice.

The first data point in figure 6.7a, i.e. the value of the jump for $U = 0\,[J]$, is one in spite of the lattice size used. This result is in accordance with expectations since without a quench whatsoever the momentum distribution maintains its initial shape shown in figure 2.3 for all times. Once a quench takes place for nonvanishing interaction strengths the long-term averages of the jump decrease notably. For strong quenches the long-term averages Δn_∞ are not influenced by U which motivates an extrapolation to the infinite lattice as depicted in figure 6.7b by means of the linear fit

$$\Delta n_\infty(N) = \frac{a}{N} + b. \tag{6.4}$$

Here, the vertical intercept b denotes the value of the jump for $N \to \infty$. Corresponding fit parameters and their standard deviations are computed as

$$a_1 = (2.8 \pm 0.7) \cdot 10^{-1} \qquad b_1 = (1.4 \pm 1.0) \cdot 10^{-2} \tag{6.5a}$$

$$a_2 = (6.2 \pm 0.7) \cdot 10^{-1} \qquad b_2 = (-1.1 \pm 0.6) \cdot 10^{-2}. \tag{6.5b}$$

Considering both the general tendency of the long-term averages in figure 6.7 to decrease for larger lattices as well as the results of section 6.1.2 which show a strong

reduction of amplitudes and later starting times for finite size effects with increasing N we assume the jump to vanish for infinite lattices. However, the uncertainty with respect to the vertical intercept renders a concluding quantitative statement regarding the disappearence of the jump in the thermodynamic limit impossible.

6.3 Time dependence of the momentum distribution

While previous sections dealt with the jump at the Fermi surface and thus analyzed the behaviour of the momentum distribution near the Fermi wave vector k_F the calculations in the following sections are extended to the full distribution of momenta of finite size systems.

In order to gain access to the behaviour of the momentum distribution after a quantum quench the equation (2.14a) is used as a suitable starting point leading to the average number of particles with momentum k and spin σ for time t of

$$n_{k\sigma}(t) = \frac{1}{N} \sum_l e^{-ikl} g_{l\sigma}(t) \tag{6.6}$$

in the case of the one-dimensional model and a lattice of N sites. To obtain the full momentum distribution equation (6.6) has to be evaluated for all momenta

$$k = \frac{2\pi m}{N} - \pi, \ m \in \{0, \ldots, N-1\}. \tag{6.7}$$

Therefore, the occurring time-dependent correlations $g_{l\sigma}(t)$ as defined in (2.16) have to be obtained which are conceptually identical to the local particle number average (5.12) discussed in section 5.3 according to equation (5.13). The main difference are varying lattice sites for the fermionic creation and the fermionic annihilation operator, respectively.

Due to the fact that it is resorted to the scalar product approach and the basis construction is executed to always account for translational invariance, cf. section 5.2, changes in the considered lattice sites do not alter the operator basis.

Accordingly, expectation values of the form $\langle A_m^\dagger A_n \rangle$ arising due to Wick's theorem do not need to be modified and it is sufficient to merely reinitialize the differential equation system (3.11) and to change the initial condition (3.12) to

$$f_{l\sigma}(t{=}0) = f_{l\sigma} \tag{6.8}$$

for the fermionic annihilation operator. This way the computationally expensive evaluations of expectation values can be saved and replaced by solving (3.11) twice.[2]

[2] Since the annihilation operator follows from the creation operator by a translation and Hermitian conjugation a respective adjustment of the prefactors would also be sufficient. However, the described approach has been found to be better suited from a computational perspective.

In each time step a Fourier transform of all N correlation functions according to (6.6) leads to the full momentum distribution. Results for different interaction strengths are depicted in figures 6.8 and 6.9.

The quench of $U = 4\,[J]$ is found to be in good agreement with data from Ref. [62] using an m-loop approach for times up to which the reference results are converged. For the strong quench regime no data for comparison is available. The results shown are taken for correct up to at least $t_{\mathrm{FS}} = 3\left[\frac{1}{J}\right]$ according to the results of section 5.5. We are thus able to study the momentum distribution for a significantly longer time span than previous similar studies [25, 26].

Both the intermediate quench and the strong quench lead to a redistribution of occupied momenta. While the initial state of the system is characterized by the Fermi sea $|\mathrm{FS}\rangle$ a rapid increase (decrease) of the average occupation number for $k > k_{\mathrm{FS}}$ ($k < k_{\mathrm{FS}}$) with $k_{\mathrm{FS}} = \pi/2$ takes place on short time scales already. After an initial transient burst of formerly unoccupied momenta the two regions of the momentum distribution separated by k_{F} oscillate with a mutual shift of about half the mean oscillation period T. The initial bump for strong quenches is such that immediately after the quench more states above than below k_{F} are occupied until a fast decrease occurs and the shifted oscillation sets in. In contrast, the momentum distribution for an intermediate quench shows no comparable overshooting but a much slighter increase and slowly captures the general oscillatory behaviour.

The shifted oscillations do not die out and persist on longer time scales instead. A repeated increase of oscillation amplitudes visible for strong quenching at the maximum time shown has to be ascribed to finite size effects as discussed in section 6.1.2. The time range around t_{FS} shows a qualitatively similar behaviour of repeated oscillations without any changes in amplitudes and frequency which apparently may hint at a quasi-stationary state overlaid by oscillations. Whether these oscillations die out in the limit $t \to \infty$ of the thermodynamic system leaving back the unmodified quasi-stationary state has yet to be examined.

Over the first Brillouin zone no momentum distribution can be recognized that resembles the initial state $|\mathrm{FS}\rangle$. Especially for the intermediate quenches an almost featureless momentum distribution arises. We emphasize two distinct aspects. First, because of the reciprocal relation between real and momentum space a practically constant momentum distribution implies nearly fully local processes. Second, the superimposed oscillations possess periods near to the Rabi predictions (5.19) for strong quenching. Both aspects underline that highly localized processes take place.

The shift and alternating increase and decrease of particles above and below k_{FS} underline that the dynamics is governed by processes on all energy scales and that processes including large momentum transfers are present. As the excited system heavily differs from the initial state an analytical treatment of the quenched Fermi-Hubbard model can not be based on techniques which suppose the excited state to be nearly identical to the ground state of the non-interacting model.

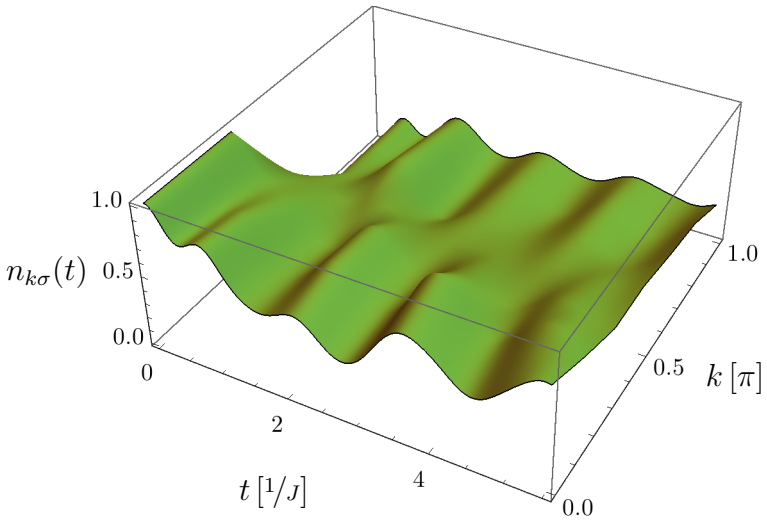

Figure 6.8: Momentum distribution for a lattice of $N = 12$ sites after being quenched to $U = 4\,[J]$ in dependence on time. Only the range of $k \in [0, \pi]$ is shown due to symmetry. Finite size features can be noticed especially for the washed-out transition between occupied and unoccupied states for $t = 0\,\left[\frac{1}{J}\right]$. Starting from the Fermi sea a mutual oscillation in the momentum distribution can be noticed with almost featureless shapes in between.

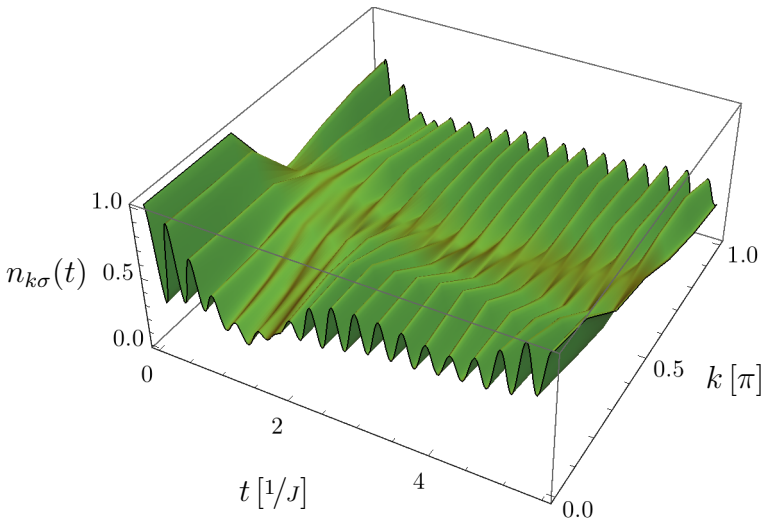

Figure 6.9: Momentum distribution for a lattice of $N = 12$ sites after being quenched to $U = 20\,[J]$ in dependence on time. Remarks below figure 6.8 apply. Compared to results of $U = 4\,[J]$ a huge increase of oscillations happens. For about $t = 1.7\,\left[\frac{1}{J}\right] < t_{\mathrm{FS}}$ a dip in the momentum distribution for excitations of long wavelengths, i.e. $k \approx 0$, is visible.

6.4 Mean momentum distribution

Building upon the results of the former section 6.3 in which a quasi-stationary behaviour on intermediate time scales was recognized we aim at examining the respective state of the system in more detail.

To characterize the system by means of its average momentum distribution two different approaches can be chosen. The first approach consists of generalizing the long-term average of the local particle number operator (4.21) to the long-term average of the time-dependent correlation functions

$$g_{l\sigma}^{\infty} = \sum_{\substack{i,j \\ \lambda_i=\lambda_j}} \overline{\mathbf{v}}_i^{(0)\dagger} \mathbf{A} \overline{\mathbf{v}}_j^{(l)}. \tag{6.9}$$

Note how naturally such generalization follows from the explanations given in section 4.1.1 since neither a new diagonalization of the Liouville matrix nor an adjustment with respect to the expectation value matrix is needed. Instead, a mere change of the initial condition (4.5) is sufficient which is what the new superscripts indicate. By using (6.9) in connection with equation (6.6) the analytical average of the momentum distribution can be obtained for infinite times. However, we do not use this approach here since long-term averages always include finite size contributions which we try to avoid.

In place of this technique we resort to the average over a full oscillation period T, i.e. the mean value of the momentum distribution is taken for $t \in [t_i, t_i + T]$ where the time range is chosen such that neither the initial bump nor finite size effects on longer time scales are included. The oscillation period of the momentum distribution is determined numerically. The resulting mean momentum distributions are shown in figures 6.10 and 6.11.

Both the result for intermediate and the result for strong quenches show a similar behaviour. States belonging to short wave vectors are occupied more than states of longer wave vectors whereas the difference in both ranges is far less than it was for the initial state $|\mathrm{FS}\rangle$. In particular, no pronounced decrease in occupation numbers near k_F is visible anymore in both cases and the momentum distribution takes an almost linear and featureless shape.

Again, the central aspect to be noticed is that electrons which are scattered by the interaction part of the Fermi-Hubbard Hamiltonian (2.4b) must have a large momentum transfer in order to soften the initial distribution belonging to $|\mathrm{FS}\rangle$ to the extent shown in figures 6.10 and 6.11. Correspondingly, the dynamics following a quantum quench will not be describable in terms of processes located near the Fermi surface. As a result, subsequent predictions using the Fermi sea as reference state or vacuum are likely to fail.

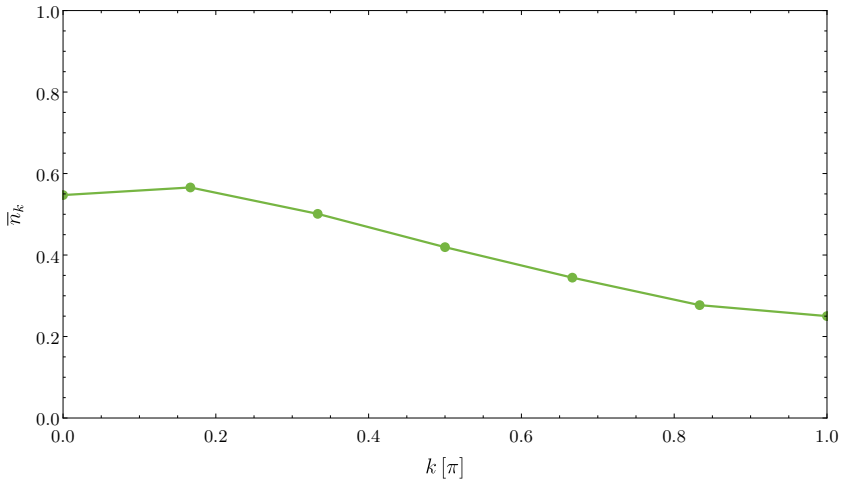

Figure 6.10: Mean momentum distribution for a lattice of $N = 12$ sites and an interaction strength of $U = 4\,[J]$. The corresponding results of figure 6.8 are used and the average value over a full period T is calculated. A general tendency of the mean momentum distribution can be recognized. Still the range of momenta belonging to short wave vectors is occupied to a larger extent than the range of long wave vectors. Nevertheless, the average distribution does not resemble the initial state $|\mathrm{FS}\rangle$. The distribution shows no jump or pronounced features and instead possesses an almost constant shape.

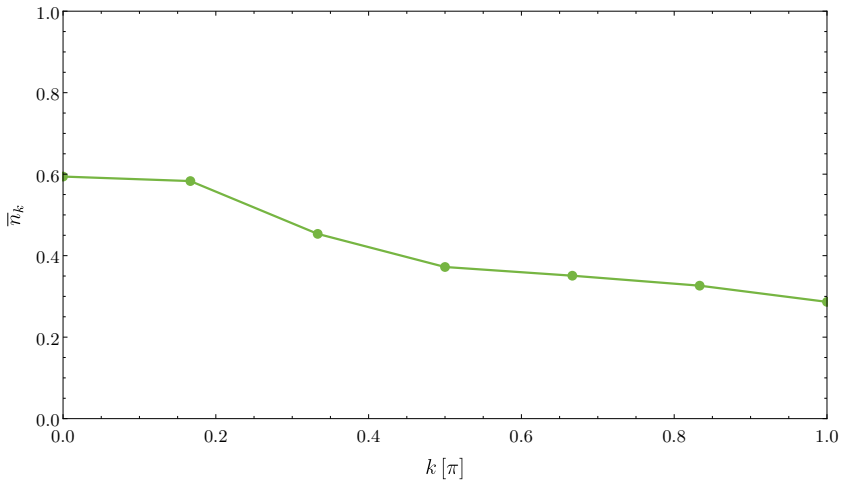

Figure 6.11: Mean momentum distribution as derived for a lattice of $N = 12$ sites and an interaction strength of $U = 20\,[J]$ based on the corresponding results of figure 6.9. The calculation was performed in a similar manner as described below figure 6.10. For the strong quench regime qualitatively identical results arise as for the intermediate quench regime. The mean momentum distribution is featureless and shows a comparably large number of occupied states with high momenta as opposed to the starting state $|\mathrm{FS}\rangle$.

7 Summary and outlook

In the course of this thesis the one-dimensional Fermi-Hubbard model exposed to a sudden global quantum quench was studied using iterated equations of motion. As opposed to previous studies which resorted to repeated applications of the Heisenberg equation of motion to form operator bases in a so called m-loop approach with obstacles in the form of non-unitary effects emerging [25, 26, 62, 64] in this work a scalar product for quantum mechanical operators was introduced which preserves unitarity on operator level. As a result, considerably longer time ranges after the quantum quench could be studied.

Based on results regarding the creation of quasi-particle monomials driving the dynamics due to the hopping part $\mathcal{L}_0(.)$ and the interaction part $\mathcal{L}_{\text{int}}(.)$ of the Fermi-Hubbard Hamiltonian two different sets of basis operators were created and put to use. Operators making up these two bases are mutually orthogonal with respect to the Frobenius scalar product and the respective bases are constructed to be invariant under repeated hopping and interaction, respectively. Especially the latter most extensive operator basis could be shown to yield reliable results in the limit of strong quenches and thus large interaction strengths. Due to the long accessible time range the crossover between weak and strong quenches could be studied in detail showing two competitive physical energy scales which could be ascribed to the finite bandwidth on the one hand and Rabi oscillations due to the interaction on the other hand. The regime of weak quenches was shown to be equally determined by both processes whereas the nearly fully local regime of strong quenches is predominantly influenced by Rabi oscillations.

Restrictions with respect to hopping processes within quasi-particle monomials allowed us to considerably decrease the numerical effort for results up to predicted time thresholds. We were able to reproduce strong quench results from reference computations [62] to high accuracy using only a small fraction of the basis operators. Thus, the computation time compared to previous studies decreased significantly. Moreover, we were able to show that results using hopping restrictions agree with results using the full operator set for much longer times than initially expected. Consequently, restricting hops may serve as a numerically effortless means to analyze the initial dynamics after strong quenches in future studies.

To assess the influences of finite size effects on the results a time t_{FS} was determined and motivated up to which results can be taken for unperturbed by finite size impacts. We stress that this insight allows for a decrease of lattice size and further performance increases if short-time dynamics is of interest.

Using techniques to obtain long-term averages of physical observables the infinite time limit could be examined. In order to make studies of larger lattices with their hugely increasing number of basis operators feasible the computation was altered using the Lanczos algorithm leading to a notable performance increase. The Lanczos algorithm was shown to be a suitable replacement for full diagonalizations due to its focus on the relevant operator subspace.

By means of long-term averages both an extensive quality assessment of the two chosen operator bases and gaining insight into the general relaxation behaviour of the momentum distribution became possible by studying the jump at the Fermi surface. We proved that long-term averages are well suited to exactly describe large systems due to vanishing observable fluctuations in case of the local particle number average and assume the jump at the Fermi surface to fully vanish in the limit of infinite sites and time which agrees with Ref. [68].

Lastly, we considered the full momentum distribution after a quench and recognized oscillatory behaviour separated by the Fermi wave vector of the initial state $|\mathrm{FS}\rangle$. The oscillations persist on longer time scales and can be explained by Rabi oscillations in the strong quench regime. Physical processes of large transferred momenta were identified in context of the quench dynamics. Especially the huge deviation of the momentum distribution after the quench from the Fermi sea renders a description in terms of (dressed) quasi-particles with respect to $|\mathrm{FS}\rangle$ impossible.

Due to partial shortcomings of the operator bases in the weak quench regime further studies should elaborate on the question whether an extension of the 3^+-basis with the aid of more allowed hopping processes is able to improve results in this parameter range. The first step towards this goal is dropping the current restriction of at most three involved sites in a cluster and thus heavily enlarging the cluster spread. Aside from the enlargement of clusters solving the Fermi-Hubbard Hamiltonian by means of Fourier transform in momentum space may yield advantages with respect to the number of operators to be considered. Doing so might especially simplify the calculation of the momentum distribution since no computationally expensive decomposition of expectation values by means of Wick's theorem is needed.

Calculations performed in the thermodynamic limit are of high practical interest. A possible way to obtain results for infinite lattices and to still preserve unitarity on operator level is to combine the translationally invariant infinite size approach discussed in Refs. [25, 26, 62, 64] with the scalar product used in this work.

As the one-dimensional model is fully integrable no true relaxation can be observed. Even the two-dimensional model is not integrable anymore making it the ideal testbed for generic observations without effects caused by, e.g., the dominant momentum conservation of the one-dimensional model [62]. Thus, extending studies using the scalar product approach to further dimensions in which no exact solution exists should be the main intention of consecutive examinations.

A Second quantization

In the course of this thesis a quantum mechanical representation called second quantization is used in order to easily incorporate quantum mechanical axioms into theoretical and numerical calculations. Decisive aspects of this representation will be reproduced here for clarity and are referenced in the preceding chapters where needed. The following description will consider fermions, i.e. particles with half-integer spins, and the corresponding creation and annihilation operators $f_i^\dagger$ and f_i. It is based on the Refs. [50, 87, 88].

A.1 Hilbert and Fock space

A naïve approach to work with interacting Hamiltonians, meaning a Hamiltonian of the form

$$H = H_0 + H_{\text{int}} \tag{A.1}$$

with an effective one-particle problem H_0 and additional interaction H_{int}, consists of resorting to first quantization. Ignoring the interaction part at first the one-particle wave functions $\varphi_{\alpha_i}(\mathbf{r}_j)$ can be deduced from solving the eigenvalue problem of the stationary Schrödinger equation arising from H_0. Here it is assumed that α denotes a set of quantum numbers and $|\alpha_i\rangle$ means a state of the chosen one-particle basis such that $\varphi_{\alpha_i}(\mathbf{r}_j) = \langle \mathbf{r}_j | \alpha_i \rangle$ holds.

Resulting many-particle wave functions for the interaction free system H_0 are Slater determinants

$$\psi_{\alpha_1,\ldots,\alpha_{N_e}}(\mathbf{r}_1,\ldots,\mathbf{r}_{N_e}) = \frac{1}{\sqrt{N_e!}} \begin{vmatrix} \varphi_{\alpha_1}(\mathbf{r}_1) & \ldots & \varphi_{\alpha_{N_e}}(\mathbf{r}_1) \\ \vdots & \vdots & \vdots \\ \varphi_{\alpha_1}(\mathbf{r}_{N_e}) & \ldots & \varphi_{\alpha_{N_e}}(\mathbf{r}_{N_e}) \end{vmatrix} \tag{A.2}$$

constructed from the $\{\varphi_{\alpha_i}(\mathbf{r}_j)\}$. Due to the fact that the complete set of Slater determinants $\{\psi_{\alpha_1,\ldots,\alpha_{N_e}}(\mathbf{r}_1,\ldots,\mathbf{r}_{N_e})\}$ forms a basis of the N_e-particle Hilbert space $\mathcal{H}_{N_e}$ each many-particle state of the full interacting Hamiltonian (A.1) can be written as linear combination of the Slater determinants (A.2). Resulting many-particle wave functions are totally antisymmetric accounting for the indistinguishable N_e fermions.

Unfortunately, this approach becomes tedious and error-prone as it creates indistinguishability at the cost of usability. In second quantization it is refrained from

using Slater determinants as basis and occupation number states are used instead in which particles are indistinguishable by construction. A basis state like

$$|\{n_\alpha\}\rangle := |n_1, n_2, ...\rangle \tag{A.3}$$

represents a system state in which $n_i \in \{0, 1\}$ fermions are in the i-th one-particle state $|\alpha_i\rangle$ whose order is arbitrary but has to be chosen once and kept thereafter.

Creating or annihilating a particle changes the total number of particles in the system. The new system state can not be element of $\mathcal{H}_{N_e}$. To solve the problem of leaving a given space another one of variable total particle number is defined with

$$\mathcal{F} = \mathcal{H}_0 \oplus \mathcal{H}_1 \oplus ... \oplus \mathcal{H}_{N_e} \oplus ... \tag{A.4}$$

as the so called Fock space. The states that are implicitly used in the following consequently fulfill $|\{n_\alpha\}\rangle \in \mathcal{F}$ and make up a complete orthonormal basis of the Fock space.

A.2 Creation and annihilation operators

For simplicity the one-particle states will be consecutively numbered in the following such that one index is sufficient to fully characterize a specific one-particle state, i.e. $\alpha_i \to i$. It is possible to define new operators $f_i^\dagger$ and f_i acting on $\mathcal{F}$. To again account for asymmetry the following definitions can be made

$$f_i^\dagger |n_1, ..., n_i, ...\rangle := (-1)^{\xi_i}(1 - n_i) |n_1, ..., n_i + 1, ...\rangle \tag{A.5a}$$

$$f_i |n_1, ..., n_i, ...\rangle := (-1)^{\xi_i} n_i |n_1, ..., n_i - 1, ...\rangle \tag{A.5b}$$

where $\xi_i = \sum_{k=1}^{i-1} n_k$ counts the total number of occupied states before the i-th one. The particle number operator $\widehat{n}_i := f_i^\dagger f_i$ fulfills the eigenvalue equation

$$\widehat{n}_i |n_1, ..., n_i, ...\rangle = n_i |n_1, ..., n_i, ...\rangle \tag{A.6}$$

and counts all quasi-particles in the state $|i\rangle$.

A.2.1 Canonical anticommutation relations and identities

The fermionic algebra can be described with the aid of the anticommutator

$$\{a, b\} = \{b, a\} = ab + ba \tag{A.7}$$

through the canonical anticommutation relations

$$\left\{f_i^\dagger, f_j\right\} = \delta_{ij} \tag{A.8a}$$

$$\left\{f_i^\dagger, f_j^\dagger\right\} = \left\{f_i, f_j\right\} = 0. \tag{A.8b}$$

It directly follows from equation (A.8b) that the identities

$$\left(f_i^\dagger\right)^2 = f_i^2 = 0 \tag{A.9}$$

hold, thus it is impossible to create or annihilate a particle in the same state twice. This way operators obeying (A.8) automatically implement the Pauli exclusion principle.

A.2.2 Relation between commutation and anticommutation

As the Heisenberg equation of motion (3.6) consists of a commutator

$$[a, b] = -[b, a] = ab - ba \tag{A.10}$$

it is advisable to rewrite occurring more complex commutators by means of anticommutators in order to use (A.8). This is possible with the aid of the correspondence

$$[ab, c] = a\{c, b\} - \{c, a\}b \tag{A.11}$$

leading to helpful building blocks used extensively in analytical calculations such as

$$\left[\widehat{n}_i, f_j^\dagger\right] = \delta_{ij} f_i^\dagger \qquad \left[\widehat{n}_i, f_j\right] = -\delta_{ij} f_i. \tag{A.12}$$

A.3 Operators in first and second quantization

During this thesis one-particle operators O are used as meaningful observables. Every one-particle operator can be written in terms of fermionic creation and annihilation operators using

$$O = \sum_{i,j} O_{ij} f_i^\dagger f_j \tag{A.13a}$$

$$O_{ij} = \int \mathrm{d}^3 r \, \psi_i^*(\mathbf{r}) O(\mathbf{r}) \psi_j(\mathbf{r}) \tag{A.13b}$$

where $O(\mathbf{r})$ describes the contribution of the one-particle operator in first quantization regarding the particle located at position $\mathbf{r}$.

Note that the important total particle number operator $\widehat{N}$ provided in (2.11) directly follows from (A.13a) for the choice $O_{ij} = \delta_{ij}$.

B Frobenius scalar product

Due to the non-unitary time evolution in former studies [25, 26, 62, 64] the long-term behaviour of observables is out of reach. A decisive aspect to overcome this obstacle and to be able to avoid non-unitary effects during the calculations described in chapter 3 is to choose a reasonable scalar product and thus achieve a self-adjoint Liouville superoperator [70]. The scalar product in question and its properties are discussed in this chapter.

B.1 Scalar product definition and criteria

Assume A and B to be linear operators defined on a finite Hilbert space $\mathcal{H}$ with $d = \dim(\mathcal{H}) < \infty$ such that $A, B \in \mathbb{C}^{d\times d}$ are the corresponding matrices representing A and B in $\mathcal{H}$ with respect to a chosen basis. For reasons of simplicity, operators and their respective representations will be used interchangeably below.

Then the Frobenius scalar product $(\cdot|\cdot) : \mathbb{C}^{d\times d} \times \mathbb{C}^{d\times d} \to \mathbb{C}$ given by the relation

$$(A|B) := \mathcal{N}\,\mathrm{Tr}\Big(A^\dagger B\Big) \text{ with normalization } \mathcal{N} := \frac{1}{d} = \frac{1}{\mathrm{Tr}(\mathbb{1})} \tag{B.1}$$

fulfills all mathematical requirements of a scalar product in complex-valued vector spaces as can be directly proven by its properties:

1. **Sesquilinearity** follows from the fact that tracing is a linear transformation and the first operator on the left-hand side of (B.1) becomes its complex conjugate according to the definition.

2. **Hermiticity**

$$(A|B)^* = \mathcal{N}\,\mathrm{Tr}\left([A^\dagger B]^\dagger\right) = \mathcal{N}\,\mathrm{Tr}\left(B^\dagger A\right) = (B|A) \tag{B.2}$$

3. **Positive definiteness**

   Let $\{|j\rangle\}$ be a discrete orthonormal basis in $\mathcal{H}$ and O_{mn} be the matrix element $\langle m|O|n\rangle$ of an operator O. Using the identity $\mathbb{1} = \sum_j |j\rangle\langle j|$ it can be shown that

$$(A|A) = \mathcal{N}\sum_i \langle i|A^\dagger A|i\rangle = \mathcal{N}\sum_{i,j} A^*_{ij}A_{ji} = \mathcal{N}\sum_{i,j} |A_{ji}|^2 \geq 0 \tag{B.3}$$

   holds. As the chosen basis $\{|j\rangle\}$ especially possesses completeness the only possibility for $(A|A) = 0$ are consistently vanishing matrix elements, i.e. $A = 0$.

B.2 Scalar product calculation

The calculation of Frobenius scalar products is a fundamental aspect of all numerical computations used within this thesis which is why the following section is completely dedicated to evaluating scalar products either by hand or with the aid of computational support. The most important cases for scalar product evaluations are the construction of operator bases via Gram-Schmidt processes or the computation of the Liouville matrix.

B.2.1 Introductory examples

In order to motivate the used algorithmic approach to solve the above mentioned task computationally it is illustrated by easily accessible examples. In the course of this key ideas behind the final algorithm are gradually developed.

Calculating a scalar product $(A|B)$ basically means building the adjoint of the left-hand side operator A, multiplying it by the right-hand side operator B and evaluating a sum over expressions proportional to

$$\mathrm{Tr}\left(F_{\alpha_1} \cdot F_{\alpha_2} \cdot \ldots \cdot F_{\alpha_n}\right) = \mathrm{Tr}\left(\prod_j^n F_{\alpha_j}\right) \tag{B.4}$$

where $F_{\alpha_j} \in \{f_{\alpha_j}^\dagger, f_{\alpha_j}\}$ is defined in analogy to the explanation below equation (3.20) as all operators A, B are compound expressions of fermionic creation or annihilation operators.

As a suitable starting point consider the question of the overlap of two given operators $f_{0\uparrow}^\dagger$ and $f_{0\uparrow}^\dagger f_{0\downarrow}^\dagger f_{0\downarrow}$ with respect to (B.1) as it could appear during a Gram-Schmidt process. This way, it is searched for the portion of the first operator projected onto the subspace spanned by the second one. The following exemplary calculation is taken from the construction of an orthonormal basis (3.37), namely the 3-basis in the context of a 2-loop approach (cf. chapters 3 and 5 for naming conventions). The overlap reads

$$\left(f_{0\uparrow}^\dagger \middle| f_{0\uparrow}^\dagger f_{0\downarrow}^\dagger f_{0\downarrow}\right) = \mathcal{N}\,\mathrm{Tr}\left(f_{0\uparrow} f_{0\uparrow}^\dagger f_{0\downarrow}^\dagger f_{0\downarrow}\right) \tag{B.5a}$$

$$\overset{(1)}{=} \mathcal{N}\,\mathrm{Tr}_0\left(f_{0\uparrow} f_{0\uparrow}^\dagger f_{0\downarrow}^\dagger f_{0\downarrow}\right) \cdot \mathrm{Tr}_{1\ldots N-1}\left(\mathbb{1}\right) \tag{B.5b}$$

$$= \frac{1}{4}\,\mathrm{Tr}_0\left(f_{0\uparrow} f_{0\uparrow}^\dagger f_{0\downarrow}^\dagger f_{0\downarrow}\right) \tag{B.5c}$$

$$\overset{(2)}{=} \frac{1}{4}\underbrace{\langle 01|01\rangle}_{=1} = \frac{1}{4}. \tag{B.5d}$$

Note that in step (1) it was made use of a general concept: If A_1 and A_2 are bounded operators acting on separable Hilbert spaces $\mathcal{H}_1$ and $\mathcal{H}_2$ a trace in $\mathcal{H} = \mathcal{H}_1 \otimes \mathcal{H}_2$ can be split according to

$$\mathrm{Tr}\left(A_1 A_2\right) = \mathrm{Tr}_1\left(A_1\right)\mathrm{Tr}_2\left(A_2\right) \tag{B.6}$$

where $\mathrm{Tr}_m(.)$ denotes a trace over $\mathcal{H}_m$. Hence, in a N-site Hilbert space a trace of a product of operators acting on different sites can always be factorized into a product of completely local traces with a four-dimensional local Hilbert space $\{|00\rangle, |10\rangle, |01\rangle, |11\rangle\}$ given the fact that a general state $|\uparrow\downarrow\rangle$ can stand for a site being occupied by no electron, one electron with arbitrary spin direction and two electrons with opposite spins each, respectively. This basis states are pairwise orthonormal as was exploited in step (2).

In practical applications many structurally identical scalar products have to be evaluated in which only the relevant sites vary. Accordingly, the question of a generalization of the exemplary problem (B.5) rises. Calculating the most general form of the scalar product (B.5) for completely arbitrary sites involves

$$\left(f_{i\uparrow}^\dagger \middle| f_{m\uparrow}^\dagger f_{n\downarrow}^\dagger f_{o\downarrow}\right) = \mathcal{N}\,\mathrm{Tr}\left(\overbrace{f_{i\uparrow} f_{m\uparrow}^\dagger} \overbrace{f_{n\downarrow}^\dagger f_{o\downarrow}}\right) \tag{B.7}$$

which can only have a nonvanishing result for the annotated pairings, i.e. $m = i$ and $n = o$. To make use of (B.6) at least two different sites have to be realized, implying $m \neq n$ has to hold, leading to

$$\left(f_{i\uparrow}^\dagger \middle| f_{m\uparrow}^\dagger f_{n\downarrow}^\dagger f_{o\downarrow}\right) = \left(\frac{1}{4}\right)^2 \underbrace{\mathrm{Tr}_m\left(f_{m\uparrow} f_{m\uparrow}^\dagger\right)}_{=2} \cdot \underbrace{\mathrm{Tr}_n\left(f_{n\downarrow}^\dagger f_{n\downarrow}\right)}_{=2} \delta_{mi}\delta_{no} \quad \text{if } m \neq n \tag{B.8a}$$

$$= \frac{1}{4}\delta_{mi}\delta_{no}. \tag{B.8b}$$

Otherwise all creation and annihilation operators act on only one lattice site which results in

$$\left(f_{i\uparrow}^\dagger \middle| f_{m\uparrow}^\dagger f_{n\downarrow}^\dagger f_{o\downarrow}\right) = \frac{1}{4} \underbrace{\mathrm{Tr}_m\left(f_{m\uparrow} f_{m\uparrow}^\dagger f_{m\downarrow}^\dagger f_{m\downarrow}\right)}_{=1} \delta_{mi}\delta_{no}\delta_{mn} \qquad \text{if } m = n \tag{B.9a}$$

$$= \frac{1}{4}\delta_{mi}\delta_{no}\delta_{mn}. \tag{B.9b}$$

Comparing equation (B.8) with (B.9) it can be seen that the value for this concrete scalar product does not depend on the number of realized sites as long as the initial conditions $m = i$ and $n = o$ are met. Therefore, the final result reads

$$\left(f_{i\uparrow}^\dagger \middle| f_{m\uparrow}^\dagger f_{n\downarrow}^\dagger f_{o\downarrow}\right) = \frac{1}{4}\delta_{mi}\delta_{no}. \tag{B.10}$$

B.2.2 Algorithmic approach

A pseudo-code algorithm incorporating ideas from section B.2.1 can be formulated to calculate a Frobenius scalar product (B.4). An explanation for algorithm 1 by means of an example is given below the pseudo-code. Algorithms 2 and 3 are responsible for calculating traces. Algorithm 1 is fully generic, uses abstract indices and examines all cases in which nonvanishing scalar products can occur. Return values are rules for pairing the indices and the respective scalar product values.

Algorithm 1 Generation and testing of all possible pairings

1: **function** ScalarProduct($L = \{F_{\alpha_1}, ..., F_{\alpha_n}\}$)
2: $C_{\uparrow/\downarrow}$ or $A_{\uparrow/\downarrow} \leftarrow$ list of all indices appearing in $f^{\dagger}_{\uparrow/\downarrow}$ or $f_{\uparrow/\downarrow}$operators within L
3: $S \leftarrow \emptyset$
4: **for each** $u \in$ Permutations($C_{\uparrow}$) **do**
5: **for each** $d \in$ Permutations($C_{\downarrow}$) **do**
6: $r \leftarrow$ Rule where each $u[i] = A_{\uparrow}[i]$ and each $d[i] = A_{\downarrow}[i]$
7: $G \leftarrow$ Undirected graph whose vertices are all indices within r
8: **for each** condition $a{=}b \in r$ **do**
9: $G \leftarrow G \cup (a, b)$ ▷ Add edge connecting two indices
10: $r' \leftarrow$ ConnectedComponents(G) ▷ Subgraphs have equal indices
11: **for each** way w to connect subgraphs in r' **do**
12: $v \leftarrow$ Trace($L|_w$) ▷ Trace result considering index equalities w
13: **if** $v \neq 0$ **then** $S \leftarrow S \cup \{(v, w)\}$
14: **return** S

Example: Consider again the scalar product (B.7) in its general form (B.4) as input L for which the algorithm 1 will be executed line by line. Initializing the index sets in line 2 leads to

$$C_{\uparrow}{=}\{m\},\, C_{\downarrow}{=}\{n\},\, A_{\uparrow}{=}\{i\} \text{ and } A_{\downarrow}{=}\{o\}\,. \tag{B.11}$$

As only one element is in each list $C_{\uparrow/\downarrow}$ the lists themselves are all possible permutations. In line 6 the rule set becomes

$$r = \{m{=}i,\, n{=}o\} \tag{B.12}$$

and serves as a basis to connect vertices within G that initially takes the form

in line 7. Utilizing the rule set (B.12) edges can be inserted into G where each edge (v_m, v_n) denotes the equality

$$v_m = v_n. \tag{B.13}$$

The resulting partly connected graph G looks like

by the end of line 9. Now G gives an immediate overview about what indices have to be considered equal when calculating scalar products. Every index vertex v_i that is part of the same subgraph as a vertex v_j has the same value as v_j. In other words, if two vertices are connected to each other by paths[1] they are considered equal henceforth.

In line 11 there are two ways to connect subgraphs: The first one, i.e. w_1, is to leave everything as is and to not introduce further edges. The resulting graph for w_1 has the form

and thus results in the index equality to be used for scalar product calculation

$$w_1 \colon \; m = i \text{ and } n = o. \tag{B.14}$$

The second possibility is to connect the two connected components of G by means of an edge, e.g. (i, n). The resulting graph for w_2 assumes the form

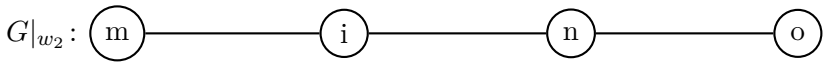

with the corresponding index equality

$$w_2 \colon \; m = i = n = o. \tag{B.15}$$

In line 12 both index equalities (B.14) and (B.15) are explicitly evaluated. In order to do so the algorithm 2 is used. Exemplarily for w_1, algorithm 2 is carried out here. The input expression thus has the form

$$L|_{w_1} = f_{m\uparrow} f^{\dagger}_{m\uparrow} f^{\dagger}_{n\downarrow} f_{n\downarrow} \tag{B.16}$$

for which the operators are initially separated by sites in line 2 of algorithm 2. For this purpose algorithm 3 is used which iterates through the given indices in order of appearance, collects all subsequent operators of the same site and moves them to

[1] The underlying subgraph decomposition can be achieved in many different ways. A common one for undirected graphs is to use depth-first search [83] and to look for disjoint sets of the intervals $[v.d, v.f]$ where $v.d$ means the discovery time of vertex v and $v.f$ the time the vertex was finished.

the position one index after the current one. Whilst doing so the number of operator swaps is counted in order to account for (A.8). Note that algorithm 3 ensures to never make operators of the same quantum numbers change position. This way no additional terms are created, i.e. $i \neq j$ holds in (A.8). In the present case the operators are already grouped such that (B.16) is not changed by GROUP.

The real calculation of the trace in line 5 of algorithm 2 now involves separately applying all operators of one site to a basis copy ψ each, comparing the finished working copy ψ to B, checking what states remained the same and to multiply the corresponding results of all individual sites. Starting with the m operators the application

$$f_{m\uparrow} f_{m\uparrow}^\dagger |00\rangle = f_{m\uparrow} |10\rangle = |00\rangle \tag{B.17a}$$

$$f_{m\uparrow} f_{m\uparrow}^\dagger |10\rangle = 0 \tag{B.17b}$$

$$f_{m\uparrow} f_{m\uparrow}^\dagger |01\rangle = f_{m\uparrow} |11\rangle = |01\rangle \tag{B.17c}$$

$$f_{m\uparrow} f_{m\uparrow}^\dagger |11\rangle = 0 \tag{B.17d}$$

shows that two operators of ψ are equal to operators of B with the same indices, i.e. the first one $\psi[1]$ and the third one $\psi[3]$. For this reason $r = 1/2$ holds in line 10 of algorithm 2. A similar application has to be done for all n operators leading to

$$f_{n\downarrow}^\dagger f_{n\downarrow} |00\rangle = 0 \tag{B.18a}$$

$$f_{n\downarrow}^\dagger f_{n\downarrow} |10\rangle = 0 \tag{B.18b}$$

$$f_{n\downarrow}^\dagger f_{n\downarrow} |01\rangle = f_{n\downarrow}^\dagger |00\rangle = |01\rangle \tag{B.18c}$$

$$f_{n\downarrow}^\dagger f_{n\downarrow} |11\rangle = f_{n\downarrow}^\dagger |10\rangle = |11\rangle \tag{B.18d}$$

and again two equal operators of ψ and B, namely $\psi[3]$ and $\psi[4]$. The trace result in line 10 now reads

$$r_n = \frac{1}{2} \cdot r_m = \frac{1}{4} \tag{B.19}$$

as the result in this step r_n has to be multiplied by the result of the last step r_m. As no odd number of swaps was needed during GROUP the result $r = r_n$ is returned in line 13 of algorithm 2.

Case w_2 delivers precisely the same results as w_1 with the mere difference of only one realized site in TRACE. Consequently, the results of algorithmically calculating the traces finally are

$$\text{TRACE}(L|_{w_1}) = \frac{1}{4} \tag{B.20a}$$

$$\text{TRACE}(L|_{w_2}) = \frac{1}{4} \tag{B.20b}$$

which directly correspond to the results already obtained by hand in (B.9) and (B.8). Due to the fact that both scalar product results do not vanish they are added to S and returned thereafter in line 14 of algorithm 1.

As can be seen algorithm 1 is designed such that only physically sensible pairings of operators are analyzed. Neither two annihilation nor two creation operators are paired leading to a drastic decrease in computation time. The output of ScalarProduct comprises needed index equalities and corresponding results rendering it possible to directly incorporate the analytical output into numerical calculations.

Algorithm 2 Trace calculation

```
1:  function Trace(L = {F_{α_1}, ..., F_{α_n}})
2:      (p, L) ←Group(L)
3:      B ← {|00⟩, |10⟩, |01⟩, |11⟩}          ▷ Local four-dimensional |↑↓⟩-basis
4:      ψ ← B, r ← 1, s ← Site(α_n)    ▷ Initialization: States, result, current site
5:      for i ← n downto 0 do
6:          if i = 0 or Site(α_i) ≠ s then                          ▷ Finish old site
7:              t ← 0
8:              for j ← 1 to 4 do                    ▷ Count states that survived
9:                  if ψ[j] = B[j] then t ← t + 1
10:             r ← t/4 · r
11:             ψ ← B,  s ← Site(α_i)                                ▷ Reinitialization
12:         if i > 0 then apply L[i] with respect to spin to each state in ψ
13:     return r · p
```

Algorithm 3 Operator grouping in real space

```
1:  function Group(L = {F_{α_1}, ..., F_{α_n}})
2:      i ← 1
3:      p ← 1                          ▷ Prefactor reflecting the number of swaps
4:      while i ≤ n do
5:          for j ← i + 1 to n do
6:              if Site(α_j) = Site(α_i) then          ▷ Group operators of same site
7:                  move L[j] to position i + 1
8:                  if (j − (i + 1) mod 2) ≠ 0 then
9:                      p ← −p                  ▷ An odd number of swaps took place
10:                 i ← i + 1
11:         i ← i + 1
12:     return (p, L)
```

B.3 Used scalar products

The following scalar products can be derived by means of techniques explained in B.2. In order to shorten the expressions the same notation for basis operators is used as in section 5.2. Notice that all constraints regarding possible and impossible index combinations remain which is why index equalities that are impossible by basis construction are *not* considered hereafter.[2] Due to equation (3.41) the relation

$$(A_i|\mathcal{L}(A_j)) = (A_j|\mathcal{L}(A_i)) \tag{B.21}$$

holds and only one half of all possible scalar products has to be given explicitly below.

$w_1^\dagger(k)$

$$\Big(w_1^\dagger(k)\,\Big|\,\mathcal{L}\Big(w_1^\dagger(c)\Big)\Big) = -J\delta_{k,c\pm1} + \frac{U}{2}\delta_{kc} \tag{B.22a}$$

$$\Big(w_1^\dagger(k)\,\Big|\,\mathcal{L}\Big(w_2^\dagger(c,d,e)\Big)\Big) = \frac{U}{2}\delta_{kc}\delta_{kd}\delta_{ke} \tag{B.22b}$$

$$\Big(w_1^\dagger(k)\,\Big|\,\mathcal{L}\Big(w_{3\ldots9}^\dagger(c,d,e)\Big)\Big) = 0 \tag{B.22c}$$

$w_2^\dagger(k,l,m)$

$$\begin{aligned}\Big(w_2^\dagger(k,l,m)\,\Big|\,\mathcal{L}\Big(w_2^\dagger(c,d,e)\Big)\Big) = &-J\delta_{k,c\pm1}\delta_{ld}\delta_{me} - J\delta_{kc}\delta_{l,d\pm1}\delta_{me} \\ &+ J\delta_{kc}\delta_{ld}\delta_{m,e\pm1} + \frac{U}{2}\delta_{kc}\delta_{ld}\delta_{me}\end{aligned} \tag{B.23a}$$

$$\Big(w_2^\dagger(k,l,m)\,\Big|\,\mathcal{L}\Big(w_3^\dagger(c,d,e)\Big)\Big) = \frac{U}{2}\delta_{kc}\delta_{ld}\delta_{me} \tag{B.23b}$$

$$\Big(w_2^\dagger(k,l,m)\,\Big|\,\mathcal{L}\Big(w_4^\dagger(c,d,e)\Big)\Big) = \frac{U}{2}\delta_{kc}\delta_{ld}\delta_{me} \tag{B.23c}$$

$$\Big(w_2^\dagger(k,l,m)\,\Big|\,\mathcal{L}\Big(w_5^\dagger(c,d,e)\Big)\Big) = \frac{U}{2}\delta_{kc}\delta_{ld}\delta_{me} \tag{B.23d}$$

$$\Big(w_2^\dagger(k,l,m)\,\Big|\,\mathcal{L}\Big(w_{6\ldots9}^\dagger(c,d,e)\Big)\Big) = 0 \tag{B.23e}$$

[2] Understanding this aspect is crucial in correctly working with the scalar products (B.22) to (B.30). To see what difference is made if index equalities are excluded beforehand consider the scalar product

$$(w_3^\dagger(k,l,m)\,|\,\mathcal{L}(w_4^\dagger(c,d,e))) = -\frac{U}{2}\delta_{km}\delta_{kc}\delta_{ke}\delta_{ld} - \frac{U}{2}\delta_{kl}\delta_{kc}\delta_{kd}\delta_{me} + \ldots\,.$$

Thus, the general form of the scalar product has a nonvanishing value but due to the requirements $k \neq l, k \neq m, d \neq c$ and $d \neq e$ of the 3^+-basis operators involved the scalar product with respect to all constraints becomes zero, cf. (B.24b).

$w_3^\dagger(k,l,m)$

$$\left(w_3^\dagger(k,l,m)\,\middle|\,\mathcal{L}\left(w_3^\dagger(c,d,e)\right)\right) = -J\delta_{k,c\pm1}\delta_{kd}\delta_{ke}\delta_{cl}\delta_{cm} - J\delta_{kc}\delta_{l,d\pm1}\delta_{me} + J\delta_{kc}\delta_{ld}\delta_{m,e\pm1} + \frac{U}{2}\delta_{kc}\delta_{ld}\delta_{me} \tag{B.24a}$$

$$\left(w_3^\dagger(k,l,m)\,\middle|\,\mathcal{L}\left(w_4^\dagger(c,d,e)\right)\right) = 0 \tag{B.24b}$$

$$\left(w_3^\dagger(k,l,m)\,\middle|\,\mathcal{L}\left(w_5^\dagger(c,d,e)\right)\right) = 0 \tag{B.24c}$$

$$\left(w_3^\dagger(k,l,m)\,\middle|\,\mathcal{L}\left(w_6^\dagger(c,d,e)\right)\right) = \frac{U}{2}\delta_{kc}\delta_{ld}\delta_{me} \tag{B.24d}$$

$$\left(w_3^\dagger(k,l,m)\,\middle|\,\mathcal{L}\left(w_7^\dagger(c,d,e)\right)\right) = -\frac{U}{2}\delta_{kc}\delta_{ld}\delta_{me} \tag{B.24e}$$

$$\left(w_3^\dagger(k,l,m)\,\middle|\,\mathcal{L}\left(w_8^\dagger(c,d,e)\right)\right) = 0 \tag{B.24f}$$

$$\left(w_3^\dagger(k,l,m)\,\middle|\,\mathcal{L}\left(w_9^\dagger(c,d,e)\right)\right) = 0 \tag{B.24g}$$

$w_4^\dagger(k,l,m)$

$$\left(w_4^\dagger(k,l,m)\,\middle|\,\mathcal{L}\left(w_4^\dagger(c,d,e)\right)\right) = -J\delta_{k,c\pm1}\delta_{ld}\delta_{me} + J\delta_{kc}\delta_{ld}\delta_{m,e\pm1} + \frac{U}{2}\delta_{kc}\delta_{ld}\delta_{me} \tag{B.25a}$$

$$\left(w_4^\dagger(k,l,m)\,\middle|\,\mathcal{L}\left(w_5^\dagger(c,d,e)\right)\right) = -J\delta_{k,c\pm1}\delta_{ke}\delta_{km}\delta_{cd}\delta_{cl} \tag{B.25b}$$

$$\left(w_4^\dagger(k,l,m)\,\middle|\,\mathcal{L}\left(w_6^\dagger(c,d,e)\right)\right) = \frac{U}{2}\delta_{kc}\delta_{ld}\delta_{me} \tag{B.25c}$$

$$\left(w_4^\dagger(k,l,m)\,\middle|\,\mathcal{L}\left(w_7^\dagger(c,d,e)\right)\right) = 0 \tag{B.25d}$$

$$\left(w_4^\dagger(k,l,m)\,\middle|\,\mathcal{L}\left(w_8^\dagger(c,d,e)\right)\right) = -\frac{U}{2}\delta_{kc}\delta_{ld}\delta_{me} \tag{B.25e}$$

$$\left(w_4^\dagger(k,l,m)\,\middle|\,\mathcal{L}\left(w_9^\dagger(c,d,e)\right)\right) = 0 \tag{B.25f}$$

$w_5^\dagger(k,l,m)$

$$\left(w_5^\dagger(k,l,m)\,\middle|\,\mathcal{L}\left(w_5^\dagger(c,d,e)\right)\right) = -J\delta_{k,c\pm1}\delta_{ld}\delta_{me} - J\delta_{kc}\delta_{l,d\pm1}\delta_{me} + \frac{U}{2}\delta_{kc}\delta_{ld}\delta_{me} \tag{B.26a}$$

$$\left(w_5^\dagger(k,l,m)\,\middle|\,\mathcal{L}\left(w_6^\dagger(c,d,e)\right)\right) = 0 \tag{B.26b}$$

$$\left(w_5^\dagger(k,l,m)\,\middle|\,\mathcal{L}\left(w_7^\dagger(c,d,e)\right)\right) = \frac{U}{2}\delta_{kc}\delta_{ld}\delta_{me} \tag{B.26c}$$

$$\left(w_5^\dagger(k,l,m)\,\middle|\,\mathcal{L}\left(w_8^\dagger(c,d,e)\right)\right) = \frac{U}{2}\delta_{kc}\delta_{ld}\delta_{me} \tag{B.26d}$$

$$\left(w_5^\dagger(k,l,m)\,\middle|\,\mathcal{L}\left(w_9^\dagger(c,d,e)\right)\right) = 0 \tag{B.26e}$$

$w_6^\dagger(k,l,m)$

$$\left(w_6^\dagger(k,l,m)\,\middle|\,\mathcal{L}\left(w_6^\dagger(c,d,e)\right)\right) = J\delta_{kc}\delta_{ld}\delta_{m,e\pm1} + \frac{U}{2}\delta_{kc}\delta_{ld}\delta_{me} \tag{B.27a}$$

$$\left(w_6^\dagger(k,l,m)\,\middle|\,\mathcal{L}\left(w_7^\dagger(c,d,e)\right)\right) = 0 \tag{B.27b}$$

$$\left(w_6^\dagger(k,l,m)\,\middle|\,\mathcal{L}\left(w_8^\dagger(c,d,e)\right)\right) = 0 \tag{B.27c}$$

$$\left(w_6^\dagger(k,l,m)\,\middle|\,\mathcal{L}\left(w_9^\dagger(c,d,e)\right)\right) = -\frac{U}{2}\delta_{kc}\delta_{ld}\delta_{me} \tag{B.27d}$$

$w_7^\dagger(k,l,m)$

$$\left(w_7^\dagger(k,l,m)\,\middle|\,\mathcal{L}\left(w_7^\dagger(c,d,e)\right)\right) = -J\delta_{kc}\delta_{l,d\pm1}\delta_{me} + \frac{U}{2}\delta_{kc}\delta_{ld}\delta_{me} \tag{B.28a}$$

$$\left(w_7^\dagger(k,l,m)\,\middle|\,\mathcal{L}\left(w_8^\dagger(c,d,e)\right)\right) = 0 \tag{B.28b}$$

$$\left(w_7^\dagger(k,l,m)\,\middle|\,\mathcal{L}\left(w_9^\dagger(c,d,e)\right)\right) = \frac{U}{2}\delta_{kc}\delta_{ld}\delta_{me} \tag{B.28c}$$

$w_8^\dagger(k,l,m)$

$$\left(w_8^\dagger(k,l,m)\,\middle|\,\mathcal{L}\left(w_8^\dagger(c,d,e)\right)\right) = -J\delta_{k,c\pm1}\delta_{ld}\delta_{me} + \frac{U}{2}\delta_{kc}\delta_{ld}\delta_{me} \tag{B.29a}$$

$$\left(w_8^\dagger(k,l,m)\,\middle|\,\mathcal{L}\left(w_9^\dagger(c,d,e)\right)\right) = \frac{U}{2}\delta_{kc}\delta_{ld}\delta_{me} \tag{B.29b}$$

$w_9^\dagger(k,l,m)$

$$\left(w_9^\dagger(k,l,m)\,\middle|\,\mathcal{L}\left(w_9^\dagger(c,d,e)\right)\right) = \frac{U}{2}\delta_{kc}\delta_{ld}\delta_{me} \tag{B.30}$$

Bibliography

[1] Brian P. Anderson and Mark A. Kasevich.
"Macroscopic Quantum Interference from Atomic Tunnel Arrays".
In: *Science* 282.5394 (1998).

[2] Immanuel Bloch. "Ultracold quantum gases in optical lattices".
In: *Nat. Phys.* 1.1 (2005).

[3] Stefan Trotzky et al. "Probing the relaxation towards equilibrium in an isolated strongly correlated 1D Bose gas". In: *Nat. Phys.* 8.4 (2011).

[4] Markus Greiner et al. "Quantum phase transition from a superfluid to a Mott insulator in a gas of ultracold atoms". In: *Nature* 415.6867 (2002).

[5] Nathan Goldman, Jan C. Budich, and Peter Zoller.
"Topological quantum matter with ultracold gases in optical lattices".
In: *Nat. Phys.* 12.7 (2016).

[6] Vollrath M. Axt and Tilmann Kuhn. "Femtosecond spectroscopy in semiconductors: a key to coherences, correlations and quantum kinetics".
In: *Reports Prog. Phys.* 67.4 (2004).

[7] Klaus Morawetz. *Nonequilibrium Physics at Short Time Scales.*
Berlin: Springer, 2004.

[8] Luca Perfetti et al. "Time Evolution of the Electronic Structure of 1T-TaS2 through the Insulator-Metal Transition". In: *Phys. Rev. Lett.* 97.6 (2006).

[9] Richard D. Mattuck.
A Guide to Feynman Diagrams in the Many-Body Problem.
New York: Dover Publications, 1976.

[10] Pasquale Calabrese, Fabian H. L. Essler, and Maurizio Fagotti.
"Quantum Quench in the Transverse-Field Ising Chain".
In: *For. Sci.* 42.2 (2011).

[11] Pasquale Calabrese, Fabian H. L. Essler, and Maurizio Fagotti. "Quantum quenches in the transverse field Ising chain II: Stationary state properties".
In: *J. Stat. Mech. Theory Exp.* 2012.07 (2012).

[12] Jean-Sébastien Caux and Fabian H. L. Essler. "Time Evolution of Local Observables After Quenching to an Integrable Model".
In: *Phys. Rev. Lett.* 110.25 (2013).

[13] Michael Moeckel and Stefan Kehrein.
"Interaction Quench in the Hubbard Model".
In: *Phys. Rev. Lett.* 100.17 (2008).

[14] Salvatore R. Manmana et al. "Time evolution of correlations in strongly interacting fermions after a quantum quench".
In: *Phys. Rev. B - Condens. Matter Mater. Phys.* 79.15 (2009).

[15] Peter Barmettler et al. "Relaxation of antiferromagnetic order in spin-1/2 chains following a quantum quench". In: *Phys. Rev. Lett.* 102.13 (2009).

[16] Pasquale Calabrese and John Cardy. "Entanglement and correlation functions following a local quench: a conformal field theory approach".
In: *J. Stat. Mech. Theory Exp.* 2007.10 (2007).

[17] Petar Jurcevic et al. "Quasiparticle engineering and entanglement propagation in a quantum many-body system". In: *Nature* 511.7508 (2014).

[18] Andreas M. Läuchli and Corinna Kollath. "Spreading of correlations and entanglement after a quench in the one-dimensional Bose–Hubbard model".
In: *J. Stat. Mech. Theory Exp.* 2008.05 (2008).

[19] David Chen et al. "Quantum Quench of an Atomic Mott Insulator".
In: *Phys. Rev. Lett.* 106.23 (2011).

[20] Tim Langen et al. "Local emergence of thermal correlations in an isolated quantum many-body system". In: *Nat. Phys.* 9.10 (2013).

[21] Marcos Rigol.
"Quantum quenches and thermalization in one-dimensional fermionic systems".
In: *Phys. Rev. A - At. Mol. Opt. Phys.* 80.5 (2009).

[22] Martin Eckstein, Marcus Kollar, and Philipp Werner.
"Thermalization after an Interaction Quench in the Hubbard Model".
In: *Phys. Rev. Lett.* 103.5 (2009).

[23] Marco Schiró and Michele Fabrizio. "Time-Dependent Mean Field Theory for Quench Dynamics in Correlated Electron Systems".
In: *Phys. Rev. Lett.* 105.7 (2010).

[24] Marco Schiró and Michele Fabrizio.
"Quantum quenches in the Hubbard model: Time-dependent mean-field theory and the role of quantum fluctuations".
In: *Phys. Rev. B - Condens. Matter Mater. Phys.* 83.16 (2011).

[25] Simone A. Hamerla and Götz S. Uhrig. "Dynamical transition in interaction quenches of the one-dimensional Hubbard model".
In: *Phys. Rev. B - Condens. Matter Mater. Phys.* 87.6 (2013).

[26] Simone A. Hamerla and Götz S. Uhrig. "One-dimensional fermionic systems after interaction quenches and their description by bosonic field theories". In: *New J. Phys.* 15 (2013).

[27] Konstantin V. Krutitsky et al. "Propagation of quantum correlations after a quench in the Mott-insulator regime of the Bose-Hubbard model". In: *EPJ Quantum Technol.* 1.1 (2014).

[28] Patrick Navez and Ralf Schützhold. "Emergence of coherence in the Mott-insulator-superfluid quench of the Bose-Hubbard model". In: *Phys. Rev. A - At. Mol. Opt. Phys.* 82.6 (2010).

[29] Andrew J. Daley et al. "Time-dependent density-matrix renormalization-group using adaptive effective Hilbert spaces". In: *J. Stat. Mech. Theory Exp.* 2004.04 (2004).

[30] George G. Batrouni et al. "Dynamic response of trapped ultracold bosons on optical lattices". In: *Phys. Rev. A - At. Mol. Opt. Phys.* 72.3 (2005).

[31] Florian Goth and Fakher F. Assaad. "Time and spatially resolved quench of the fermionic Hubbard model showing restricted equilibration". In: *Phys. Rev. B - Condens. Matter Mater. Phys.* 85.8 (2012).

[32] Michael Moeckel and Stefan Kehrein. "Real-time evolution for weak interaction quenches in quantum systems". In: *Ann. Phys. (N. Y).* 324.10 (2009).

[33] Javier Sabio and Stefan Kehrein. "Sudden interaction quench in the quantum sine-Gordon model". In: *New J. Phys.* 12 (2010).

[34] Jorn Mossel, Guillaume Palacios, and Jean-Sébastien Caux. "Geometric quenches in quantum integrable systems". In: *J. Stat. Mech. Theory Exp.* 2010.09 (2010).

[35] Vincenzo Alba and Fabian Heidrich-Meisner. "Entanglement spreading after a geometric quench in quantum spin chains". In: *Phys. Rev. B - Condens. Matter Mater. Phys.* 90.7 (2014).

[36] Thilo Stöferle et al. "Transition from a Strongly Interacting 1D Superfluid to a Mott Insulator". In: *Phys. Rev. Lett.* 92.13 (2004).

[37] Jacob F. Sherson et al. "Single-atom-resolved fluorescence imaging of an atomic Mott insulator". In: *Nature* 467.7311 (2010).

[38] Scott N. Sanders, Florian Mintert, and Eric J. Heller.
"Matter-Wave Scattering from Ultracold Atoms in an Optical Lattice".
In: *Phys. Rev. Lett.* 105.3 (2010).

[39] Klaus Mayer, Alberto Rodriguez, and Andreas Buchleitner.
"Matter-wave scattering from interacting bosons in an optical lattice".
In: *Phys. Rev. A - At. Mol. Opt. Phys.* 90.2 (2014).

[40] Igor B. Mekhov, Christoph Maschler, and Helmut Ritsch.
"Probing quantum phases of ultracold atoms in optical lattices by transmission spectra in cavity quantum electrodynamics".
In: *Nat. Phys.* 3.5 (2007).

[41] Renate Landig et al. "Measuring the dynamic structure factor of a quantum gas undergoing a structural phase transition".
In: *Nat. Commun.* 6.7046 (2015).

[42] Nicolai ten Brinke and Ralf Schützhold. "Dicke superradiance as a nondestructive probe for quantum quenches in optical lattices".
In: *Phys. Rev. A - At. Mol. Opt. Phys.* 92.1 (2015).

[43] Josh M. Deutsch. "Quantum statistical mechanics in a closed system".
In: *Phys. Rev. A* 43.4 (1991).

[44] Mark Srednicki. "Chaos and quantum thermalization".
In: *Phys. Rev. E* 50.2 (1994).

[45] Marcos Rigol.
"Breakdown of Thermalization in Finite One-Dimensional Systems".
In: *Phys. Rev. Lett.* 103.10 (2009).

[46] John Hubbard. "Electron correlations in narrow energy bands".
In: *Proc. R. Soc. A Math. Phys. Eng. Sci.* 276.1365 (1963).

[47] Junjiro Kanamori.
"Electron Correlation and Ferromagnetism of Transition Metals".
In: *Prog. Theor. Phys.* 30.3 (1963).

[48] Martin C. Gutzwiller.
"Effect of Correlation on the Ferromagnetism of Transition Metals".
In: *Phys. Rev. Lett.* 10.5 (1963).

[49] Gregory H. Wannier.
"The Structure of Electronic Excitation Levels in Insulating Crystals".
In: *Phys. Rev.* 52.3 (1937).

[50] Gerd Czycholl. *Theoretische Festkörperphysik*. Berlin: Springer, 2008.

[51] Elliott H. Lieb and Fa-Yueh Wu. "Absence of Mott transition in an exact solution of the short-range, one-band model in one dimension". In: *Phys. Rev. Lett.* 20.25 (1968).

[52] Fabian H. L. Essler et al. *The One-Dimensional Hubbard Model*. Cambridge: Cambridge University Press, 2005.

[53] Felix Bloch. "Über die Quantenmechanik der Elektronen in Kristallgittern". In: *Zeitschrift für Phys.* 52.7-8 (1929).

[54] Jens Eisert, Mathis Friesdorf, and Christian Gogolin. "Quantum many-body systems out of equilibrium". In: *Nat. Phys.* 11.2 (2015).

[55] Jürgen Berges, Szabolcs Borsányi, and Christof Wetterich. "Prethermalization". In: *Phys. Rev. Lett.* 93.14 (2004).

[56] Marcos Rigol et al. "Relaxation in a Completely Integrable Many-Body Quantum System: An Ab Initio Study of the Dynamics of the Highly Excited States of 1D Lattice Hard-Core Bosons". In: *Phys. Rev. Lett.* 98.5 (2007).

[57] Amy C. Cassidy, Charles W. Clark, and Marcos Rigol. "Generalized Thermalization in an Integrable Lattice System". In: *Phys. Rev. Lett.* 106.14 (2011).

[58] Toshiya Kinoshita, Trevor Wenger, and David S. Weiss. "A quantum Newton's cradle". In: *Nature* 440.7086 (2006).

[59] Chen N. Yang. "Some exact results for the many-body problem in one dimension with repulsive delta-function interaction". In: *Phys. Rev. Lett.* 19.23 (1967).

[60] Rodney J. Baxter. *Exactly Solved Models in Statistical Mechanics*. London: Academic Press, 1989.

[61] Piers Coleman. *Introduction to Many-Body Physics*. Cambridge: Cambridge University Press, 2015.

[62] Simone A. Hamerla. "Dynamics of Fermionic Hubbard Models after Interaction Quenches in One and Two Dimensions". PhD Thesis. Technische Universität Dortmund, 2013.

[63] Martin Eckstein, Marcus Kollar, and Philipp Werner. "Interaction quench in the Hubbard model: Relaxation of the spectral function and the optical conductivity". In: *Phys. Rev. B - Condens. Matter Mater. Phys.* 81.11 (2010).

[64] Simone A. Hamerla and Götz S. Uhrig. "Interaction quenches in the two-dimensional fermionic Hubbard model". In: *Phys. Rev. B - Condens. Matter Mater. Phys.* 89.10 (2014).

[65] Hideo Aoki et al.
"Nonequilibrium dynamical mean-field theory and its applications".
In: *Rev. Mod. Phys.* 86.2 (2014).

[66] Wolfgang Nolting. *Grundkurs Theoretische Physik 7*.
Berlin: Springer Spektrum, 2015.

[67] Claude Cohen-Tannoudji, Bernard Diu, and Franck Laloë.
Quantenmechanik I. Quantenmechanik. Berlin: de Gruyter, 2009.

[68] Götz S. Uhrig. "Interaction quenches of Fermi gases".
In: *Phys. Rev. A - At. Mol. Opt. Phys.* 80.6 (2009).

[69] Holger Krull. "Conductivity of strongly pumped superconductors: An electron-phonon system far from equilibrium".
PhD Thesis. Technische Universität Dortmund, 2014.

[70] Mona Kalthoff et al. "Comparison of the iterated equation of motion approach and the density matrix formalism for the quantum Rabi model".
In: *Eur. Phys. J. B* 90.5 (2017).

[71] Erwin Fehlberg. "Low-order classical Runge-Kutta formulas with stepsize control and their application to some heat transfer problems".
In: *NASA Tech. Rep.* (1969), Report 315.

[72] John R. Dormand and Peter J. Prince.
"A family of embedded Runge-Kutta formulae".
In: *J. Comput. Appl. Math.* 6.1 (1980).

[73] Przemyslaw Bogacki and Lawrence F. Shampine.
"A 3(2) Pair of Runge-Kutta Formulas". In: *Appl. Math. Lett.* 2.4 (1989).

[74] Sebastian Tomaskovic-Moore. "Vector Differential Equations: Defective Coefficient Matrix and Matrix Exponential Solutions".
University Lecture Notes. University of Pennsylvania, 2015.

[75] Elliott H. Lieb and Derek W. Robinson.
"The Finite Group Velocity of Quantum Spin Systems".
In: *Commununications Math. Phys.* 28 (1972).

[76] Franz Wegner. "Expectation Values, Wick's Theorem and Normal Ordering".
University Lecture Notes. University of Heidelberg, 2000.

[77] Gian-Carlo Wick. "The Evaluation of the Collision Matrix".
In: *Phys. Rev.* 80.2 (1950).

[78] Walter E. Arnoldi. "The principle of minimized iterations in the solution of the matrix eigenvalue problem". In: *Q. Appl. Math.* 9.1 (1951).

[79] Cornelius Lanczos. “An Iteration Method for the Solution of the Eigenvalue Problem of Linear Differential and Integral Operators”.
In: *J. Res. Natl. Bur. Stand. (1934).* 45.4 (1950).

[80] Claude E. Shannon. “Communication in the Presence of Noise”.
In: *Proc. IRE* 37.1 (1949).

[81] Peter Arbenz.
“Numerical Methods for Solving Large Scale Eigenvalue Problems”.
University Lecture Notes. Eidgenössische Technische Hochschule Zürich, 2016.

[82] *Parallelism in the Intel Math Kernel Library.*
URL: `https://software.intel.com/en-us/articles/parallelism-in-the-intel-math-kernel-library` (visited on 06/26/2017).

[83] Thomas H. Cormen et al. *Introduction to Algorithms.*
Cambridge: MIT Press, 2009.

[84] Marcos Rigol, Vanja Dunjko, and Maxim Olshanii.
“Thermalization and its mechanism for generic isolated quantum systems”.
In: *Nature* 452.7189 (2008).

[85] Miguel A. Cazalilla.
“Effect of Suddenly Turning on Interactions in the Luttinger Model”.
In: *Phys. Rev. Lett.* 97.15 (2006).

[86] Johannes Rentrop, Dirk Schuricht, and Volker Meden. “Quench dynamics of the Tomonaga-Luttinger model with momentum-dependent interaction”.
In: *New J. Phys.* 14 (2012).

[87] Peter Reineker, Michael Schulz, and Beatrix Schulz. *Theoretische Physik III.*
Weinheim: Wiley-VCH, 2007.

[88] Peter Reineker, Michael Schulz, and Beatrix Schulz. *Theoretische Physik IV.*
Weinheim: Wiley-VCH, 2008.

Danksagungen

Für die hervorragende Betreuung, große Geduld bei der Beantwortung jeder meiner Fragen im Rahmen dieser Arbeit und konzeptionelle Ideen zum Vorgehen bedanke ich mich bei Herrn Prof. Dr. Götz S. Uhrig. Ich danke Herrn Prof. Dr. Ralf Schützhold von der Universität Duisburg-Essen für die freundliche Übernahme des externen Zweitgutachtens dieser Arbeit.

Der gesamten Arbeitsgruppe T1a danke ich für fachnahe und -fremde Gespräche sowie die angenehme Atmosphäre.

Frau Fiona Krahé spreche ich meinen Dank für ein umfangreiches sprachliches Lektorat dieser Arbeit aus. Herrn Matthias Gianfelice danke ich für seine Meinung zu Text, Layout und Grafik und dafür, dass er es stillschweigend ertragen hat, wenn ich sein Büro zu meinem umfunktioniert habe.

Ich danke den besten Menschen, die ich kenne. Ich danke meinen Eltern, die mich mein ganzes Leben lang unterstützt, stets an mich geglaubt und mir Türen zu öffnen geholfen haben, die ich für fest verschlossen hielt.

Eidesstattliche Versicherung

Ich versichere hiermit an Eides statt, dass ich die vorliegende Masterarbeit mit dem Titel „Stationary states after interaction quenches in the Fermi-Hubbard model“ selbstständig und ohne unzulässige fremde Hilfe erbracht habe. Ich habe keine anderen als die angegebenen Quellen und Hilfsmittel benutzt, sowie wörtliche und sinngemäße Zitate kenntlich gemacht. Die Arbeit hat in gleicher oder ähnlicher Form noch keiner Prüfungsbehörde vorgelegen.

Ort, Datum | Unterschrift

Belehrung

Wer vorsätzlich gegen eine die Täuschung über Prüfungsleistungen betreffende Regelung einer Hochschulprüfungsordnung verstößt, handelt ordnungswidrig. Die Ordnungswidrigkeit kann mit einer Geldbuße von bis zu 50 000 € geahndet werden. Zuständige Verwaltungsbehörde für die Verfolgung und Ahndung von Ordnungswidrigkeiten ist der Kanzler/die Kanzlerin der Technischen Universität Dortmund. Im Falle eines mehrfachen oder sonstigen schwerwiegenden Täuschungsversuches kann der Prüfling zudem exmatrikuliert werden (§63 Abs. 5 Hochschulgesetz –HG–).

Die Abgabe einer falschen Versicherung an Eides statt wird mit Freiheitsstrafe bis zu drei Jahren oder mit Geldstrafe bestraft.

Die Technische Universität Dortmund wird ggf. elektronische Vergleichswerkzeuge (wie z. B. die Software „turnitin“) zur Überprüfung von Ordnungswidrigkeiten in Prüfungsverfahren nutzen.

Die oben stehende Belehrung habe ich zur Kenntnis genommen.

Ort, Datum | Unterschrift